Project Title: An Integrated Approach to Characterizing Bypassed Oil in Heterogeneous and Fractured Reservoirs Using Partitioning Tracers

ANNUAL REPORT
Reporting Period Start Date: June 2002
Reporting Period End Date: June 2003

Principal Author: Akhil Datta-Gupta
August, 2003

DOE Contract No. DE-FC26-02NT15345

Submitting Organization:
Texas Engineering Experiment Station
Texas A&M University, College Station, TX

Subcontractor: Gary A. Pope
Petroleum and Geosystems Engineering
University of Texas, Austin, TX

DISCLAIMER

ABSTRACT

We explore the use of efficient streamline-based simulation approaches for modeling partitioning interwell tracer tests in hydrocarbon reservoirs. Specifically, we utilize the unique features of streamline models to develop an efficient approach for interpretation and history matching of field tracer response. A critical aspect here is the underdetermined and highly ill-posed nature of the associated inverse problems. We have adopted an integrated approach whereby we combine data from multiple sources to minimize the uncertainty and non-uniqueness in the interpreted results. For partitioning interwell tracer tests, these are primarily the distribution of reservoir permeability and oil saturation distribution. A novel approach to multiscale data integration using Markov Random Fields (MRF) has been developed to integrate static data sources from the reservoir such as core, well log and 3-D seismic data. We have also explored the use of a finite difference reservoir simulator, UTCHEM, for field-scale design and optimization of partitioning interwell tracer tests. The finite-difference model allows us to include detailed physics associated with reactive tracer transport, particularly those related with transverse and cross-streamline mechanisms. We have investigated the potential use of downhole tracer samplers and also the use of natural tracers for the design of partitioning tracer tests. Finally, the behavior of partitioning tracer tests in fractured reservoirs is investigated using a dual-porosity finite-difference model.

TABLE OF CONTENTS

EXECUTIVE SUMMARY

During the first year of the project, we have explored the use of efficient streamline-based simulation approaches for modeling partitioning interwell tracer tests in hydrocarbon reservoirs. We utilized the unique features of streamline models to develop an efficient approach for interpretation and history matching of field tracer response. A critical aspect here is the underdetermined and highly ill-posed nature of the associated inverse problems. As a result, the interpretation of the tests can be highly ambiguous and non-unique. To circumvent the problem, we have adopted an integrated approach whereby we integrate data from multiple sources to minimize the uncertainty and non-uniqueness in the interpreted results. For partitioning interwell tracer tests, these are primarily the distribution of reservoir permeability and oil saturation distribution. We have also explored the use of a finite difference reservoir simulator, UTCHEM, for field-scale design and optimization of partitioning interwell tracer tests. The finite-difference model allows us to include detailed physics associated with reactive tracer transport, particularly those related with transverse and cross-streamline mechanisms. We have investigated the potential use of downhole tracer samplers and also the use of natural tracers for the design of partitioning tracer tests. Finally, the behavior of partitioning tracer tests in fractured reservoirs is investigated using a dual-porosity finite-difference model.

This report is divided into three major parts. The first part deals with the interpretation of interwell tracer test via inverse modeling. Specifically, we have investigated the relative merits of the traditional history matching ('amplitude inversion') and a novel travel time inversion in terms of robustness of the method and convergence behavior of the solution. We show that the traditional amplitude inversion is orders of magnitude more non-linear and the solution here is likely to get trapped in local minimum, leading to inadequate history match. The proposed travel time inversion is shown to be extremely efficient and robust for practical field applications.

The second part of the report describes a novel approach to multiscale data integration using Markov Random Fields (MRF). A key to proper interpretation of tracer tests is a good prior geological model. This prior model should be able to integrate various forms of static data such core, logs and 3-D seismic, accounting for the different scale and precision the data types. We examined the role of MRF for this purpose through the use of a field application that involves the integration of well log and seismic data during geologic modeling.

The third part of the report is devoted to the field scale design and optimization of tracer tests using a finite difference simulator, UTCHEM. This simulator has been widely used throughout the industry and its accuracy and ability to model complex physical processes have been demonstrated through numerous field applications. During the first year, we have investigated the potential use of downhole tracer samplers to measure tracer concentrations in real time at multiple depths and their role in improving the test design. Another important idea related to test design is the use of water-soluble components of crude oil as partitioning tracers. The UTCHEM simulator has been used to explore the validity of this concept. Finally, we have started to examine the utility of partitioning tracer tests in fractured reservoirs using a dual porosity version of UTCHEM.

The following papers were published based on the work from the first year of this research project.

1. Cheng, H., Datta-Gupta, A. and He, Zhong., "A Comparison of Travel Time and Amplitude Matching for Field-Scale Production Data Integration: Sensitivity, Non-Linearity and Practical Implications," SPE 84570 presented at the SPE Annual Technical Conference and Exhibition , Denver, CO, October 5-8, 2003.
2. Malallah, A., Perez, H., Datta-Gupta, A. and Alamody, W., "Multiscale Data Integration Using Markov Random Fields and Markov Chain Monte Carlo: A Field Application in the Middle East,"SPE 81544 presented at the SPE 13th Middle East Oil Show & Conference, Bahrain 2-6 June 2003

Also, we have developed a 3D streamline simulator for modeling tracer tests in petroleum reservoirs. A user-friendly interface with basic graphics capabilities have been added to facilitate use of the model by practicing engineers. The program is now available for public distribution and a copy is attached with this report.

INTRODUCTION

Streamline Modeling of Partitioning Interwell Tracer Tests

Streamline models approximate 3D fluid flow calculations by a sum of 1D solutions along streamlines. The choice of streamline directions for the 1D calculations makes the approach extremely effective for modeling convection-dominated flows in the presence of strong heterogeneity. Briefly, in this approach we first compute the pressure distribution using a finite difference solution to the conservation equations. The velocity field is then obtained using Darcy's law. A key step is streamline simulation is the decoupling of flow and transport by a coordinate transformation from the physical space to one following flow directions. This is accomplished by defining a streamline 'time of flight' as follows:

$$\tau(\psi) = \int_{\psi} \frac{1}{|\mathbf{v}(\mathbf{x})|} dr \tag{1}$$

Thus, the time of flight is simply the travel time of a neutral tracer along a streamline. In Eq.(1), r is the distance along the streamline and $\mathbf{x}$ refers to the spatial coordinates. We will exploit an analogy between streamlines and seismic ray tracing to utilize efficient techniques from geophysical inverse theory for analysis of field tracer tests. To facilitate this analogy, we will rewrite the time of flight in terms of a 'slowness' commonly used in ray theory in seismology. The 'slowness' is defined as the reciprocal of velocity as follows

$$s(\mathbf{x}) = \frac{1}{|\mathbf{v}(\mathbf{x})|} = \frac{\mu\,\phi(\mathbf{x})}{k(\mathbf{x})|\nabla P(\mathbf{x})|} \tag{2}$$

where we have used Darcy's law for the interstitial velocity v and ϕ is the porosity, k is permeability, and P is the pressure. The streamline time of flight can now be written as

$$\tau(\psi) = \int_{\psi} s(\mathbf{x}) dr \tag{3}$$

Consider the convective transport of a neutral tracer. The conservation equation is given by

$$\frac{\partial C(\mathbf{x},t)}{\partial t} + \mathbf{v}\cdot\nabla C(\mathbf{x},t) = 0 \tag{4}$$

where C represents the tracer concentration. We can rewrite (4) in the streamline time of flight coordinates using the operator identity

$$\mathbf{v}\cdot\nabla = \frac{\partial}{\partial\tau}. \tag{5}$$

Physically, we have now moved to a coordinate system where all streamlines are straightlines and the distance is measured in units of τ. The coordinate transformation reduces the multidimensional transport equation into a series of one-dimensional equations along streamlines,

$$\frac{\partial C(\tau,t)}{\partial t} + \frac{\partial C(\tau,t)}{\partial \tau} = 0\,. \tag{6}$$

The tracer response at a producing well can be obtained by simply integrating the contributions of individual streamlines reaching the producer,

$$C(t) = \int C_0\left(t - \tau(\psi)\right) d\psi = \int C_0\left(t - \int_{\psi} s(\mathbf{x}) dr\right) d\psi \tag{7}$$

where C_0 is the tracer concentration at the injection well. If we include longitudinal dispersion along streamlines, then the tracer concentration at the producing well will be given by

$$C(t) = \int \frac{\exp[-(t-\tau(\psi))^2/(4\alpha\omega)]}{\sqrt{4\alpha\omega}} d\psi \tag{8}$$

where α is longitudinal dispersivity and $\omega = \int_{\psi} \frac{dr}{\left|\mathbf{v}(\mathbf{x})\right|^2}$.

During partitioning interwell tracer tests the retardation of partitioning tracers in the presence of oil saturation can simply be expressed as an increase in travel time along streamlines. This in turn results in an increased slowness as follows

$$s(\mathbf{x}) = \frac{1}{\left|\mathbf{v}(\mathbf{x})\right|}(S_w + K_N S_N) = \frac{\mu\,\phi(\mathbf{x})}{k(\mathbf{x})\left|\nabla P(\mathbf{x})\right|}(S_w + K_N S_N) \tag{9}$$

where S_w and S_N denote water and oil saturation and K_N is the partitioning coefficient of tracer defined as the ratio of tracer concentration in the oil phase to that in the water phase. Notice that when the tracer has equal affinity towards water and oil ($K_N = 1$), the tracer response will be insensitive to oil saturation as one would expect and Eq.(8) reverts back to Eq.(2) for single phase tracer transport. If the oil is mobile, the impact of oil saturation on the hydraulic conductivity can be accounted for through the use of appropriate relative permeability functions.

Fast and Robust History Matching of Field Tracer Tests: A Comparison of Travel Time vs. Amplitude Inversion

Traditional approach to reconciling geologic models to field tracer data involves an "amplitude matching", that is matching the tracer history directly. It is well-known that such amplitude matching results in a highly non-linear inverse problem and difficulties in convergence, often leading to an inadequate history match. The non-linearity can also aggravate the problem of non-uniqueness and instability of the solution. Recently, dynamic data integration via 'travel-time matching' has shown great promise for practical field applications. In this approach the observed data and model predictions are lined up at some reference time such as the breakthrough or 'first arrival' time. Further extensions have included amplitude information via a 'generalized travel-time' inversion. Although the travel-time inversion has been shown to be more robust compared to amplitude matching, no systematic study has been done to examine the relative merits of the methods in terms of the non-linearities and convergence properties, particularly for field-scale applications. In this work we quantitatively investigate the non-linearities in the inverse problems related to travel-time, generalized travel-time and amplitude matching during production data integration. Our results show that the commonly used amplitude inversion can be orders of magnitude more non-linear compared to the travel-time inversion. The travel-time matching is extremely robust and the minimization proceeds rapidly even if the prior geologic model is not close to the solution. The travel-time sensitivities are more uniform between the wells compared to the amplitude sensitivities that tend to be localized near the wells. This prevents over-correction near the wells. Also, for field data characterized by multiple peaks, the travel-time inversion can prevent the solution from converging to secondary peaks, resulting in a better fit to the production response. We have demonstrated our results using a field application involving a multiwell, multitracer interwell tracer injection study in the McCleskey sandstone of

the Ranger field, Texas. Starting with a prior geologic model, the traditional amplitude matching could not reproduce the field tracer response which was characterized by multiple peaks. Both travel time and generalized travel time exhibited better convergence properties and could match the tracer response at the wells with realistic changes to the geologic model. Our results appear to confirm the power and robustness of the travel-time matching for field scale production data integration.

Multiscale Data Integration for Reservoir Characterization

Proper characterization of reservoir heterogeneity using available static data sources such as geologic data, well log, core and seismic data is a prerequisite to analysis and interpretation of field tracer tests. Integrating multi-resolution data sources into high-resolution reservoir models for accurate performance forecasting is an outstanding challenge in reservoir characterization. Well logs, cores, seismic and production data scan different length scales of heterogeneity and have different degrees of precision. Current geostatistical techniques for data integration rely on a stationarity assumption that is often not borne out by field data. Geologic processes can vary abruptly and systematically over the domain of interest. In addition, geostatistical methods require modeling and specification of variograms that can often be difficult to obtain in field situations. We present a case study from the Middle East to demonstrate the feasibility of a hierarchical approach to spatial modeling based on Markov Random Fields (MRF) and multi-resolution algorithms in image analysis. Our proposed approach provides an efficient and powerful framework for data integration accounting for the scale and precision of different data types. Unlike their geostatistical counterparts that simultaneously specify distributions across the entire field, the MRF are based on a collection of full conditional distributions that rely on local neighborhood of each element. This critical focus on local specification provides several advantages: (a) MRFs are far more computationally tractable and are ideally suited to simulation-based computation such as MCMC (Markov Chain Monte Carlo) methods, and (b) model extensions to account for non-stationarities, discontinuity and varying spatial properties at various scales of resolution are accessible in the MRF. We construct fine scale porosity distribution from well and seismic data explicitly accounting for the varying scale and precision of the data types. First, we derive a relationship between the neutron porosity and the seismic amplitudes. Second, we integrate the seismically derived coarse-scale porosity with fine-scale well data to generate a 3-D field-wide porosity distribution using MRF. The field application demonstrates the feasibility of this emerging technology for practical reservoir characterization.

Field-Scale Design Optimization via Numerical Simulation

To complement the streamline-based studies carried out at Texas A&M, a parallel effort has been ongoing using a finite difference model, UTCHEM for field-scale design and optimization of tracer tests. This work is carried out under the supervision of Dr. Gary A. Pope at the University of Texas, a subcontractor to the project.

The past several years have seen a great increase in the development, deployment and application of permanent in-well fiber optic monitoring systems. In-well fiber optic sensors are either currently available or under active development for measuring pressure, temperature, flow rate, phase fraction, strain, acoustics, and sand production. Potential future sensor developments

include measurement of density and fluid chemistry. This study is a preliminary investigation of the use of downhole sensors to enhance the value of Partitioning Interwell Tracer Tests (PITTs). The idea being investigated is to measure the tracer concentrations in real time at multiple depths using downhole sensors. These tracer concentration data could be used to estimate oil saturations at the corresponding depths using the method of moments and/or inverse modeling.

Crude oil is a mixture of organic components of varying water solubility. A novel idea being investigated in this research is to use some of the more water-soluble components of crude oil as natural partitioning tracers to estimate oil saturations and swept pore volumes, and hence as a substitute for injected tracers. The rate at which these components will dissolve into water will depend upon their partition coefficients under reservoir conditions. In this study we have identified some of the common components of crude oils that might be used as natural partitioning tracers. Equations have been derived to estimate pore volumes and average oil saturations in a reservoir for both single-phase and multiphase flow and two simulations used to illustrate their validity under the assumed conditions.

Naturally fractured reservoirs can be modeled as two interconnected media: the matrix which contains the bulk of the fluid, but has very less conductive capacity, and the fracture which generally has high permeability but very little storage capacity. The dual porosity model is one of the oldest and most common approaches for modeling naturally fractured oil reservoirs and is available in most reservoir simulators including UTCHEM and ECLIPSE. The simulation domain is divided into two superimposed porous media: one for the fracture system and another for the porous rock matrix. A mass balance for each of the media results in two continuity equations coupled by a transfer function. This study compares the ECLIPSE and UTCHEM results for a series of partitioning tracer simulations as a first step in our research on how to optimize the use of tracers in naturally fractured oil reservoirs.

EXPERIMENTAL

No experiments were performed during the first year of the project.

RESULTS AND DISCUSSION: PART I

Fast and Robust History Matching of Field Tracer Tests: A Comparison of Travel Time vs. Amplitude Inversion

Introduction

Geological models derived from static data alone often fail to reproduce the production history of a reservoir. Reconciling geologic models to the dynamic response of the reservoir is critical to building reliable reservoir models. In recent years several techniques have been developed for integrating production data into reservoir models.[1-14] The theoretical basis of these techniques is generally rooted in the least-squares inversion theory that attempts to minimize the difference between the observed production data and the model predictions. This can be referred to as 'amplitude' matching. The production data can be water-cut observations, tracer response or pressure history at the wells. It is well known that such inverse problems are typically ill-posed and can result in non-unique and unstable solutions. Proper incorporation of static data in the form of a prior model can partially alleviate the problem. However, there are additional outstanding challenges that have deterred the routine integration of production data into reservoir models. The relationship between the production response and reservoir properties can be highly non-linear. The non-linearity can result in multiple local minima in the misfit function. This can cause the solution to converge to a local minimum, leading to an inadequate history match. All these can make it difficult to obtain a meaningful estimate of the parameter field, particularly if the initial model is far from the solution.

Recently streamline-based methods have shown significant potential for incorporating dynamic data into high resolution reservoir models.[1-14] A unique feature of the streamline-based production data integration has been the concept of a 'travel-time match' that is analogous to seismic tomography. Instead of matching the production data directly, the observed data and model predictions are first 'line-up' at the breakthrough time. This is typically followed by a conventional 'amplitude match' whereby the difference between the observed and calculated production response is minimized. A major part of the production data misfit reduction occurs during the travel-time inversion and most of the large-scale features of heterogeneity are resolved at this stage.[2,4-5]

The concept of travel-time inversion is not limited to streamline models. Recently, it has been extended for application to finite-difference models via a 'generalized travel-time' inversion.[9] The 'generalized travel-time' inversion ensures matching of the entire production response rather than just the breakthrough times and at the same time retains most of the desirable properties of the travel-time inversion. The concept follows from wave-equation travel-time tomography and is very general, robust and computationally efficient.[12,15] The generalized travel-time inversion has been utilized to extend the streamline-based production data integration methods to changing field conditions involving rate changes and infill drilling.

The advantages of the travel-time inversion compared to amplitude inversion mainly stems from its quasilinear properties. Unlike conventional 'amplitude' matching which can be highly non-linear, it has been shown that the travel-time misfit function is quasilinear with respect to changes in reservoir properties.[2,4-5] As a result, the minimization proceeds rapidly even if the initial model is not close to the solution. These advantages of travel-time inversion are

well-documented in the context of seismic inversion.[15] However, no systematic study has been done to examine the benefits of travel-time inversion for production data integration in terms of non-linearity and convergence properties. Characterizing the degree of nonlinearity can be as important as finding the solutions to the inverse problem itself. However, quantitative measures of nonlinearity for the inverse problems related to production data integration haven't been adequately addressed.

We discuss the mathematical foundation for the measure of nonlinearity and its implications on the production data integration. We quantitative investigate the extent of nonlinearity in travel-time inversion and amplitude inversion. In particular, we show that the nonlinearity in travel-time inversion is orders of magnitude smaller than that of the amplitude inversion. This leads to better convergence properties and a robust method for production data integration. We illustrate our results using both synthetic and field applications. The field application is from the McCleskey sandstone, the Ranger field, Texas and involves a multiwell, multitracer interwell tracer injection study. The results clearly demonstrate the benefits of travel-time inversion for field-scale production data integration. In particular, the generalized travel-time inversion appears to outperform both travel-time and amplitude inversion in reconciling the geologic model to the field tracer response.

Background and Approach

Travel-Time Inversion, Amplitude Inversion and Generalized Travel-Time Inversion. Travel-time inversion attempts to match the observed data and model predictions at some reference time, for example the breakthrough time or the peak arrival time. Thus, we are lining-up the production response along the time axis. Fig.1a illustrates the travel-time inversion. On the other hand, the amplitude inversion attempts to match the production response directly. This is illustrated in Fig.1b whereby we match the observed tracer concentration and model predictions at the producing well. Creatively, we can combine the travel-time inversion and amplitude inversion into one step while retaining most of the desirable features of a travel-time inversion. This is the 'generalized travel-time inversion' and follows from the work of Luo and Schuster[15] in the context of wave equation travel-time tomography.

A generalized travel-time or travel-time shift is computed by systematically shifting the computed production response towards the observed data until the cross-correlation between the two is maximized. The approach is illustrated in Figs. 1c and 1d. It preserves the robustness of a travel-time inversion and improves computational efficiency by representing the production data misfit at a well in terms of a single travel-time shift. It can be shown to reduce to the more traditional least-squared misfit functional as we approach the solution.[12]

The advantages of travel-time inversion are well documented in the geophysics literature. For example, Luo and Schuster[15] pointed out that travel-time inversion is quasi-linear as opposed to amplitude inversion which can be highly non-linear. Amplitude inversion typically works well when the prior model is close to the solution. This was the rationale behind our previously proposed two-step approach to production data integration: travel-time match followed by amplitude match.[2,4] In this paper, we will quantitatively investigate the relative merits of the different methods in terms of non-linearity and convergence properties.

Measures of Nonlinearity. Characterizing and assessing the nonlinearity in the parameter estimation problem is critical to designing efficient and robust approaches to production data

integration. There are several methods for quantifying the degree of non-linearity in inverse problems. We will use the measure proposed by Bates and Watts[16] to examine the non-linearities in travel-time and amplitude inversion. Grimsted and Mannseth[17-18] applied this measure to examine the relationship between non-linearity, scale and sensitivity in parameter estimation problems. If F represents an outcome, for example, the tracer response, then the nonlinearity measure is defined as $\kappa=||Fkk||/||Fk||2$, where F_k is the vector of the first-order derivatives with respect to the parameter vector k, that is, the sensitivity vector, and F_{kk} is the vector of second-order derivatives. This measure is based on the geometric concept of curvature and κ represents the inverse of a radius of the circle that best approximates the outcome locus F in the direction of F_k at k. Smoother and more linear outcome will have smaller curvature (larger radius) and thus smaller measure of non-linearity as illustrated in Fig. 2.

In our application, we evaluate $\kappa=||Fkk||/||Fk||2$ for every iteration during inversion. In addition, for amplitude inversion, we compute the measure for different observations and choose the maximum. The details of the computations, including the derivative calculations for travel-time, amplitude, and generalized travel-time will be discussed later. In the following section, we first illustrate the approach using a synthetic example.

Non-linearity Measure in Production Data Integration: A Simple Illustration. This example involves integration of tracer response in a heterogeneous 9-spot pattern as shown in Fig. 3. The mesh size is 21×21. The reference permeability distribution consists of a low-permeability trend towards north and a high-permeability trend towards south. The tracer responses from the eight producers in the 9-spot pattern are shown in Fig. 4a. Also superimposed in Fig. 4a are the tracer responses corresponding to our initial model, a homogeneous permeability field that is conditioned at the well locations.

We compare the relative performance of travel-time, amplitude, and generalized travel-time inversion and also the non-linearities inherent in these approaches. Fig. 4b shows the tracer concentration matches after travel-time inversion. All the peak times are now in agreement although there are some discrepancies in the details of the tracer responses. Fig. 4c shows the tracer concentration matches after generalized travel-time inversion. Not only the peak arrival-times but also the amplitudes are matched much better compared to the travel-time inversion. Fig. 4d shows the tracer-responses match after the amplitude inversion. Although the matches are quite good for most wells, they are unsatisfactory for wells 2 and 7. Incidentally, these are the two wells that exhibited maximum discrepancy based on the initial model.

Fig. 5 shows the convergence behavior for the three methods. Both travel-time and generalized travel-time inversion reproduce the arrival times perfectly. The generalized travel-time further reduces the tracer concentration misfit. In contrast, direct amplitude match shows high arrival time misfit and is unable to reproduce the tracer response at two wells. Fig. 6a is the estimated permeability field after travel-time match. On comparing with Fig. 3, we can identify the low-permeability areas and some of the moderate-to-high permeability areas, although the high permeability area is not well reproduced. Fig. 6b shows the permeability field derived by generalized travel-time inversion. It reproduces not only the low-permeability area but also the high-permeability regions. Fig. 6c shows the estimated permeability field after the amplitude inversion. Clearly, the results show signs of instability because of the high non-linearity as discussed below.

Fig. 7 shows the measure of nonlinearity for the three approaches. We can see that both the travel-time and the generalized travel-time exhibit the same degrees of non-linearity. In

contrast, the amplitude inversion is three to four orders of magnitudes more nonlinear than the travel-time inversion. This is partly the reason for the failure of the amplitude inversion when the initial model is far from the solution. The generalized travel-time inversion appears to retain most of the desirable features of a travel-time inversion while obtaining an adequate amplitude match.

Mathematical Formulation: Sensitivity Computations and Measures of Nonlinearity

We now discuss the mathematical details related to sensitivity computation and measure of non-linearity for travel-time, generalized travel-time and amplitude inversion. Although the approach is generally applicable, we will use a streamline simulator here because of the advantages in sensitivity computations. The sensitivities quantify change in production response because of a small change in reservoir properties. They are an integral part of most inverse modeling methods. We also need the sensitivities to quantify non-linearities in the various inverse methods examined in this study. Several approaches can be used to compute sensitivity coefficients of model parameters. Most of these methods fall into one of the three categories: perturbation method, direct method, and adjoint state method[19-21] and can be computationally demanding, particularly for large-scale field applications. However, for streamline models, it is possible to analytically derive a relationship between perturbations in reservoir properties, such as permeability or porosity, and changes in observations such as watercut and tracer response. Streamline-based sensitivity computation is very fast and involves quantities computed by a single streamline simulation. Hence, we will limit our discussion to streamline models only.

We use the theory of Bates and Watts[16] to measure the nonlinearity in production data integration. Bates and Watts[16] separate the nonlinearity measures into parameter-effect curvature and intrinsic curvature; thus they decompose the second-order derivative F_{kk} into one component parallel to the tangent plane defined by F_k for all directions and another component normal to that plane. Here we do not separate the intrinsic curvature and parameter effect curvature; neither do we consider the direction in the parameter space since it is not practical to do so for our problem. However, the theory we applied is essentially the same as that of Bates and Watts.[16]

Sensitivity and Nonlinearity of Travel-time. Streamline methods decouple flow and transport by a coordinate transformation from the physical space to the time-of-flight along streamlines.[22] The time-of-flight is defined as

$$\tau = \int_{\psi} s(x)dr \quad , \tag{1}$$

where the integral is along the streamline trajectory, Ψ, and s is the slowness defined as the reciprocal of the interstitial velocity,

$$s = \frac{1}{|v|} = \frac{\phi}{k\lambda_{rt}|\nabla P|} \quad . \tag{2}$$

The first-order derivative of slowness with respect to permeability is

$$\frac{\partial s}{\partial k} = -\frac{s}{k} \quad . \tag{3}$$

and the second-order derivative of slowness is

$$\frac{\partial^2 s}{\partial k^2} = \frac{s}{k^2} \quad . \tag{4}$$

If we assume that the streamlines do not shift because of small perturbations in reservoir properties, we can then relate the change in travel time δτ to the change in slowness by

$$\delta\tau = \int_{\Psi} \delta s(x) dr$$
$$= \int_{\Psi} \left[-\frac{s(x)}{k(x)} \delta k(x) + \frac{s(x)}{\phi(x)} \delta\phi(x) \right] dr \quad . \tag{5}$$

The travel-time sensitivity along a single streamline at a producer with respect to permeability for a grid block at location x is given by integrating Eq. 3 from the inlet to the outlet of the streamline Ψ within the grid block:

$$\frac{\partial \tau(\psi)}{\partial k(x)} = \int_{inlet}^{outlet} \left[-\frac{s(x)}{k(x)} \right] dr(\psi) \quad . \tag{6}$$

The overall travel-time sensitivity is then obtained by summing the sensitivities over all streamlines contributing to the arrival time of a particular concentration (for example, the peak concentration):

$$\frac{\partial \tau}{\partial k(x)} = \sum_{all\ \psi} \frac{\partial \tau(\psi)}{\partial k(x)} \quad . \tag{7}$$

The second-order derivative of travel-time along a single streamline is obtained by integrating Eq. 4,

$$\frac{\partial^2 \tau(\psi)}{\partial k^2(x)} = \int_{inlet}^{outlet} \frac{s(x)}{k^2(x)} dr(\psi) \quad , \tag{8}$$

and then integrating over all streamlines contributing to a producer,

$$\frac{\partial^2 \tau}{\partial k^2(x)} = \sum_{\Psi} \frac{\partial^2 \tau(\psi)}{\partial k^2(x)} \quad . \tag{9}$$

The components of the tangent vector Fk and acceleration vector Fkk can now be obtained from Eqs. 7 and 9:

$$\text{Fk} = \left(\frac{\partial \tau}{\partial k_1}, \frac{\partial \tau}{\partial k_2}, \cdots, \frac{\partial \tau}{\partial k_{n_b}} \right)^T \quad ; \tag{10}$$

$$\text{Fkk} = \left(\frac{\partial^2 \tau}{\partial k_1^2}, \frac{\partial^2 \tau}{\partial k_2^2}, \cdots, \frac{\partial^2 \tau}{\partial k_{n_b}^2} \right)^T \quad . \tag{11}$$

The 2-norms are used to calculate the vector norms,

$$||\text{Fk}|| = \left(\sum_{j=1}^{n_b} \left(\frac{\partial \tau}{\partial k_j} \right)^2 \right)^{1/2} \quad , \tag{12}$$

$$||\text{Fkk}|| = \left(\sum_{j=1}^{n_b} \left(\frac{\partial^2 \tau}{\partial k_j^2} \right)^2 \right)^{1/2} \quad . \tag{13}$$

Now we can calculate the nonlinearity measure of travel-time inversion κtt according to the theory of Bates and Watts16 by

$$\kappa tt = ||\text{Fkk}|| / ||\text{Fk}||2 \tag{14}$$

Sensitivity and Nonlinearity of Amplitude. Tracer transport can be described by the following convection-diffusion equation,

$$\phi\frac{\partial C(x,t)}{\partial t}=\nabla\cdot[D(x)\cdot\nabla C(x,t)]-u\cdot\nabla C(x,t) \quad (15)$$

Ignoring the dispersion term, Eq. 15 can be rewritten as

$$\phi\frac{\partial C(x,t)}{\partial t}+u\cdot\nabla C(x,t)=0 \quad (16)$$

Applying a transformation to the time-of-flight coordinate, the tracer transport equation along a streamline can be expressed as22

$$\frac{\partial C(\tau,t)}{\partial t}+\frac{\partial C(\tau,t)}{\partial \tau}=0 \quad (17)$$

For a unit-impulse concentration at (τ, t)=(0,0), the solution is22

$$C(x,t)=\delta(t-\tau(x)), \quad (18)$$

where δ is the Dirac-delta function. If the input is C0, then

$$C(x,t)=C_0(t-\tau) \quad (19)$$

Summing the contributions of all streamlines reaching a producer, we get the tracer response at a producer as

$$C(t)=\int_{all\ \psi} C_0(t-\tau)d\psi \quad (20)$$

From Eq. 19, tracer response at the producer along a single streamline is

$$C(t)=C_0\left(t-\int_{\Psi} s(x)dr)\right) \quad (21)$$

where we have used the definition of time of flight from Eq.1.

Now, consider a small perturbation in reservoir properties, say permeability. The resulting changes in slowness and concentrations can be written as

$$s(x)=s^0(x)+\delta s(x), \quad (22)$$

$$C(t)=C^0(t)+\delta C(t), \quad (23)$$

where s0 and C0 are initial slowness distribution in the reservoir and the associated tracer response respectively. Applying Eqs. 21 and 22, the change in concentration response can be expressed as

$$\begin{aligned}\delta C(t)&=C(t)-C^0(t)\\&=C_0\left(t-\int_{\Psi}\left[s^0(x)+\delta s(x)\right]dr\right)-C_0\left(t-\int_{\Psi_0} s^0(x)dr)\right)\end{aligned} \quad (24)$$

Using a Taylor series expansion and assuming $\Psi=\Psi_0$ (stationary streamlines), we get

$$\begin{aligned}&C_0\left(t-\int_{\Psi}\left[s^0(x)+\delta s(x)\right]dr\right)\\&=C_0\left(t-\int_{\Psi_0} s^0(x)dr-\int_{\Psi_0}\delta s(x)dr\right)\end{aligned}$$

$$\approx C_0\left(t-\int_{\Psi_0} s^0(x)dr\right)+\left[\left(t-\int_{\Psi_0} s^0(x)dr-\int_{\Psi_0}\delta s(x)dr\right)\right.$$
$$\left.-\left(t-\int_{\Psi_0} s^0(x)dr\right)\right]C_0'\left(t-\int_{\Psi_0} s^0(x)dr\right)$$
$$=C_0\left(t-\int_{\Psi_0} s^0(x)dr\right)-\int_{\Psi_0}\delta s(x)dr\cdot C_0'\left(t-\int_{\Psi_0} s^0(x)dr\right). \quad (25)$$

Hence the perturbation in C(t) and s(x) are related by

$$\delta C(t)=-C_0'\left(t-\int_{\Psi_0} s^0(x)dr\right)\int_{\Psi_0}\delta s(x)dr. \quad (26)$$

The tracer-concentration sensitivity along a single streamline Ψ is then

$$\frac{\partial C(t)}{\partial k(x)}=-C_0'\left(t-\int_{\Psi} s^0(x)dr\right)\int_{\Psi}\frac{\partial s(x)}{\partial k(x)}dr$$
$$=-C_0'\left(t-\int_{\Psi} s^0(x)dr\right)\int_{\Psi}[-\frac{s(x)}{k(x)}]dr$$
$$=-C_0'\left(t-\int_{\Psi} s^0(x)dr\right)\frac{\partial\tau(\Psi)}{\partial k(x)}. \quad (27)$$

The second-order derivative of the tracer concentration with respect to permeability is

$$\frac{\partial^2 C(t)}{\partial k^2(x)}=-C_0'\left(t-\int_{\Psi} s^0(x)dr\right)\int_{\Psi}\frac{\partial^2 s(x)}{\partial k^2(x)}dr$$
$$=-C_0'\left(t-\int_{\Psi} s^0(x)dr\right)\int_{\Psi}\frac{s(x)}{k^2(x)}dr$$
$$=-C_0'\left(t-\int_{\Psi} s^0(x)dr\right)\frac{\partial^2\tau(\Psi)}{\partial k^2(x)}. \quad (28)$$

As before, we need to sum over all streamlines reaching a producer to get the final first-order and second-order derivatives of the concentration response at the producer.

Now we need to evaluate the tangent vector Fk, the acceleration vector Fkk, and measure of nonlinearity κ at different observation times. The vectors and norms are expressed as follows

$$\text{Fk(ti)}=\left(\frac{\partial C(t_i)}{\partial k_1},\frac{\partial C(t_i)}{\partial k_2},\cdots,\frac{\partial C(t_i)}{\partial k_{n_b}}\right)^T, \quad (29)$$

$$\text{Fkk(ti)}=\left(\frac{\partial^2 C(t_i)}{\partial k_1^2},\frac{\partial^2 C(t_i)}{\partial k_2^2},\cdots,\frac{\partial^2 C(t_i)}{\partial k_{n_b}^2}\right)^T; \quad (30)$$

$$\|\text{Fk(ti)}\|=\left(\sum_{j=1}^{n_b}(\frac{\partial C(t_i)}{\partial k_j})^2\right)^{1/2}, \quad (31)$$

$$\|\text{Fkk(ti)}\|=\left(\sum_{j=1}^{n_b}(\frac{\partial^2 C(t_i)}{\partial k_j^2})^2\right)^{1/2}. \quad (32)$$

By definition, the measure of nonlinearity at observation time ti is

$$\kappa(ti)=\|\text{Fkk(ti)}\|/\|\text{Fk(ti)}\|2. \quad (33)$$

The final measure of nonlinearity for amplitude inversion κam is given by the maximum over all observed data,

$$\kappa_{am} = \max\left(\kappa(t_1), \kappa(t_2), \cdots, \kappa(t_{n_o})\right). \tag{34}$$

Sensitivity and Nonlinearity of Generalized Travel Time. In generalized travel-time inversion we define the misfit between the calculated and observed tracer concentrations in terms of the following correlation function:[12,15]

$$f(x,\tau) = \int dt \frac{C(x,t+\tau)_o}{A_o} C(x,t)_c, \tag{35}$$

where A is the maximum amplitude of tracer concentration and τ is the shift time between calculated and observed tracer concentrations. We seek a τ that shifts the calculated tracer response so that it best matches the observed tracer response.

The criterion for the "best" match is defined as the travel-time residual Δτ that maximizes the correlation function above, that is,

$$f(x,\Delta\tau) = \max\{f(x,\tau) \mid \tau \in [-T,T]\}, \tag{36}$$

where T is the estimated maximum travel-time difference between the observed and calculated tracer responses. So the derivative of $f(x,\tau)$ with respect to τ should be zero at Δτ unless the maximum is at an end point T or –T,

$$\begin{aligned} \dot{f}_{\Delta\tau} &= \left[\frac{\partial f(x,\tau)}{\partial\tau}\right]_{\tau=\Delta\tau} \\ &= \frac{1}{A}\int dt \frac{\partial C(t+\Delta\tau)_o}{\partial t} C(t)_c \frac{\partial t}{\partial\tau} \\ &= \frac{1}{A}\int dt \frac{\partial C(t+\Delta\tau)_o}{\partial t} C(t)_c = 0 \end{aligned}. \tag{37}$$

Note that $\partial t/\partial\tau = 1$ in this derivation. Eq. 37 is the function that is used to compute the sensitivity of the generalized travel time.

Using Eq. 37 and the rule for the derivative of an implicit function, we get

$$\frac{\partial\Delta\tau}{\partial k(x)} = -\frac{\frac{\partial(\dot{f}_{\Delta\tau})}{\partial k(x)}}{\frac{\partial(\dot{f}_{\Delta\tau})}{\partial\Delta\tau}}. \tag{38}$$

Taking the derivatives of $\dot{f}_{\Delta\tau}$ with respect to k(x) and Δτ, we have

$$\begin{aligned} \frac{\partial(\dot{f}_{\Delta\tau})}{\partial k(x)} &= \frac{1}{A}\int dt \frac{\partial C(t+\Delta\tau)_o}{\partial t}\frac{\partial C(t)_c}{\partial k(x)} \\ &= \frac{1}{A}\int dt \frac{\partial C(t+\Delta\tau)_o}{\partial t}\frac{\partial C(t)_c}{\partial t}\frac{\partial t}{\partial\tau}\frac{\partial\tau}{\partial k(x)} \\ &= \frac{1}{A}\int dt \frac{\partial C(t+\Delta\tau)_o}{\partial t}\frac{\partial C(t)_c}{\partial t}\frac{\partial\tau}{\partial k(x)} \end{aligned}. \tag{39}$$

and

$$\frac{\partial\dot{f}_{\Delta\tau}}{\partial\Delta\tau} = \frac{\int dt \cdot E}{A}, \tag{40}$$

where

$$E = \frac{\partial C(t+\Delta\tau)_o}{\partial t}\frac{\partial C(t)_c}{\partial \Delta\tau} + C(t)_c \frac{\partial[\frac{\partial C(t+\Delta\tau)_o}{\partial t}]}{\partial \Delta\tau}$$
$$= \frac{\partial C(t+\Delta\tau)_o}{\partial t}\frac{\partial C(t)_c}{\partial t}\frac{\partial t}{\partial \Delta\tau} + C(t)_c \frac{\partial^2 C(t+\Delta\tau)_o}{\partial t^2}\frac{\partial t}{\partial \Delta\tau}$$
$$= \frac{\partial C(t+\Delta\tau)_o}{\partial t}\frac{\partial C(t)_c}{\partial t} + C(t)_c \frac{\partial^2 C(t+\Delta\tau)_o}{\partial t^2} \quad . \tag{41}$$

In the derivation above, we have applied the relationship $\frac{\partial t}{\partial \Delta\tau} = \frac{\partial t}{\partial \tau} = 1$ at $\tau = \Delta\tau$.

Substitution of Eqs. 39 through 41 into Eq. 38 gives

$$\frac{\partial \Delta\tau}{\partial k(x)} = \frac{\int dt[\frac{\partial C(t+\Delta\tau)_o}{\partial t}\frac{\partial C(t)_c}{\partial t}\frac{\partial \tau}{\partial k(x)}]}{\int dt[\frac{\partial C(t+\Delta\tau)_o}{\partial t}\frac{\partial C(t)_c}{\partial t} + C(t)_c \frac{\partial^2 C(t+\Delta\tau)_o}{\partial t^2}]} \quad . \tag{42}$$

The second-order derivative of generalized travel-time with respect to permeability is then

$$\frac{\partial^2 \Delta\tau}{\partial k^2(x)} = \frac{\int dt[\frac{\partial C(t+\Delta\tau)_o}{\partial t}\frac{\partial C(t)_c}{\partial t}\frac{\partial^2 \tau}{\partial k^2(x)}]}{\int dt[\frac{\partial C(t+\Delta\tau)_o}{\partial t}\frac{\partial C(t)_c}{\partial t} + C(t)_c \frac{\partial^2 C(t+\Delta\tau)_o}{\partial t^2}]} , \tag{43}$$

where $\frac{\partial^2 \tau}{\partial k^2}$ is calculated by Eq. 8.

Finally, to calculate measures of nonlinearity, the components of the tangent vector Fk and acceleration vector Fkk are obtained from Eqs. 42 and 43 as follows

$$\text{Fk} = \left(\frac{\partial \Delta\tau}{\partial k_1}, \frac{\partial \Delta\tau}{\partial k_2}, \cdots, \frac{\partial \Delta\tau}{\partial k_{n_b}}\right)^T ; \tag{44}$$

$$\text{Fkk} = \left(\frac{\partial^2 \Delta\tau}{\partial k_1^2}, \frac{\partial^2 \Delta\tau}{\partial k_2^2}, \cdots, \frac{\partial^2 \Delta\tau}{\partial k_{n_b}^2}\right)^T . \tag{45}$$

The 2-norms of the vectors are calculated by

$$||\text{Fk}|| = \left(\sum_{j=1}^{n_b} (\frac{\partial \Delta\tau}{\partial k_j})^2\right)^{1/2} ; \tag{46}$$

$$||\text{Fkk}|| = \left(\sum_{j=1}^{n_b} (\frac{\partial^2 \Delta\tau}{\partial k_j^2})^2\right)^{1/2} . \tag{47}$$

The measure of nonlinearity for the generalized travel-time inversion is evaluated using Eqs. 46 and 47

$$\kappa gt = ||\text{Fkk}||/||\text{Fk}||2, \tag{48}$$

Sensitivity Computations: A ¼ Five-spot Example. We illustrate sensitivity computations for the three methods using the tracer response in a heterogeneous quarter 5-spot pattern (**Fig. 8**). **Fig. 9a** is the sensitivity distribution for the peak travel-time, and **Fig. 9b** is the sensitivity distribution for the generalized travel-time. **Figs. 10a**, **10b**, and **10c** show the sensitivity

distribution for the amplitude before, at, and after peak time respectively. From **Figs. 9** and **10**, we can see that the sensitivity distribution between the wells for travel-time inversion is more uniform than that for amplitude inversion. Also, the magnitude of the amplitude sensitivity is much smaller than that of the travel-time sensitivity. This smaller sensitivity contributes to the high nonlinearity of amplitude inversion because the nonlinearity is evaluated by $||\boldsymbol{F}_{kk}||/||\boldsymbol{F}_k||^2$, where $\boldsymbol{F}_k$ is the sensitivity vector. Such relationship between non-linearity and sensitivity for inverse modeling has also been observed by Grimstad and Mannseth.[17-18]

Data Inversion

Our goal is to reconcile high-resolution geologic models to field production history, for example tracer response. This typically involves the solution of an underdetermined inverse problem. The mathematical formulation behind such streamline-based inverse problems has been discussed elsewhere.[2,4-5] Briefly, in our approach we start with a prior static model that already incorporates geologic, well log, and seismic data. We then minimize a penalized misfit function consisting of the following three terms,

$$\|\delta d - S\delta R\| + \beta_1\|\delta R\| + \beta_2\|L\delta R\| \quad \text{.....} \quad (49)$$

In **Eq. 49**, $\delta\boldsymbol{d}$ is the vector of data residuals at the wells, S is the sensitivity matrix containing the sensitivities of the observed data with respect to the reservoir parameters. Also, δR corresponds to the change in the reservoir property and L is a second-spatial-difference operator. The first term ensures that the difference between the observed and calculated production response is minimized. The second term, called a norm constraint, penalizes deviations from the initial model. This helps preserve geologic realism because our initial or prior model already incorporates available geologic and static information related to the reservoir. Finally, the third term, a roughness penalty, simply recognizes the fact that production data are an integrated response and are thus, best suited to resolve large-scale structures rather than small-scale property variations.

The minimum in Eq. 49 can be obtained by an iterative least-squares solution to the augmented linear system

$$\begin{pmatrix} S \\ \beta_1 I \\ \beta_2 L \end{pmatrix} \delta R = \begin{pmatrix} \delta d \\ 0 \\ 0 \end{pmatrix}. \quad \text{.....} \quad (50)$$

The weights β_1 and β_2 determine the relative strengths of the prior model and the roughness term. The selection of these weights can be somewhat subjective although there are guidelines in the literature.[23] In general, the inversion results will be sensitive to the choice of these weights.

In **Eq. 50**, $\delta\boldsymbol{d}$ is replaced by $\delta\boldsymbol{\tau}$ for travel-time inversion, $\delta\boldsymbol{C}$ for amplitude inversion, and $\delta\Delta\boldsymbol{\tau}$ for generalized travel-time inversion. The sensitivity matrix S is also replaced by the corresponding expression.

Note that one of the major advantages of travel-time and the generalized travel-time approach is that the size of the sensitivity matrix S is dependent only on the number of wells regardless of the number of data points. This leads to considerable savings in computation time. We use an iterative sparse matrix solver, LSQR, for solving this augmented linear system efficiently.[24] The LSQR algorithm is well suited for highly ill-conditioned systems and has been widely used for large-scale tomographic problems in seismology.[25]

Field Application: The Ranger Field, Texas

Dataset Description. A multiwell, mulitracer, interwell tracer injection study was carried out in the McCleskey sandstone of the Ranger field, Texas. The first description of this data set was published by Lichtenberger.[26] The dataset was also described later by Allison *et al*.[27] The 320-acre area of interest includes 13 producers and 4 injectors, injecting 7 different tracers. The seven tracers injected included 5 conservative tracers consisting of four decaying (Tritium, Cobalt-57, Cobalt-58, and Cobalt-60), one chemical (sodium thiocyanate, NaSCN), and two partitioning tracers (tertiary butyl alcohol, TBA, and isopropyl alcohol, IPA).

All tracers were injected in small slugs on the same day except for TBA, which was injected in a small slug 20 days later. Tracer sampling continued for 826 days after injection of the first set of tracers. The tracer injection pattern is shown in **Fig. 11**. Detailed information for injection locations and the amounts of each tracer injected can be found elsewhere.[28] We use averaged well-production and injection rates over the life of the project for our work. The average production and injection rates for all wells are summarized in **Fig. 12**.

We can use the conservative tracers (Tritium and NaSCN) to obtain permeability distribution in the study area. However, the Tritium response may be affected by a chromatographic delay because of tritium exchange with immobile hydrogen.[26] We selected NaSCN as the conservative tracer for permeability inversion. Totally 5,655 lbs of NaSCN was injected into Well 38. The observed tracer responses are shown in **Fig. 13**.

Choice of an Initial Model. During inverse modeling, a proper selection of the initial model can be critical to ensure a plausible solution. Such an initial model should incorporate all available prior information. For our simulation studies, we use a 31×45×6 grid which corresponds to 100×100 ft gridblocks areally and 2 to 4 ft vertically. A total of 141 core samples were available for analysis. We did not have well- and depth-specific data but rather a summary of the core data for all wells. A histogram and cumulative distribution of the core permeabilities are shown in **Fig. 14**. The core data indicated a fair degree of permeability heterogeneity in the reservoir but only slight variation in porosity. For the initial model, we used a uniform value of porosity and a heterogeneous permeability field generated using Sequential Gaussian Simulation[29] based on well data (**Fig. 15)**.

Estimating permeability. We matched the NaSCN data to obtain the permeability distribution in the study area using the three different approaches: travel-time inversion, generalized travel-time inversion, and amplitude inversion. **Fig. 13** shows the NaSCN responses from a streamline simulator using the initial permeability field. Also, superimposed are the observed NaSCN concentrations. Clearly, there is a large difference between the calculated and observed NaSCN response. **Fig. 16** shows the NaSCN concentration match after travel-time inversion. The peak arrival times are now in agreement with the observed data. The tracer concentration amplitudes show improvement but the overall match is still not satisfactory. **Fig. 17** is the NaSCN concentration match after the generalized travel-time inversion. From Fig. 17 we can see that not only are the peak-arrival times well matched, but the calculated concentration amplitudes are also in close agreement with the observed data. This shows that generalized travel-time inversion is an effective one-step inversion process. **Fig. 18** displays the NaSCN concentration match after direct amplitude inversion. Clearly the calculated responses have changed very little from the initial responses. The results indicate that amplitude inversion may not be as effective as the travel-time inversion, particularly when the initial model is far from the solution. Generalized

travel-time inversion stands out as the best among the three inversion methods. This is also demonstrated by **Fig. 19**, which shows the convergence behavior for travel-time inversion, generalized travel-time inversion, and amplitude inversion for the field case.

Fig. 20 summarizes nonlinearity for the three inversion methods. The measure of nonlinearity for the field example is given by the maximum amongst the three producers. Amplitude inversion displays the highest measure of nonlinearity, about 200 to 250, while travel-time inversion is quasi-linear with a nonlinearity of around 0.2 to 0.4. The generalized travel-time inversion is between these two cases in terms of non-linearity measure. However, it is one order of magnitude larger than the travel-time inversion while two orders of magnitude smaller than that of the amplitude inversion. Generalized travel-time inversion keeps most of the favorable features of travel-time inversion and has a much better tracer-concentration amplitude match than travel-time inversion. The severe nonlinearity of the amplitude inversion is partly responsible for its poor performance for the field case.

Fig. 21 shows the permeability fields derived by travel-time inversion and generalized travel-time inversion. **Fig. 22** shows the permeability change after travel-time inversion and generalized travel-time inversion. Comparing these with the permeability distribution obtained by Allison *et al.*[27] by a manual matching of the tracer data using a finite-difference simulator reveals a general agreement between the location of the permeability multipliers and the areas with higher and lower permeability values. For example, we see that the high-permeability multipliers in the upper-right and central-left areas and the low-permeability multipliers in the lower-left areas in **Fig. 23** agree with the positive and negative changes shown in Fig. 22.

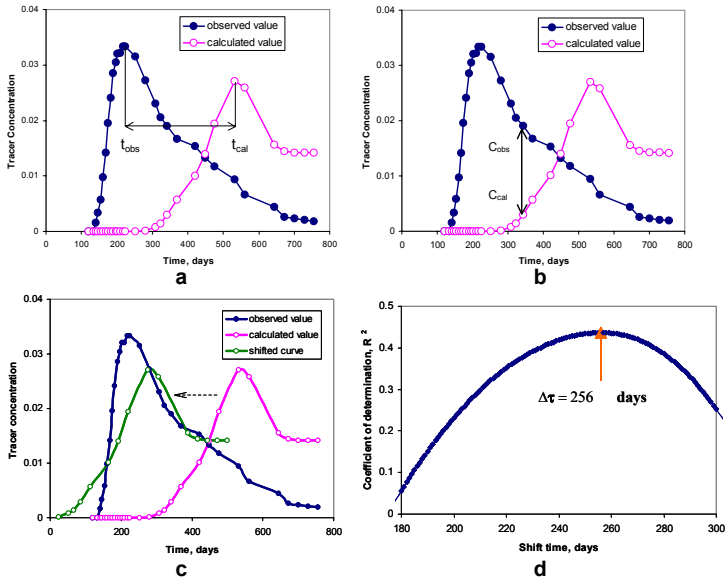

Fig. 1—Illustration of (a) travel-time inversion, (b) amplitude inversion, (c) generalized travel-time inversion, and (d) best time shift.

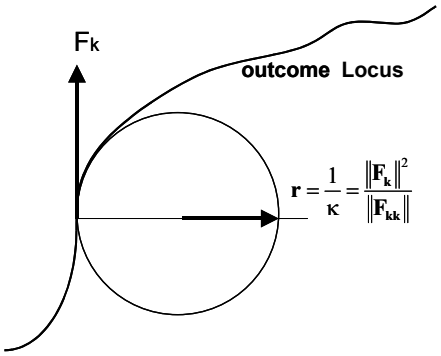

Fig. 2— Geometric meaning of the measure of nonlinearity.

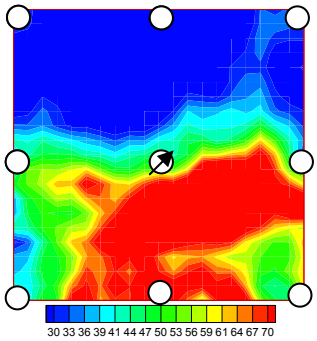

Fig. 3—Synthetic permeability distribution for the 9-spot case.

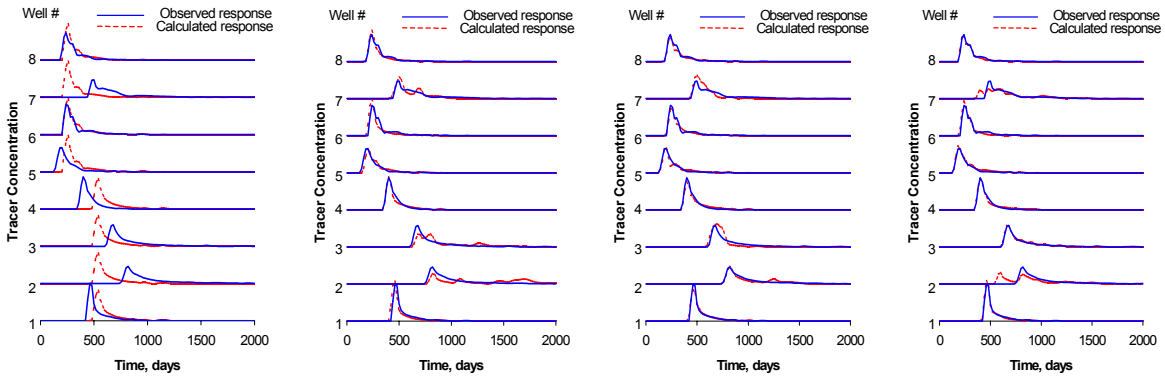

Fig. 4—Tracer response (a) for uniform initial permeability, (b) after peak arrival-time inversion, (c) after generalized travel-time inversion, and (d) after direct amplitude inversion.

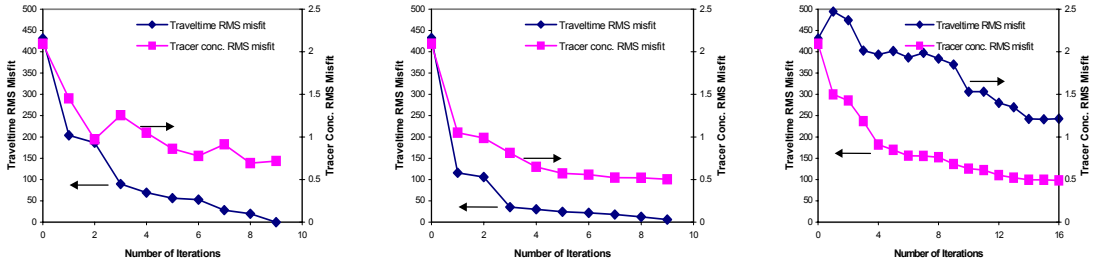

a b c

Fig. 5—Travel-time and tracer concentration misfit for (a) travel-time, (b) generalized travel-time, and (c) amplitude inversion.

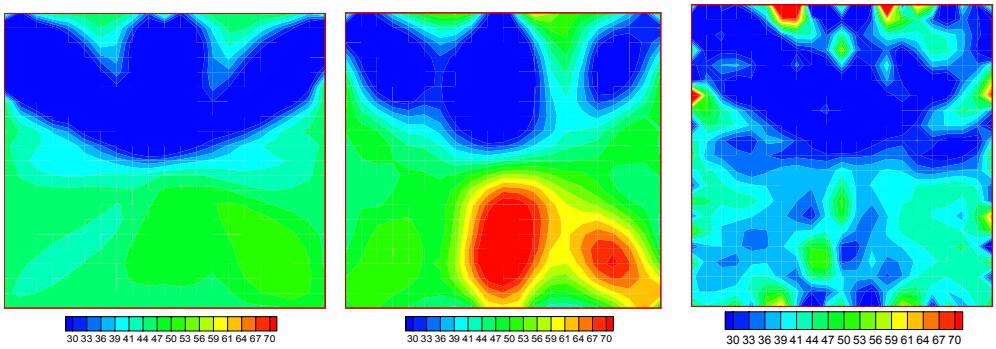

a b c

Fig. 6—Estimated permeability distribution for the 9-spot case (a) after travel-time inversion, (b) after generalized travel-time inversion, and (c) after amplitude inversion.

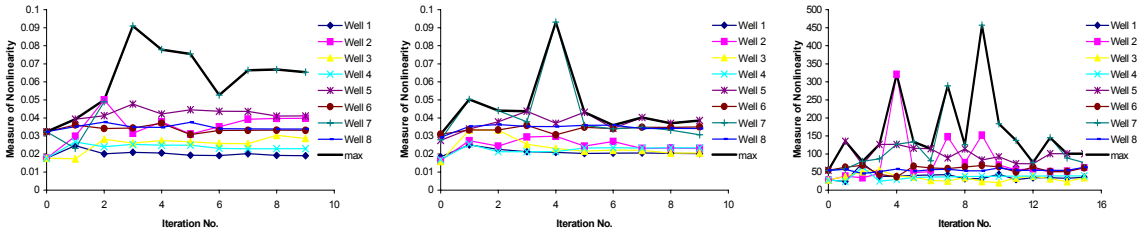

a b c

Fig. 7—Measure of nonlinearity for (a) travel-time inversion, (b) generalized travel-time inversion, and (c) amplitude inversion.

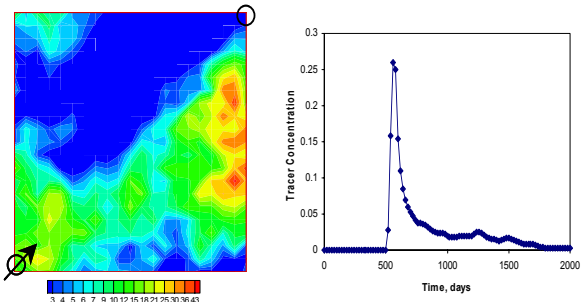

a b

Fig. 8—Tracer response for a ¼ five-spot heterogeneous case.

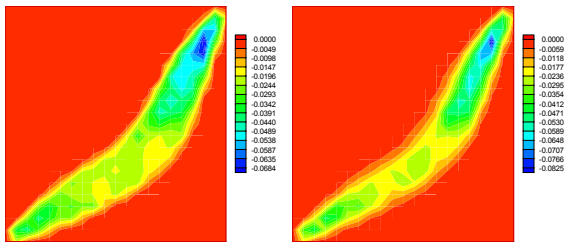

a b

Fig. 9—Sensitivity for (a) travel-time and (b) generalized travel- time inversion.

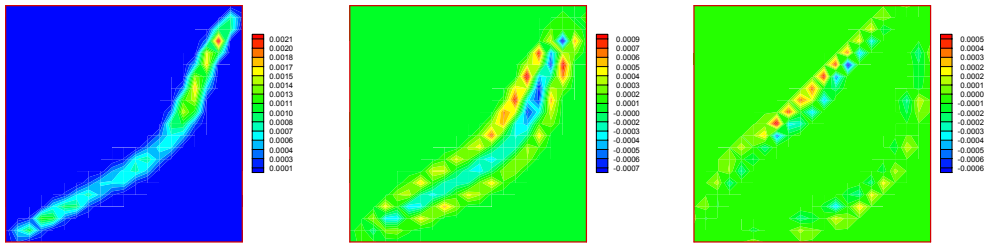

a b c

Fig. 10—Sensitivity distribution for amplitude inversion (a) before peak time, (b) at peak time, and (c) after peak time.

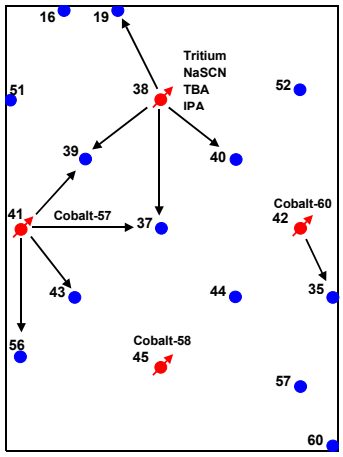

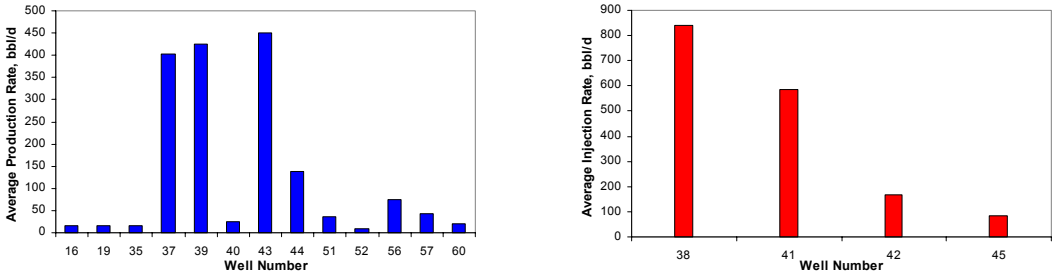

a b

Fig. 12— (a) Well production rates and (b) well injection rates.

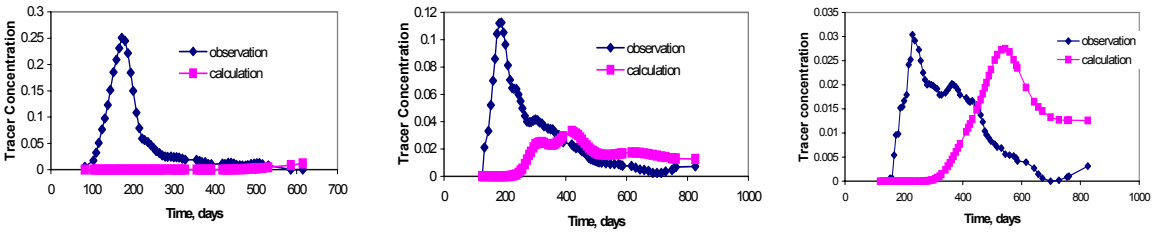

a b c

Fig. 13—NaSCN tracer response for the initial permeability field at (a) Well 40, (b) Well 37, and (c) Well 39.

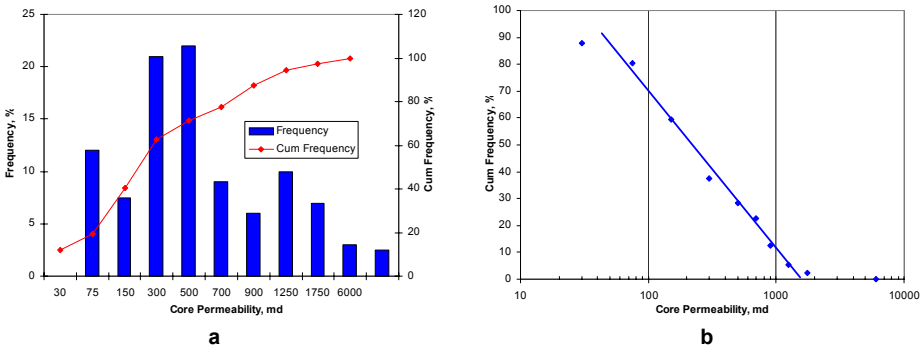

Fig. 14—Core permeability (a) histogram and (b) cumulative distribution.

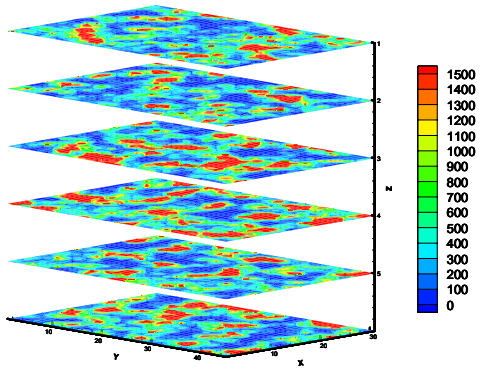

Fig. 15—Initial permeability distribution for the Ranger field case.

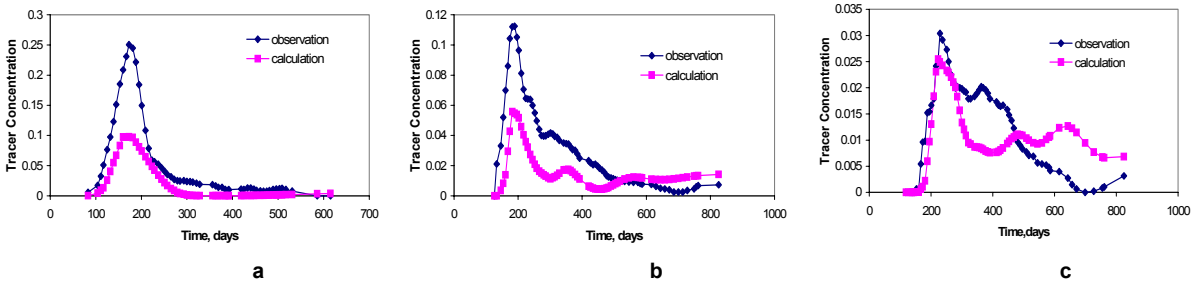

Fig. 16—NaSCN tracer response after travel-time inversion at (a) Well 40, (b) Well 37, and (c) Well 39.

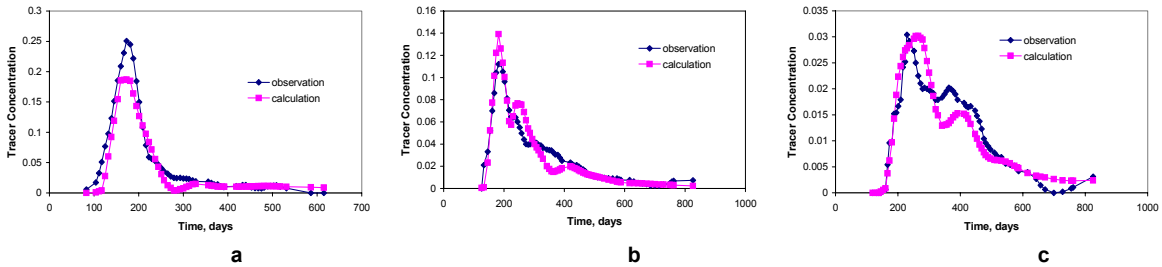

Fig. 17—NaSCN tracer response after generalized travel-time inversion at (a) Well 40, (b) Well 37, and (c) Well 39.

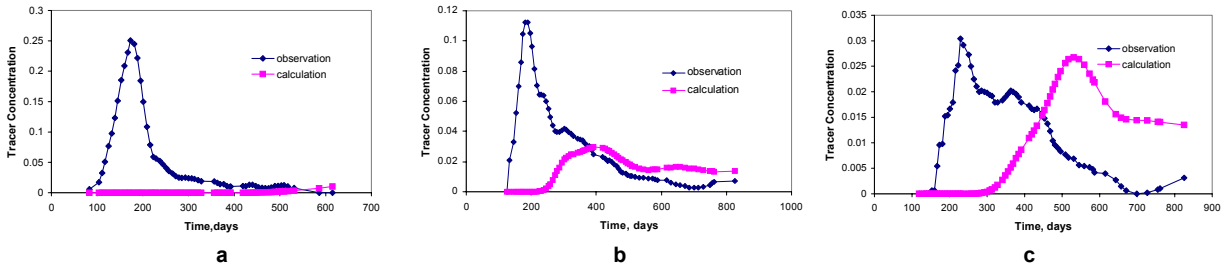

Fig. 18—NaSCN tracer response after direct amplitude inversion at (a) Well 40, (b) Well 37, and (c) Well 39.

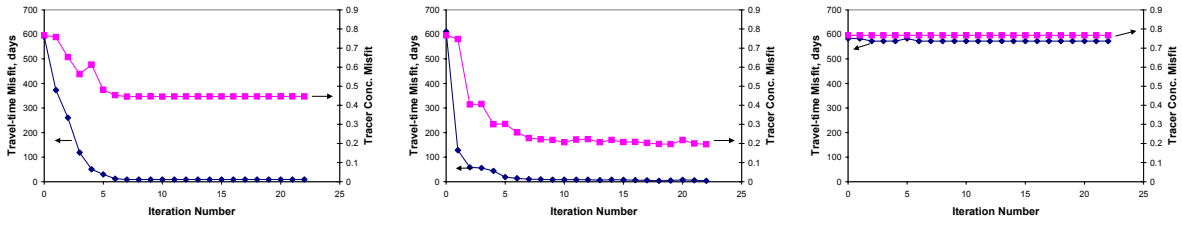

Fig. 19—Travel-time and tracer concentration misfit for (a) travel-time inversion, (b) generalized travel-time inversion, and (c) amplitude inversion.

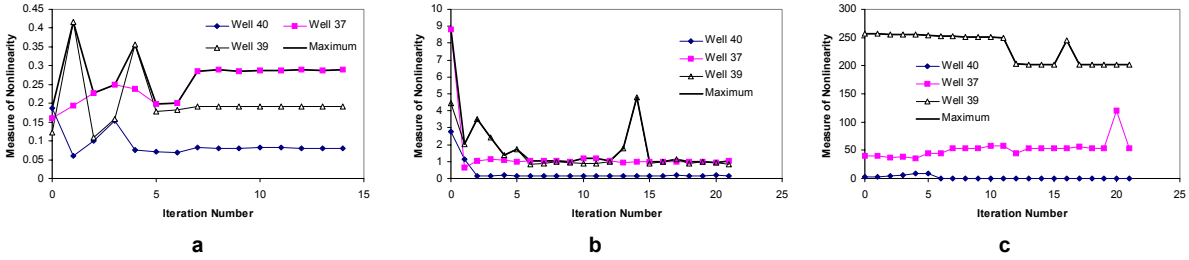

Fig. 20—Measure of nonlinearity for (a) travel-time inversion, (b) generalized travel-time inversion, and (c) amplitude inversion.

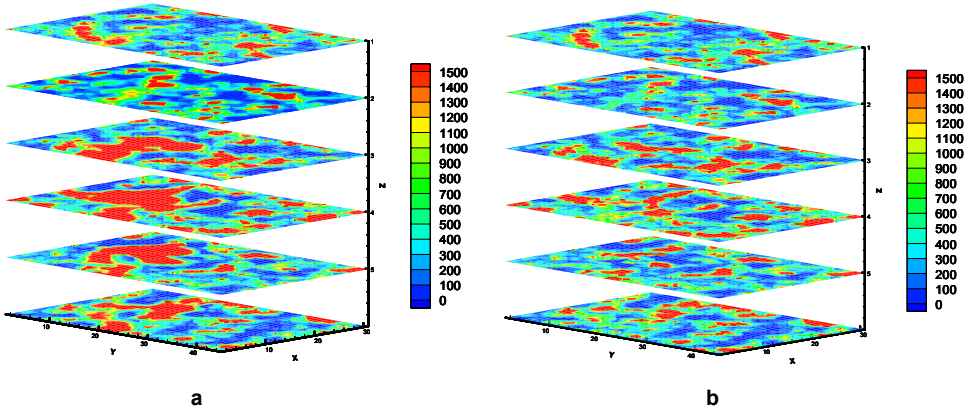

Fig. 21—Derived permeability field after NaSCN concentration match by (a)generalized travel-time inversion and (b) travel-time inversion.

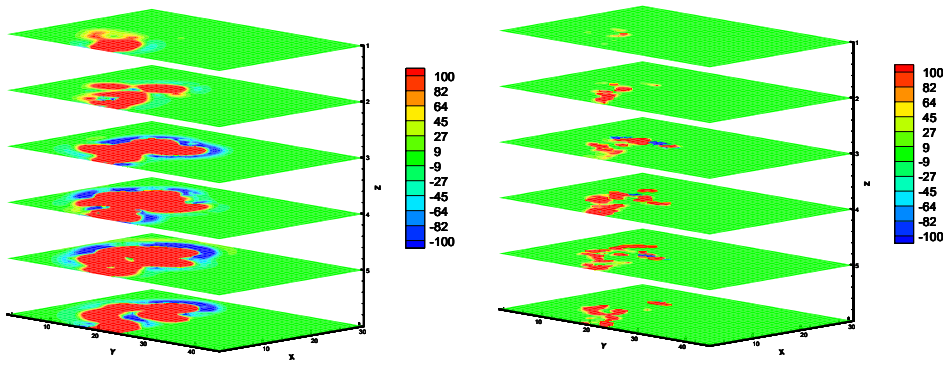

a b

Fig.22—Permeability change after (a) gereralized travel-time match and (b) travel-time match.

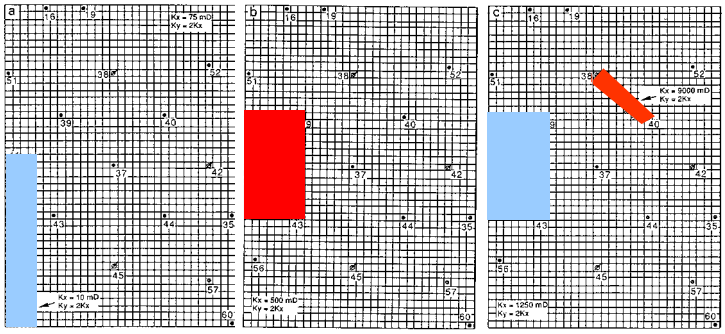

Fig. 23—Permeability multipliers for Layers 1, 2, and 3 from the finite-difference history match (Allison *et al.*[26]).

RESULTS AND DISCUSSION: PART II

Multiscale Data Integration for Reservoir Characterization

Introduction

The principal goal of reservoir characterization is to provide a reservoir model for accurate reservoir performance prediction. Integrating various data sources is an essential task in reservoir characterization. In general, we have hard data such as well logs and cores and soft data such as seismic traces, production history, a conceptual depositional model, and regional geological analysis. Seismic data in particular can play a major role in enhancing the geological model. It can be a block constraint when generating property distributions at a finer scale. However, integrating such information into the reservoir model is nontrivial. This is because different data sources scan different length-scales of heterogeneity and can have different degree of precision.[1] It is essential that reservoir models preserve small-scale property variations observed in well logs and core measurements and capture the large-scale structure and continuity observed in global measures such as seismic and production data.

The large coverage area of seismic data has established that such data sources can play a major role in characterizing the reservoir. Most applications of seismic data for reservoir characterization have focused on the relationship between seismic attributes such as amplitudes or impedance and porosity.[2,3] Two basic approaches have been adopted for integrating seismic data into reservoir models. For high-resolution seismic data, several geostatistical techniques such as cokriging and collocated cokriging have been proposed to estimate areal distribution of porosity.[45,6] On the lower-resolution spectrum, there are methods to combine multiscale data where seismic data imposes a block constraint for the finer scale.[3,4,6,78,91011] These include techniques such as Sequential Gaussian Simulation with Block Kriging (SGSBK)[3] and Bayesian updating of point kriging.[1011] Most kriging-based methods are restricted to multi-Gaussian and stationary random fields. They therefore require data transformation and variogram construction.[3,4,6,78,91011] In practice, variogram modeling with a limited data set can be difficult and strongly user dependent. Improper variograms can lead to errors and inaccuracies in the estimation. Thus, one might also need to consider the uncertainty in variogram models during estimation.[12] However, conventional geostatistical methods do not provide an effective framework to take into account the uncertainty of the variogram. Furthermore, most of the multiscale integration algorithms assume a linear relationship between the scales.

An alternative approach to traditional geostatistical methods is based on multiscale Markov Random Fields (MRF) that can effectively integrate diverse data sources into high-resolution reservoir models. MRF has been widely applied in imaging processing[1314,15] and spatial modeling. In the oil industry, this technique is relatively new. There are limited applications in determining the reservoir facies[1617] distribution and spatial modeling of reservoir properties using synthetic examples.[18] However, field-scale application of MRF has remained a challenging goal.

We further investigate our previously proposed method[18] with the main objective of gaining insight on the practical implementation of this technique by a field application in the Middle East. The particular field studied here, the CNR field in Saudi Arabia is located south of Riyadh and produces superlight, sweet crude oil from the Unayzah Formation, a late Permian clastic

reservoir. Our goal is to generate 3D high-resolution porosity model by integrating seismic and well log data via MRF.

Background and Methodology

The integration of seismic data and well data must account for the difference in scales and precision of the data types. Our proposed method is a Bayesian approach to spatial modeling based on MRF and multi-resolution algorithms in image analysis. Broadly, the method consists of two major parts (i) construction of a posterior distribution for multiscale data integration using a hierarchical model and (ii) implementing MCMC to explore the posterior distribution.

Construction of a posterior distribution for multiscale data integration. A multi-resolution MRF provides an efficient framework to integrate different scales of data hierarchically, provided that the coarse scale resolution is dependent on the next fine scale resolution.[13,14,19,20] In general, a hierarchical conditional model over scales 1,…, N (from fine to coarse) can be expressed in terms of the product of conditional distributions

$$\pi(x^1,...,x^N) = \pi(x^1)\prod_{n=2}^{N}\pi(x^n \mid x^{n-1}) \tag{1}$$

where $\pi(x^n)$, n = 1,…, N, are MRF models at each scale, and the terms $\pi(x^n \mid x^{n-1})$ express the statistical interactions between different scales. This approach links the various scales stochastically in a direct Bayesian hierarchical modeling framework (**Fig. 1**). Knowing the fine scale field x^n does not completely determine the field at a coarser scale x^{n+1}, but depending on the extent of the dependence structure modeled and estimated, influences the distribution at the coarser scales to a greater or lesser extent. This enables us to address multiscale problems accounting for the scale and precision of the data at various levels.

For clarity of exposition, a hierarchical model for reconciling two different scales of data will be considered below.

$$\pi(x^1, x^2) = \pi(x^1)\pi(x^2 \mid x^1) = \pi(x^2)\pi(x^1 \mid x^2) \tag{2}$$

From this equation, the posterior distribution of the fine scale random field indexed by 1 given a coarse scale random field indexed by 2 can be derived as follows

$$\begin{aligned}\pi(\mathbf{x}^1 \mid \mathbf{x}^2) &= \frac{\pi(\mathbf{x}^1, \mathbf{x}^2)}{\pi(\mathbf{x}^2)} = \frac{\pi(\mathbf{x}^1)\pi(\mathbf{x}^2 \mid \mathbf{x}^1)}{\pi(\mathbf{x}^2)} \\ &\propto \pi(\mathbf{x}^1)\pi(\mathbf{x}^2 \mid \mathbf{x}^1)\end{aligned} \tag{3}$$

In Eq. 3, $\pi(\mathbf{x}^1)$ is a prior distribution of the fine-scale represented by an MRF. We can generalize Eq. 3 to incorporate uncertainty in the prior spatial model

$$\begin{aligned}\pi(\mathbf{x}_n^1 \mid \theta, \mathbf{x}_o^1, \mathbf{x}^2) &\propto \pi(\mathbf{x}_n^1, \mathbf{x}_o^1 \mid \theta)\pi(\mathbf{x}^2 \mid \mathbf{x}^1) \\ &\propto \pi(\mathbf{x}^1 \mid \theta)\pi(\mathbf{x}^2 \mid \mathbf{x}^1)\end{aligned} \tag{4}$$

In Eq. 4 we have split $\mathbf{x}^1$ into its two components: $\mathbf{x}_n^1$ represents simulated (unknown) fine scale values and $\mathbf{x}_o^1$ are the conditioning points. Also, θ denotes a parameter in the MRF that controls the variance in the fine-scale spatial model.

Thus, the posterior distribution is proportional to the product of three major terms as follows:

1. $\pi(\mathbf{x}^1 \mid \theta)$ represents the joint spatial distribution of $\mathbf{x}^1$ modeled by a MRF with a scale parameter, θ.

2. $\pi(\mathbf{x}^2 \mid \mathbf{x}^1)$ is a stochastic link model for scale to scale transitions.

Spatial modeling using MRF. In the petroleum literature, several MRF models for discrete data such as Ising, Potts and Strauss models etc. have been used to model the distribution of rock types or sedimentary facies in the reservoir.[21,15,22,17] However, the use of MRF for spatial modeling of continuous data such as permeability and porosity has been rather limited. By far the most prevalent spatial MRF model for continuous data has been the auto-normal model[21,15,22,17,23], the so called Gaussian Markov Random Fields (GMRF), although extensions to non-Gaussian distributions are possible.[23]

GMRF specify the conditional probability of x_i^1 to be normally distributed with a mean that depends upon the elements of its neighborhood, N_i (**Fig. 2**)

$$\pi(x_i^1 \mid x_j^1, j \in N_i) = \frac{1}{\sqrt{2\pi\sigma^2}} \exp\left\{-\frac{1}{2\sigma^2}\left\{x_i^1 - \sum_{j\in N_i} w_{ij} x_j^1\right\}^2\right\} \tag{5}$$

where w_{ij} can be viewed as interaction coefficients and N_i is the neighborhood set of site *i*. This leads to the following joint distribution of $\mathbf{x}^1 = (x_1^1, x_2^1, \cdots, x_n^1)^T$,

$$\pi(\mathbf{x}^1) = \frac{1}{\sqrt{(2\pi\sigma^2)^n}} \mid \mathbf{W} \mid^{1/2} \exp\left\{-\frac{1}{2\sigma^2}\mathbf{x}^{1T}\mathbf{W}\mathbf{x}^1\right\} \tag{6}$$

where **W** is the *n* x *n* interaction matrix whose diagonal elements are unity and off-diagonal elements are $-w_{ij}$. Note the w_{ij} must be specified so that **W** is positive definite.

The model in Eq. 6 assumes that the conditional variance $\mathrm{var}(x_i^1 \mid x_j^1, j \in N_i) = \sigma^2$ is a constant. This may not be appropriate for heterogeneous environments where the number of neighbors and the local conditional variance might vary. We utilize the following pair-wise difference prior (PDP) conditional distribution that more effectively captures the local properties of the spatial process *x* [2425,26]

$$\pi(x_i^1 \mid x_j^1, j \in N_i) \propto \theta^{1/2} \exp\left\{-\frac{1}{2}\theta \sum_{j\in N_i} \beta_{ij}(x_i^1 - x_j^1)^2\right\} \tag{7}$$

In Eq. 7 β_{ij} are prespecified local spatial parameters with β_{ij}=0 unless *i* and *j* are neighbors and θ is a scale parameter controlling the variance in the fine-scale distribution. Eq. 7 is equivalent to a normal local conditional prior distribution of the form

$$\pi(x_i^1 \mid x_j^1, j \in N_i) \sim N\left(\sum_{j\in N_i} \frac{\beta_{ij} x_j^1}{\beta_{i+}}, \frac{1}{\theta\beta_{i+}}\right) \tag{8}$$

where $\beta_{i+} = \sum_{j\in N_i} \beta_{ij}$. Note that in Eq. 8 both the mean and the variance can be locally varying, allowing for non-stationary spatial modeling.

Similarly, Eq.7 leads to the following joint distribution of $\mathbf{x}^1 = (x_1^1, x_2^1, \cdots, x_n^1)^T$,

$$\pi(\mathbf{x}^1) \propto \theta^{n/2} \mid \mathbf{B} \mid^{1/2} \exp\left\{-\frac{1}{2}\theta\mathbf{x}^{1T}\mathbf{B}\mathbf{x}^1\right\} \tag{9}$$

where **B** is the *nxn* precision matrix whose diagonal elements are $\beta_{i+} = \sum_{j \in N_i} \beta_{ij}$ and off-diagonal elements are $-\beta_{ij}$. Note the β_{ij} must be specified so that **B** is positive semi-definite and symmetric.

The choice of model parameter, β. The selection of β_{ij} in a MRF allows us to incorporate prior subjective and geologic knowledge into the model. Unfortunately, the estimation of β_{ij} is not trivial. Several techniques have been proposed in the literature for the optimal estimation of β_{ij}.[21,2326,27] For example, Devine et al.[28] propose forming a matrix of interregional distance. β_{ij} is then set equal to *g(dij)* where g is a decreasing function inversely proportional to the distance. The simplest choice is $\beta_{ij} = 1$ if *i* and *j* are adjacent locations. [27]

In some cases, one might also choose to specify β_{ij} to reflect known local and global spatial properties of $\mathbf{x}^1$ such as distance between sites.[27,29] Rue and Tjelmeland[29] demonstrated how to fit a GMRF to a known stationary Gaussian Random Field (GRF) on a torus through a minimization scheme. Caers[30] further utilized this approach for GMRF to reproduce a prior covariance. Their approach is briefly discussed below with an illustrative example.

Suppose we have a stationary GRF with covariance **G**. In a GMRF, with a certain covariance matrix **M** (which is the inverse of the precision matrix **W**), an optimization technique is applied to find w_{ij} that minimizes

$$O(\mathbf{W}) = \sum_{i=1}^{n_c} \sum_{j=1}^{n_r} \left(M_{11ij}(\mathbf{W}) - G_{11ij} \right)^2 \xi_{ij} \tag{10}$$

where M_{11ij} and G_{11ij} are the covariances between 11 site and ij site in GMRF and GRF respectively, ξ_{ij} is user defined weighting factor. For a detailed explanation, refer to Rue and Tjelmeland[29] and Caers[30]. To achieve computational efficiency for large lattices, Fast Fourier Transform (FFT) algorithm is used.

To illustrate this approach, let us consider a simple 2D example on a 64x64 grid, using an isotropic exponential variogram with range equal to 15 grid-blocks. The neighborhood template is comprised of the 25 nodes as shown in **Fig. 3** and the *w*'s calculated using the above scheme are given in **Fig. 4**. The fitted covariance **M**(**W**), using the above-mentioned FFT approach is shown in **Fig. 5**. With the chosen template, a good match is obtained. **Fig. 6** shows a single simulated realization obtained using the GMRF. When compared to the actual reference realization, the simulated realization shows good agreement.

Once β_{ij} which controls the spatial dependence structure of *x* are specified, the joint spatial distribution of $\mathbf{x}^1$ can now be determined by a product of its conditional distributions in Eq. 7 as follows

$$\pi(\mathbf{x}^1 \mid \theta) \propto \theta^{n_1/2} \exp\left\{ -\frac{1}{2} \theta \sum_{i \sim j} \beta_{ij} (x_i^1 - x_j^1)^2 \right\} \tag{11}$$

where the sum is over all such pairs of neighbors (*i*,*j*) denoted by *i*~*j* and n_1 denotes total number of fine grid sites.

A stochastic link model between different scales. Assume two random fields at different scales to be linked so that each component of the coarse field will depend stochastically on the components of the finer grids within the coarse grid. For a link between resolution levels, let us consider a general Gaussian stochastic transformation model, usually nonlinear:

$$x_l^2 = f(x_1^1, x_2^1, \cdots, x_{n_l}^1) + \varepsilon_l \,, \tag{12}$$

where , n_l is the number of fine scale sites in each coarse site indexed by l, $\varepsilon_l \sim N(0, \sigma_2^2)$ that controls the precision of the coarse scale data. Eq. 12 may be approximated by a generalized additive model:

$$\varphi(x_l^2) = \sum_{i=1}^{n_l} \phi_i(x_i^1) + \varepsilon_l \,, \tag{13}$$

where ϕ , φ are transformation functions to account for different averaging schemes (linear or non-linear) between coarse scale and fine scale. In the case where $\varphi(u) = u$ and $\phi_s(v_s) = v_s / m_l$, Eq. 13 reduces to a simple linear averaging model[12,13] with Gaussian white noise between the different resolution levels. This leads to the following stochastic link model between the scales

$$\pi(\mathbf{x}^2 \mid \mathbf{x}^1) = \prod_{l=1}^{n_2} \frac{1}{\sigma_2 \sqrt{2\pi}} \exp\left\{ -\frac{1}{2{\sigma_2}^2} \left(x_l^2 - \frac{1}{m_l} \sum_{s=1}^{m_l} x_s^1 \right)^2 \right\} \tag{14}$$

where n_2 represents total number of coarse grid sites. If $\varphi(u) = u^{\omega} m_l$, $\phi_s(v_s) = {v_s}^{\omega}$, we have a ω-power averaging model[31] with Gaussian white noise between different resolution levels

$$\pi(\mathbf{x}^2 \mid \mathbf{x}^1) = \prod_{l=1}^{n_2} \frac{1}{\sigma_2 \sqrt{2\pi}} \exp\left\{ -\frac{1}{2{\sigma_2}^2} \left(m_l (x_l^2)^{\omega} - \sum_{s=1}^{m_l} (x_s^1)^{\omega} \right)^2 \right\}. \tag{15}$$

We can generalize such stochastic link models to incorporate as many scales as necessary.

Simulations using MCMC. The posterior distribution given by Eq. 14 provides a Bayesian framework for reconciling two different scales of data. We can generate multiple realizations from the posterior distribution using Markov Chain Monte Carlo(MCMC).[2425,26,32] MCMC is well known to be quite versatile and suitable for multivariate or high dimensional problems. The approach can handle non-Gaussian and complex posterior distributions.[26,32,33]

The essential idea of MCMC is Monte Carlo simulation utilizing Markov Chains. Two practical update algorithms for constructing a Markov Chain with a specified stationary distribution, $\pi(\mathbf{x})$ are Gibbs sampling and Metropolis-Hasting algorithms. Because MCMC methods are most conveniently built upon *full conditional* distributions, first we need to derive the full conditionals denoted by $\pi(x_i \mid x_{-i})$, which is the distribution of the i-th component x_i, conditioned on all the remaining components $x_{-i} = \{x_j : j \neq i\}$, $j = 1,\ldots,n$.

The joint posterior distribution determines each of the full conditionals. Thus random drawings from the target distribution $\pi(\mathbf{x})$ can be accomplished by a sequence of draws from full conditional distributions. The Gibbs sampling involves sampling from full conditional distributions. This algorithm, therefore, can not be used when the full conditionals have non-standard form or when sampling from the full conditional distribution is computationally difficult. On the other hand, Metropolis-Hastings algorithm is more general and does not require sampling from the full conditionals.[2425,26,32]

From the posterior distribution Eq. 15, the full conditional for $\mathbf{x}_n^1$

$$\pi(x_i^1 \mid \theta, x_{-i}^1, x_l^2) \propto \theta^{1/2} \exp\left\{-\frac{1}{2}\theta \sum_{j \in N_i} \beta_{ij}(x_i^1 - x_j^1)^2\right\}$$
$$\frac{1}{\sigma_2\sqrt{2\pi}} \exp\left\{-\frac{1}{2\sigma_2{}^2}\left(\varphi(x_l^2) - \sum_{s=1}^{m_l} \phi_s(x_s^1)\right)^2\right\} \tag{16}$$

where all $x_s^1 \in x_l^2$, $s = 1, \cdots, i-1, i, i+1, \cdots, m_l$.

We can now simulate $x_1^1, \cdots, x_n^1$ by updating according to the full conditionals.

Our MCMC scheme is carried out in practice by updating each x_i^1 using a Metropolis-Hasting step and θ using a Gibbs step. In the single component Metropolis-Hastings algorithm each candidate value, $x_i^{1^*}$ is generated from a prespecified proposal distribution. Assuming a symmetric proposal distribution, a candidate $x_i^{1^*}$ is accepted with a probability $\alpha(x_i^1, x_i^{1^*})$ where

$$\alpha(x_i^1, x_i^{1^*}) = \min\left\{1, \frac{\pi(x_i^{1^*} \mid \theta, x_{-i}^{1^*}, x_l^2)}{\pi(x_i^1 \mid \theta, x_{-i}^1, x_l^2)}\right\} \tag{17}$$

Here $\pi(x_i^1 \mid \theta, x_{-i}^1, x_l^2)$ is the full conditional distribution of x_i^1 given by Eq. 16.

Applications

We illustrate our approach using several examples that demonstrate the power and versatility of the method. The first synthetic example involves integration of sparse fine-scale data with coarse scale data. This is the situation encountered, for example, when we have well data and seismic data. The second example is a field example that involves integration of seismic data and fine-scale conditioning points representing the well data. The field is located in Saudi Arabia south of Riyadh and produces superlight oil from the Unayzah Formation, a late Permian siliclastic reservoir.

Sy**nthetic Example**: Integrating two different scales of data with anisotropy. This example involves generating fine-scale realizations of permeability based on limited fine-scale conditioning data and a coarse block constraint.

The reference permeability field in Fig. 7(a) shows a clear anisotropic structure. The permeability data is from a slab of Berea sandstone and has been extensively used in the literature.[34] This field consists of 40 by 40 air permeameter measurements taken from a 2 by 2 foot vertical slab of Berea sandstone. Note that the scale of permeability values is in millidarcies. We can see a low permeability streak along the North-West direction and high permeability regions in the upper right corner. A coarse permeability field is generated by geometric averaging of the fine scale reference field and adding Gaussian noise. **Fig. 7 (b)** shows the coarse scale permeability field. To take into account for the anisotropy in the fine scale permeability field, we define anisotropic neighborhood system on a lattice of regular sites (**Fig. 2 (b)**). Based on 64 fine scale conditioning data and the coarse scale permeability field, fine scale realizations are sampled from the posterior distribution using MCMC. **Fig. 7 (c)** shows one such realization simulated by MCMC. **Fig. 8** shows the cross plot of simulated permeability versus the true

permeability. **Fig. 9** demonstrates that the coarse scale constraint is preserved by the simulated permeability distribution.

Field Application: In this field application, our goal is to obtain a high-resolution porosity model based on well log and seismic data. The well log data represents the sparse fine-scale information and the seismic data are the coarse scale data.

Geological Aspects. The CNR Field is located south of Riyadh in the central Saudi Arabian basin. The CNR Field produces superlight, sweet crude oil from the Unayzah Formation, a late Permian clastic reservoir.The area under study (**Fig. 10**) is approximately 100 sq km (38.6 sq miles) in size. The seismic data over the area include a 3-D post stack data set. The area includes 9 wells; A, B, C, D, E, F, G, H, I.

The Permian Unayzah Formation is a continental clastics consisting of braid-plain and eolian sands and floodplain silts. The Unayzah formation is bounded by two major unconformities: the Pre-Unayzah Unconformity (PUU) at the formation base eroding into the Qusaiba marine shales, the source rock for Central Arabia, and the Pre-Khuff Unconformity (PKU) at the formation top, overlain by the Khuff marine clastic sediments. The stratigraphic column of the 'Unayzah Formation is shown in **Fig. 12.** Three major depositional cycles are recognized within Unayzah formation (in descending order): Unayzah A, B, and C (**Fig. 12**). Unayzah B reservoir falls within one of these major cycles.

Unayzah B reservoir consists of wadi fill and alluvial fan to braided-plain glacio-fluvial deposits infilling an irregular topography following the cessation of the Hercynian Orogeny.[36]

Unayzah B reservoir well spacing is about 2 km. With such a coarse well spacing, it is difficult to characterize the reservoir heterogeneity with well data alone. Integration of the 3-D seismic data with petrophysical information has improved the mapping of porosity distribution in Unayzah B reservoir.

Unayzah B porosity varies from about 30% to less than 10%. A well-to-seismic calibration has been carried out to interpret the top and base of Unayzah B reservoir. Maximum acoustic seismic amplitudes were extracted on the seismic picked top horizon of the Unayzah B reservoir for our study.

Approach. The two major steps involved in the proposed approach can be outlined as follows:

1) Derive a relationship between the neutron porosity and seismic amplitudes.
2) Integrate the seismically derived coarse-scale porosity with fine-scale well data to generate a 3-D field-wide porosity distribution using the MRF.

Step 1: Correlation between Seismic data and porosity

Seismic map, which is a source of dense information, is considered as soft data that is related to the average porosity within seismic resolution. Well log porosity values, which are sparse yet contain high resolution vertical information, are considered as hard data. The seismic map is represented by the maximum acoustic seismic amplitudes that were extracted from the seismic picked top horizon of the Unayzah B reservoir. The seismic data with a resolution acquisition of 100mx100m is shown in **Fig. 13**. Well log data is basically neutron porosity values. **Table 1** shows the location of wells, the formation top and bottom depth. **Fig. 14** shows the distribution of wells in the field.

While well data provide excellent resolution in the vertical direction, they represent a small portion of the actual field. On the other hand, seismic data are generally less precise but more abundant. We consider in our approach that the average of the cell values in any one vertical column of grid cells is constrained by the value of the seismic map over that column. Because seismic data resolution deteriorates with depth, we employ inverse distance weighting while calculating average porosity values from well logs to give more weights to porosities closest to the value of the seismic map as follows:

$$Z_{Average} = \frac{\sum_{i=1}^{n} (1/d_i) * Z_i}{\sum_{i=1}^{n} (1/d_i)} \tag{18}$$

where Z_i is the parameter or property that we want to average, d_i: distance, and $Z_{Average}$: is the average of parameter Z_i according to inverse distance. **Table 2** shows the results of the average of porosity for each well according to Eq. 18.

The next step is to define the seismic amplitude values at the top of the formation for each well. **Table 3** shows these values for each well. With the average values of neutron porosity and seismic amplitude, we obtain a correlation between these parameters. Several linear regression models were tested e.g. average neutron porosity vs. amplitude and average neutron porosity*thickness vs. amplitude. We concluded that the linear regression model that gave the best correlation coefficient was for average neutron porosity*thickness vs. amplitude which is consistent with models available in the literature.[37] **Fig. 15** shows the correlation between these variables and the correlation coefficient is 0.66. Using this correlation, we obtain a coarse scale distribution of porosity in the reservoir based on the seismic resolution. **Fig. 16** shows the seismically derived porosity distribution.

Step 2: Integration of seismically derived coarse- scale porosity with fine-scale well data using MRF.

The next step is generating fine-scale realizations of porosity based on the well log data and the coarse block seismically derived porosity values. The grid size for the 3D high-resolution porosity model is 65x69x32. The fine scale well data correspond to 9 wells in the field. The coarse scale data (65x69x1) is the seismically derived porosity values generated in step 1. Due to the limited numbers of conditioning points, a representative variogram is difficult to construct. Hence, we decided against utilizing variograms to calculate the spatial interaction coefficients β_{ij} as discussed before. Instead, we adopted the simplest choice of $\beta_{ij} = 1$ if i and j are adjacent locations. Using a single component Metropolis algorithm we explore the posterior distribution (Eq. 14) that incorporates information from the various scales accounting for the precision of the data. **Fig. 17** shows one of the realizations obtained via the multiscale integration procedure. **Fig. 18** compares the true average porosity versus the simulated average porosity. As expected, the fine scale realization reproduces almost perfectly the coarse scale block average.

Sensitivity Analysis: In MRF approach, Eq. 16 expresses the full conditional distribution. In this equation, θ is a scale parameter controlling the variance in the fine-scale distribution. In the Bayesian inference for multiscale integration, which is the base of MRF approach, considering the uncertainty of θ is trivial. Lee et al.[18] have showed that generalizing Eq. 4 by including a

prior model for θ, one can easily quantify the uncertainty in the prior spatial model. Eq. 4 will be modified as follows:

$$\begin{aligned}\pi(\mathbf{x}_n^1,\theta \mid \mathbf{x}_o^1,\mathbf{x}^2) &\propto \pi(\mathbf{x}_n^1,\mathbf{x}_o^1 \mid \theta)\pi(\mathbf{x}^2 \mid \mathbf{x}^1)\pi(\theta) \\ &\propto \pi(\mathbf{x}^1 \mid \theta)\pi(\mathbf{x}^2 \mid \mathbf{x}^1)\pi(\theta)\end{aligned} \tag{18}$$

Another parameter, σ_2 in Eq. 16, controls the precision of information at different scales. The value of σ_2 will depend on how much weight one want to exert for the coarse scale information. The higher the value of σ_2, lesser will be the impact of the seismic data on the fine-scale realization. In our field example, a sensitivity analysis for σ_2 was conducted to observe its effect on the final high resolution porosity model. By comparing **Fig. 18** and **Fig. 19,** we can see that the influence of the coarse-scale constraint is practically non-existent when we change from σ_2=0.0001 to σ_2=0.1, respectively.

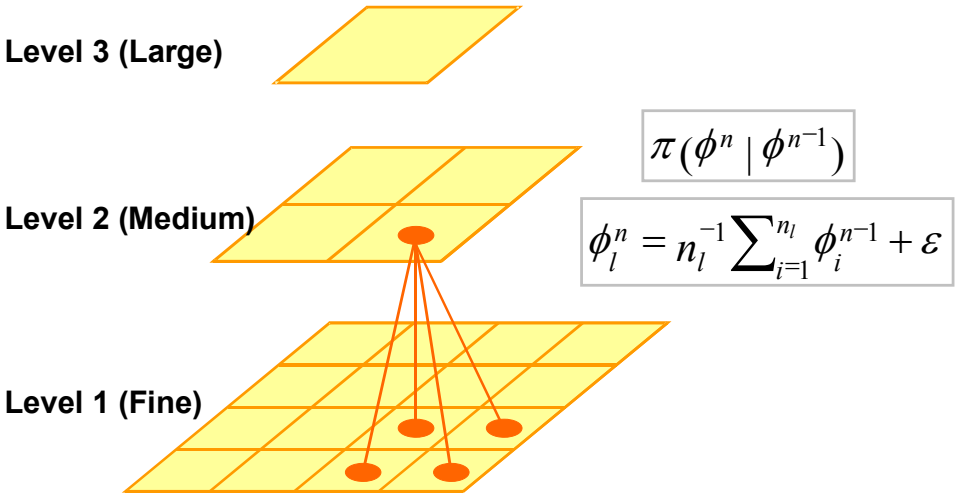

Fig. 1-An illustration of hierarchical estimation structure. An example of "link" between two different scales of data according to a local stochastic transformation.

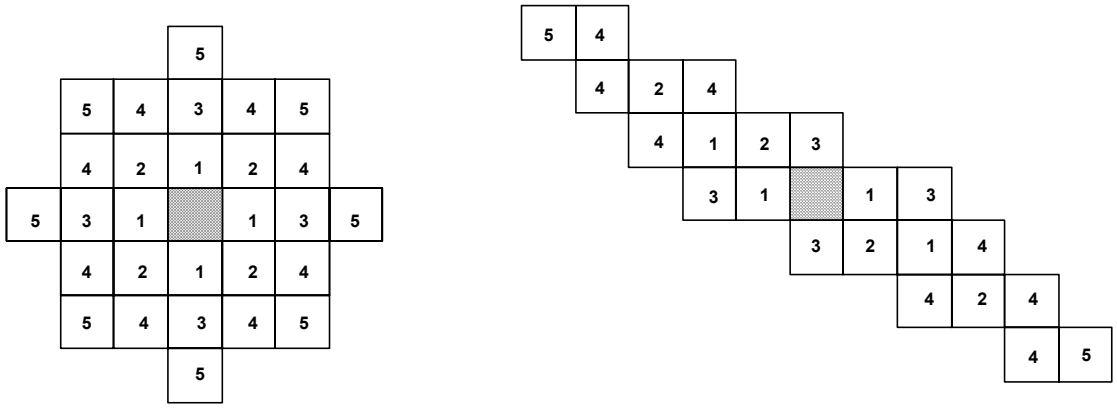

(a) Isotropic template (b) Anisotropic template

Fig. 2-Two neighborhood systems with respect to a generalized Euclidean distance on a two-dimensional lattice. The numbers (e.g.,1, …, 5) in the template indicate the order of the neighborhood system.

w_{22}	w_{21}	w_{20}	w_{21}	w_{22}
w_{21}	w_{11}	w_{10}	w_{11}	w_{21}
w_{20}	w_{10}	w_{00}	w_{10}	w_{20}
w_{21}	w_{11}	w_{10}	w_{11}	w_{21}
w_{22}	w_{21}	w_{20}	w_{21}	w_{22}

Fig. 3-A 25x25 grid isotropic template used for the calculation and the corresponding w's.

-0.018	-0.018	-0.032	-0.018	-0.018
-0.018	0.1736	0.1650	0.1736	-0.018
-0.032	0.1650	1.0	0.1650	-0.032
-0.018	0.1736	0.1650	0.1736	-0.018
-0.018	-0.018	-0.032	-0.018	-0.018

Fig. 4-Estimated w's using the two-way FFT.

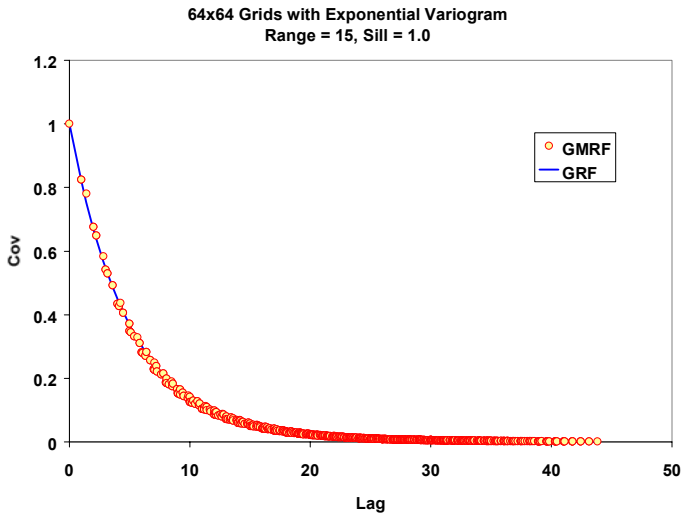

Fig. 5-The target (solid) model fitted with the covariance of MRF calculated using the two-way FFT.

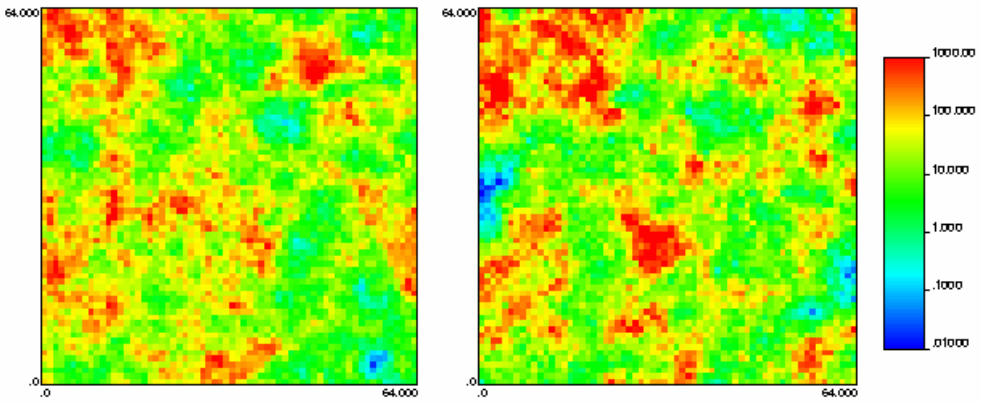

(a) **(b)**

Fig. 6-The reference field (a) compared to simulated realization using GMRF (b)

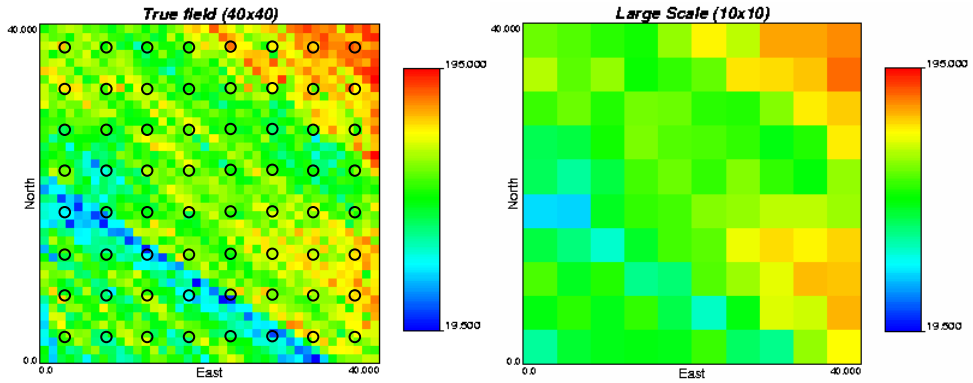

(a) (b)

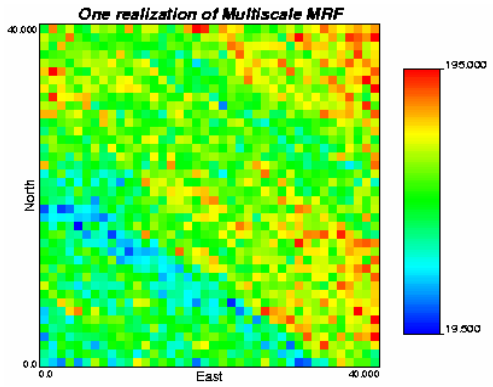

(c)

Fig. 7-Synthetic example for multiscale data integration with the consideration of anisotropy. (a) Reference Berea Sandstone permeability field on fine scale 40x40 grid (logarithmic scale); (b) Large scale permeability field generated by geometric averaging plus correlated error (10x10); (c) One realization of fine scale permeability field generated by MRF and MCMC.

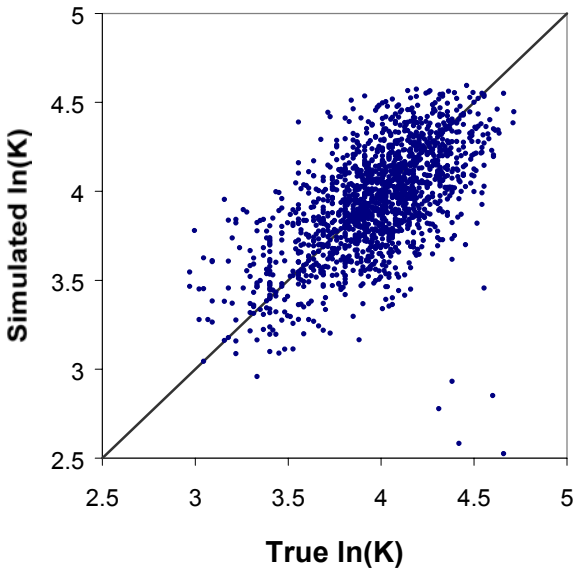

Fig. 8-Cross plot of true permeability versus simulated permeability from a new approach based on multiscale MRF.

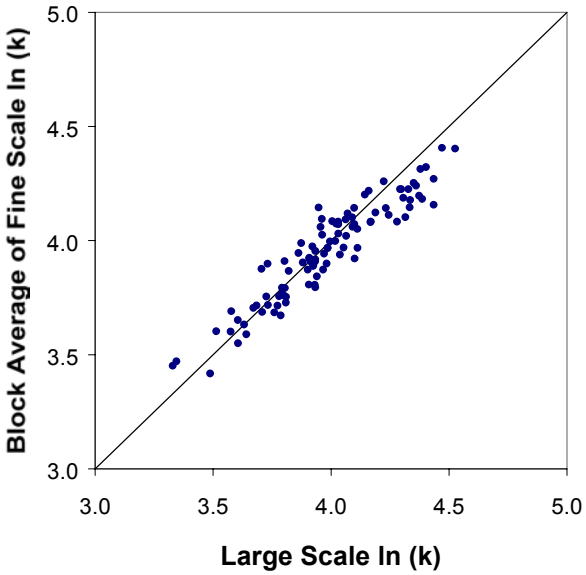

Fig. 9-Cross plot of simulated block average of fine scale ln(k) versus large scale block ln(k). Perfect reproduction of large scale block values corresponds to the diagonal line.

Fig. 10-Location map of the CNR Field in the central basin of Saudi Arabia

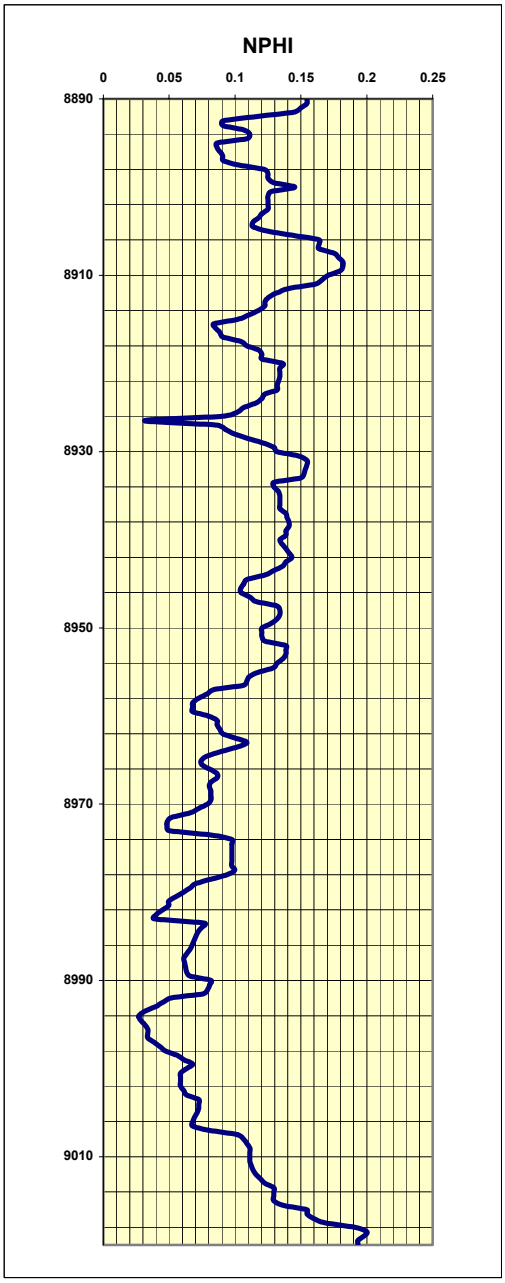

Fig. 11-Neutron porosity for one of the wells in the area of study.

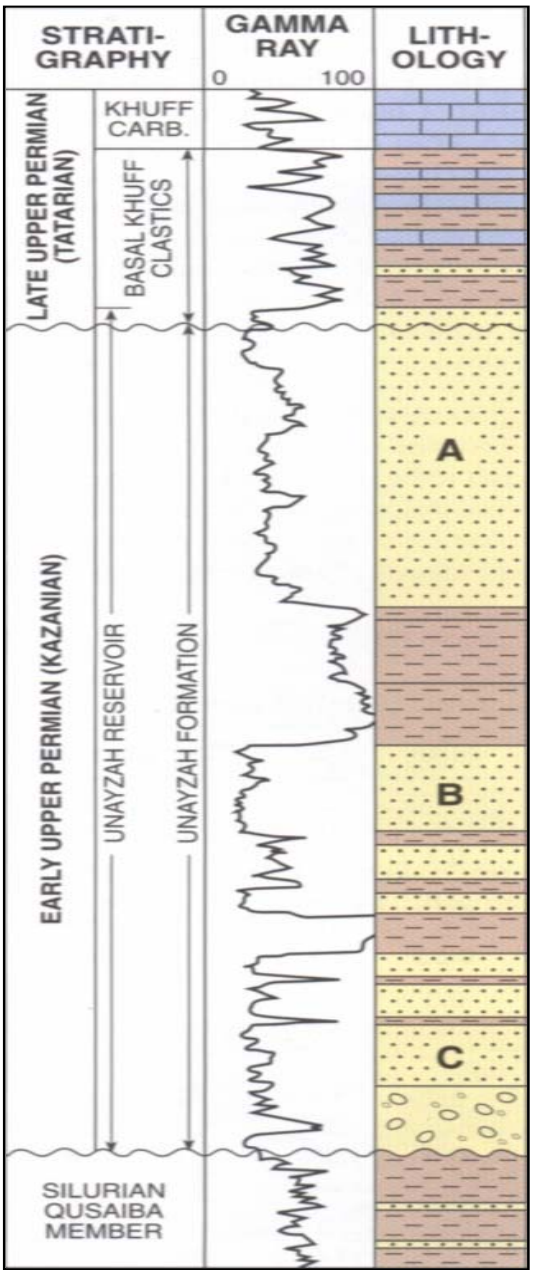

Fig. 12-Stratigraphic column of the Unayzah Formation[37].

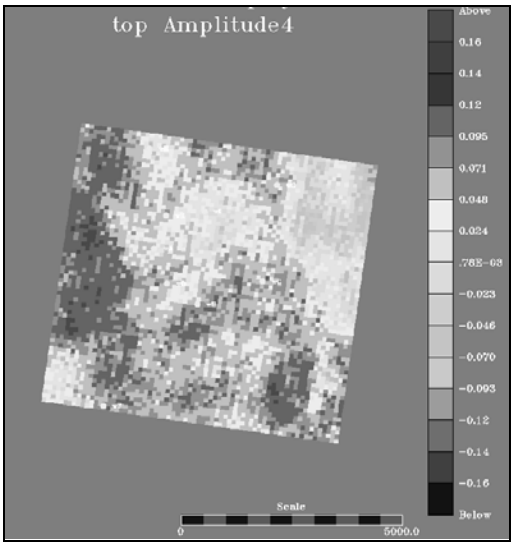

Fig. 13-Maximum acoustic seismic amplitude-top of the reservoir 100mx100 m.

Well	X(m)	Y(m)	Top (ft)	Base (ft)
A	731875	2551249	8886	8932
B	732861	2549953	8900	8950
C	734375	2550472	8908	9015
D	732170	2550424	8878	8931
E	732144	2551997	8912	8950
F	730700	2547600	8962	9164
G	734700	2552669	8992	9158
H	731765	2553556	8955	9014
I	733025	2552100	8940	8954

Table 1-General well information.

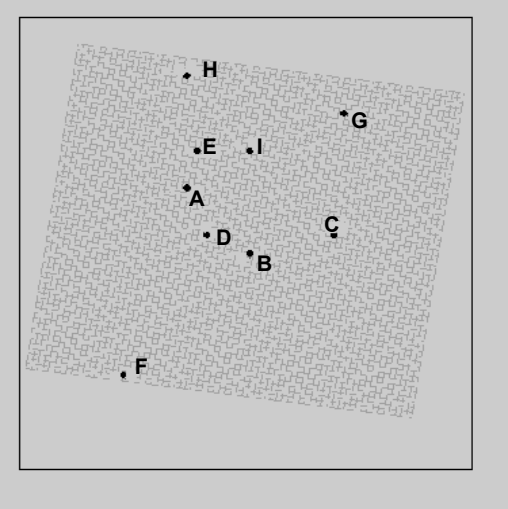

Fig. 14-Well positions in the study zone.

Well	NPHI_Top
A	0.15371
B	0.16215
C	0.13942
D	0.16366
E	0.14880
F	0.11647
G	0.09678
H	0.13634
I	0.15107

Table 2-Average values of neutron porosity for each well.

Well	Top_100x100
A	0.0300
B	0.0500
C	0.0800
D	0.0700
E	0.0500
F	0.0900
G	0.0600
H	0.0200
I	0.0100

Table 3- Maximum acoustic seismic amplitude for each well at the top of formation.

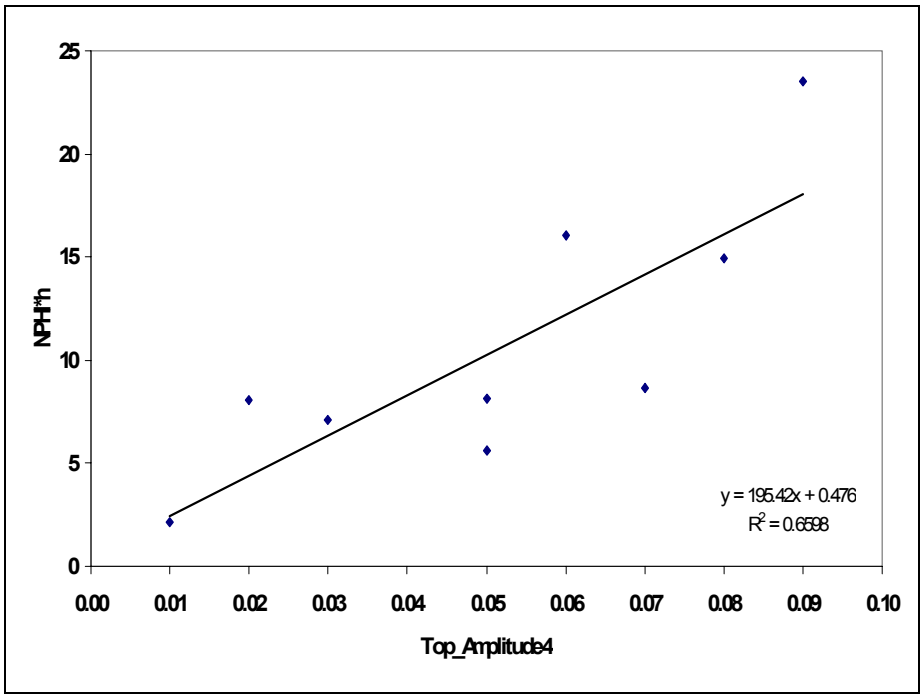

Fig. 15-Correlation between neutron porosity*thickness and 100m*100m seismic amplitude parameter.

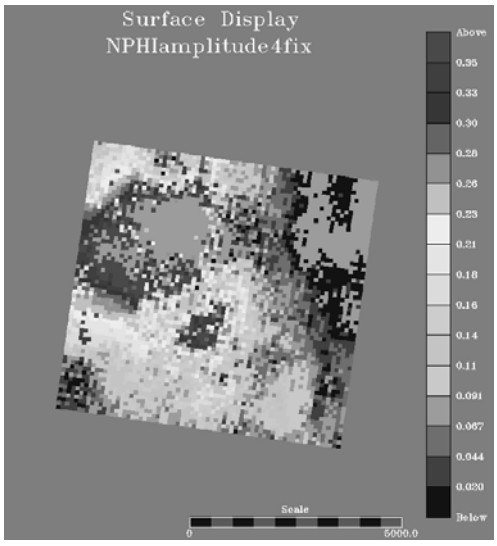

Fig. 16-Porosity distribution from maximum acoustic seismic amplitude, 100mx100m.

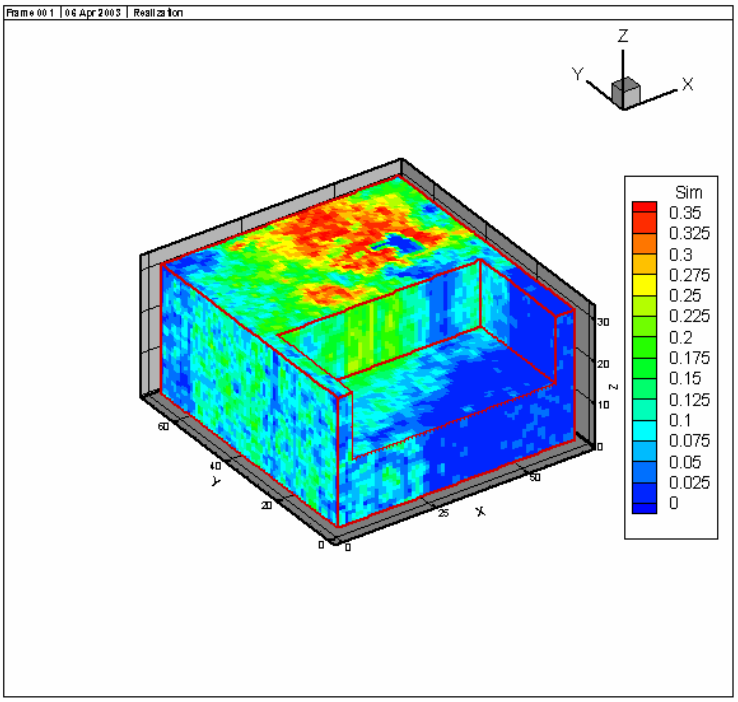

Fig. 17-3D high-resolution model for porosity distribution using σ_2 =0.0001, θ =0.5858, and betas=1.

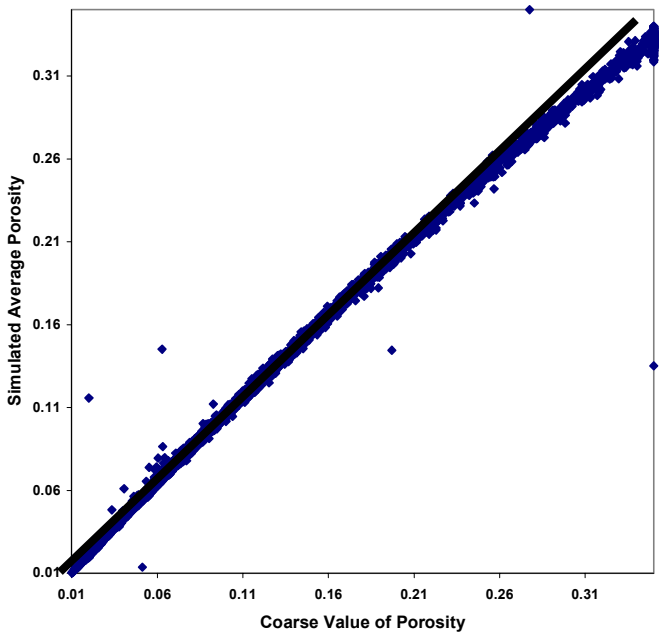

Fig. 18- Crossplot of simulated average porosity values vs coarse scale porosity values, σ_2 =0.0001 , θ =0.5858, and betas=1.

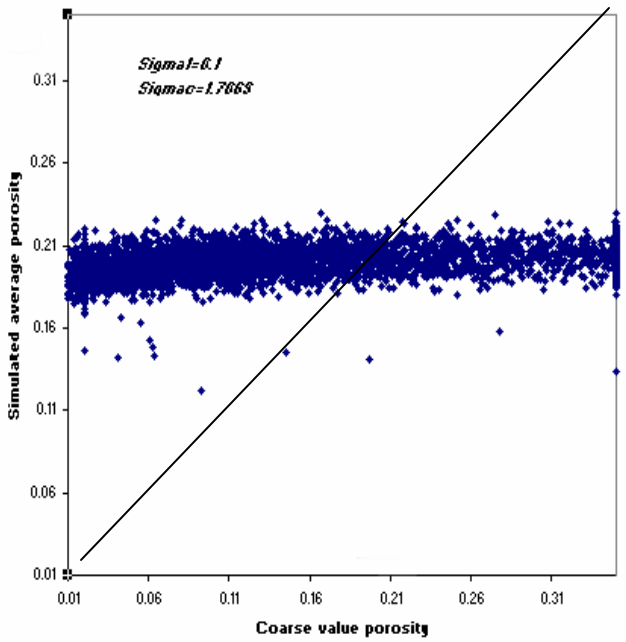

Fig. 19-Crossplot of simulated average porosity values vs coarse scale porosity values, σ_2 =0.1 , θ =0.5858, and betas=1.

RESULTS AND DISCUSSION: PART IIIA

Field-Scale Design Optimization via Numerical Simulation: Use of Downhole Samplers for Test Design

Introduction

The past several years have seen a great increase in the development, deployment and application of permanent in-well fiber optic monitoring systems. In-well fiber optic sensors are either currently available or under active development for measuring pressure, temperature, flow rate, phase fraction, strain, acoustics, and sand production. Potential future sensor developments include measurement of density and fluid chemistry (Kragas et al., 2001). This study is a preliminary investigation of the use of downhole sensors to enhance the value of Partitioning Interwell Tracer Tests (PITTs). The idea being investigated is to measure the tracer concentrations in real time at multiple depths using downhole sensors. These tracer concentration data could be used to estimate oil saturations at the corresponding depths using the method of moments (Zemel, 1995) and/or inverse modeling (Yoon et al., 1999, Wu et al., 2002).

Preliminary Results

Partitioning interwell tracer tests were simulated for two cases. In each case, a tracer slug was injected and the produced tracer concentrations were measured for several layers corresponding to several depths in these production wells. Residual oil saturations were estimated and a vertical distribution of oil saturation was generated.

The first case illustrated is based upon a carbonate outcrop called Lawyer Canyon in the San Andres formation. The outcrop geology is quite similar to the oilfields of West Texas and consists of highly cyclic Permian dolomitized shallow water platform carbonates (Jennings et al., 2000). Figure 1 shows the location of the outcrop and the associated geology. A vertical cross-section of 150 feet long by 100 feet wide by 10 feet thick was simulated. The geometrically averaged horizontal permeability is 13 md and the porosity is 0.15. Residual oil saturation distributions were generated using an exponential relation with the permeability. The average residual oil saturation is 0.35. Figures 2 and 3 show the permeability and residual oil saturation profiles. The residual oil saturation was averaged for each simulation layer and is shown versus depth in figure 6.A tracer slug consisting of a conservative tracer and two partitioning tracers of partitioning coefficients 0.5 and 1.0 was injected. The injected volume of the tracer slug was 0.7 PV. Figures 4 and 5 show the tracer concentration curves for the top and bottom simulation layers The.bottom low permeability layers have greater tracer transit times, evident from figure 5. The method of moments (Zemel, 1995) was used to calculate the residual oil saturation for each layer from the simulated tracer concentrations. The major assumptions of the method are that the average oil saturation in the reservoir is constant with time and the partition coefficients of the tracers do not change during the test.

The average oil saturation in the swept volume can be calculated from PITT data using the following equations. The partition coefficient for tracer i between the oil phase and the mobile water phase is

$$K_i = \frac{C_{2i}}{C_{1i}}$$

where C2i is the concentration of tracer i in the oil phase and C1i is the concentration of tracer i in the water phase. The mean residence volume for a tracer i in a slug tracer injection is

$$\overline{V}_i = \frac{\int_0^\infty V C_{Di} dV}{\int_0^\infty C_{Di} dV} - \frac{V_{slug}}{2}$$

In the above equation V_{slug} is the volume of the injected tracer slug, C_{Di} is the normalized concentration of tracer i at the producer and V is the cumulative volume of fluid injected.
The oil saturation can be calculated by

$$S_o = \frac{\overline{V}_2 - \overline{V}_1}{(K-1)\overline{V}_1 + \overline{V}_2}$$

$\overline{V}_2$ is the mean residence volume of the partitioning tracer, $\overline{V}_1$ is the mean residence volume of the conservative tracer and K is the partition coefficient of the partitioning tracer.

Figure 6 shows the close match between the estimated and model oil saturations, for simulation runs with different vertical permeability values. The accuracy in estimation increases with decrease in vertical permeability due to decreased cross flow.

The second illustration is for a three-dimensional oil reservoir. The simulated field is a quarter of a 40 acre five-spot well pattern. For the permeability realization, the standard deviation in the natural logarithm of permeability was 1.61, the geometrically averaged permeability was 345 md, the correlation length in the vertical z-direction was 10 ft, and the correlation lengths in the horizontal directions were 100 ft. An exponential variogram was used to generate the permeability data. The permeability and oil saturation distributions have been presented in Figures 7 and 8. The injected volume of the tracer slug was 0.9 PV. Figure 9 shows the tracer concentration outputs for the first simulation layer. Figure 10 shows the close match between the estimated and model oil saturations. The same trend, as in the two-dimensional case of higher accuracies with decreasing vertical permeability is observed.

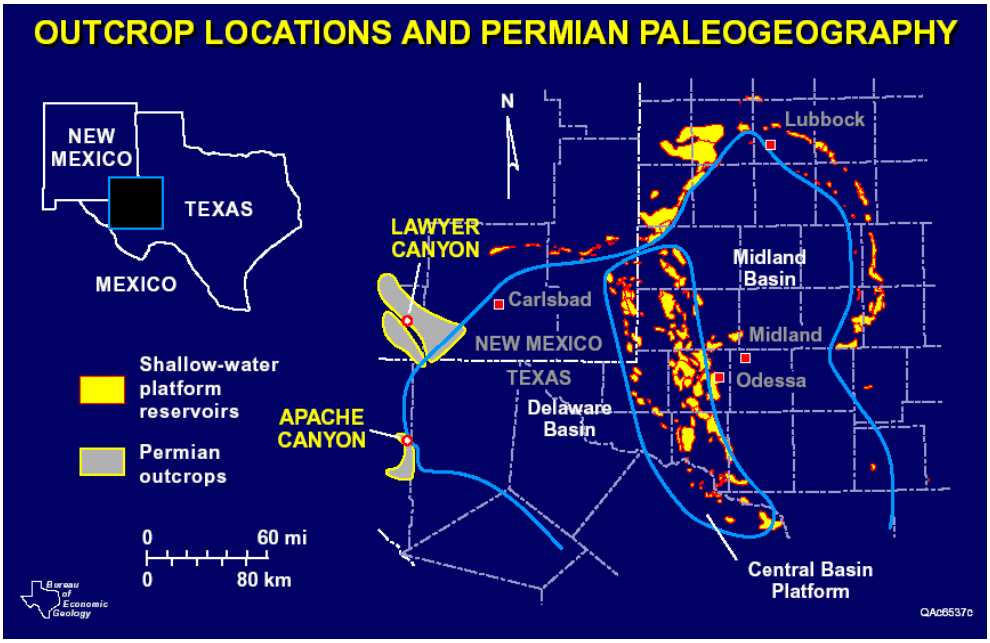

Figure 1**:** Map of geology and carbonate outcrop location of West Texas

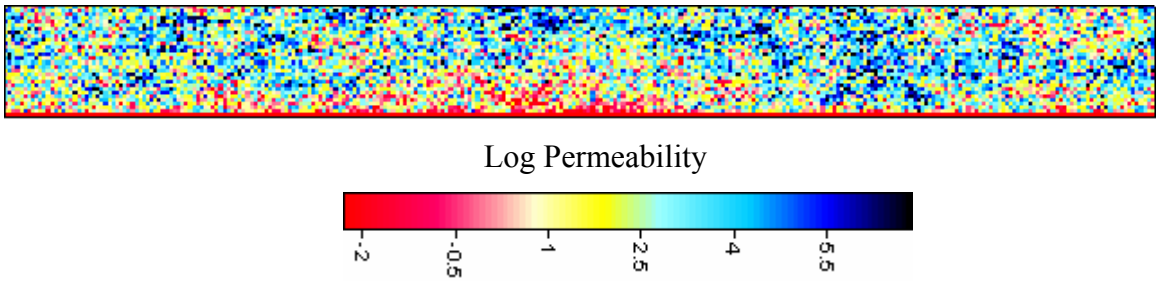

Figure 2: Horizontal permeability profile of Lawyer Canyon

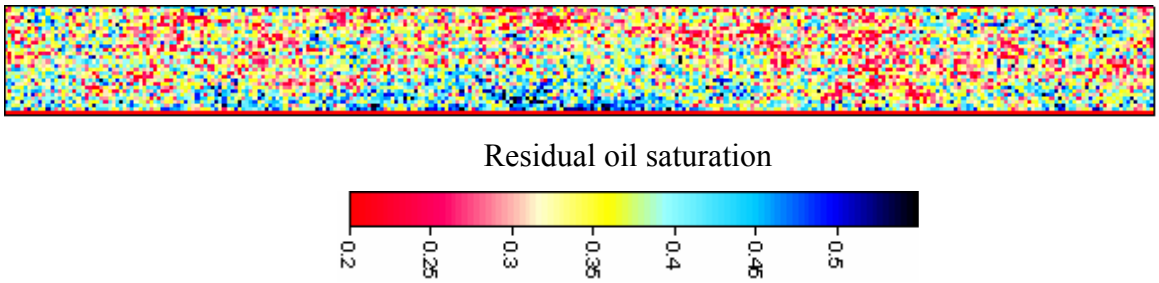

Figure 3: Residual oil saturation profile of Lawyer Canyon

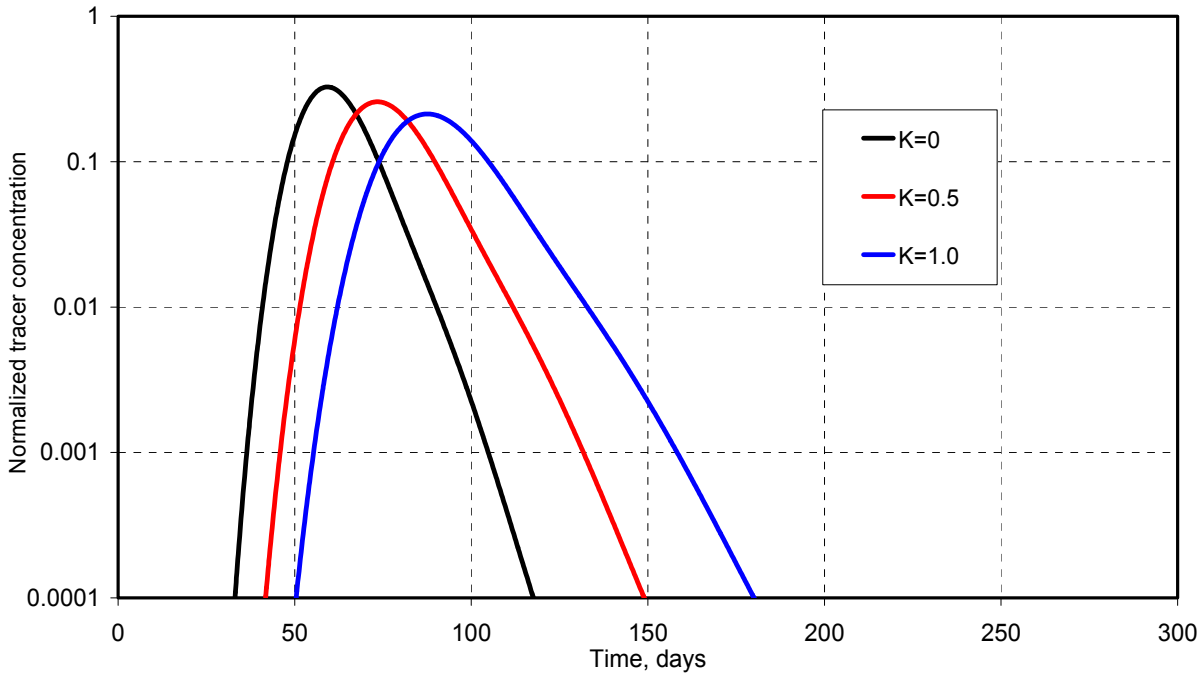

Figure 4: Normalized tracer concentrations for simulation layer 1 for Lawyer Canyon

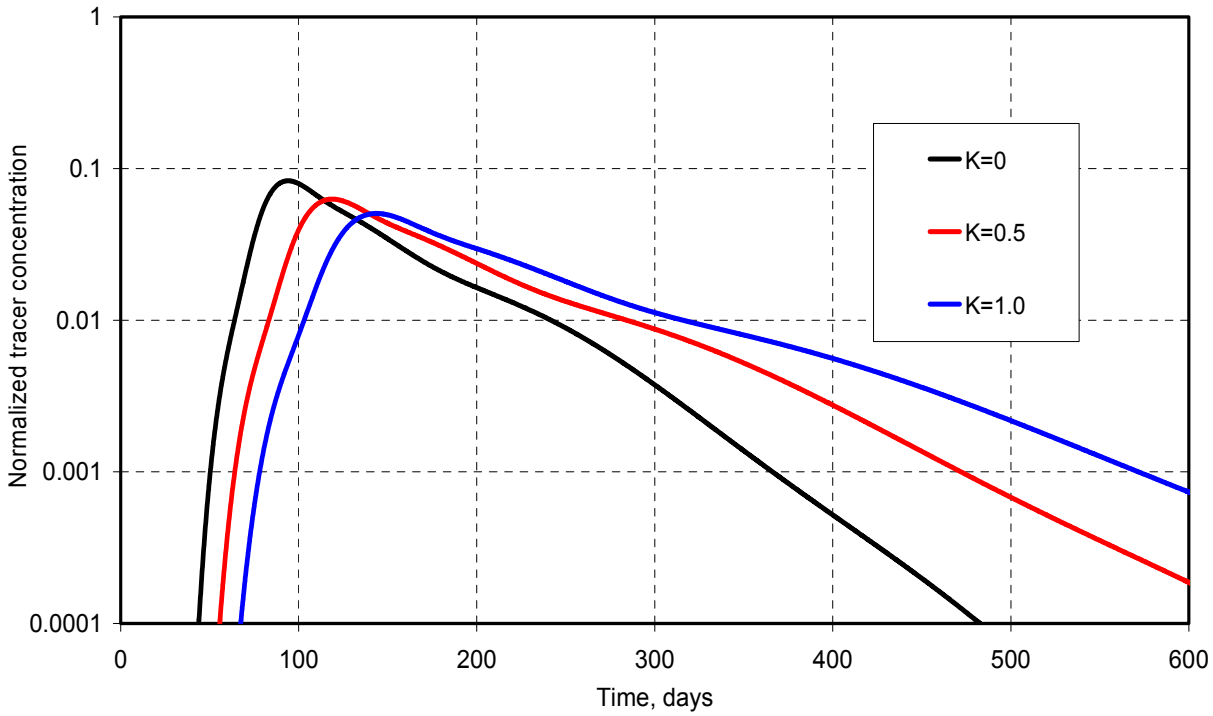

Figure 5: Normalized tracer concentrations for simulation layer 30 for Lawyer Canyon

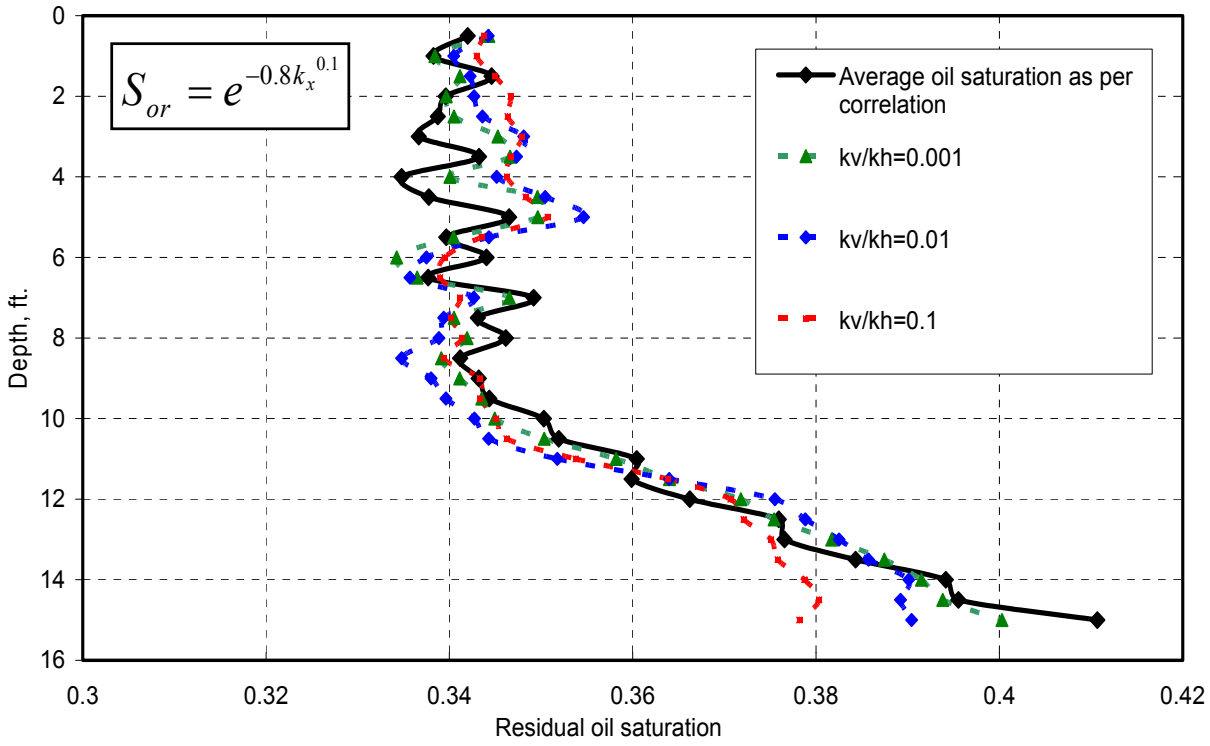

Figure 6: Estimated oil saturations for different vertical permeabilities for Lawyer Canyon

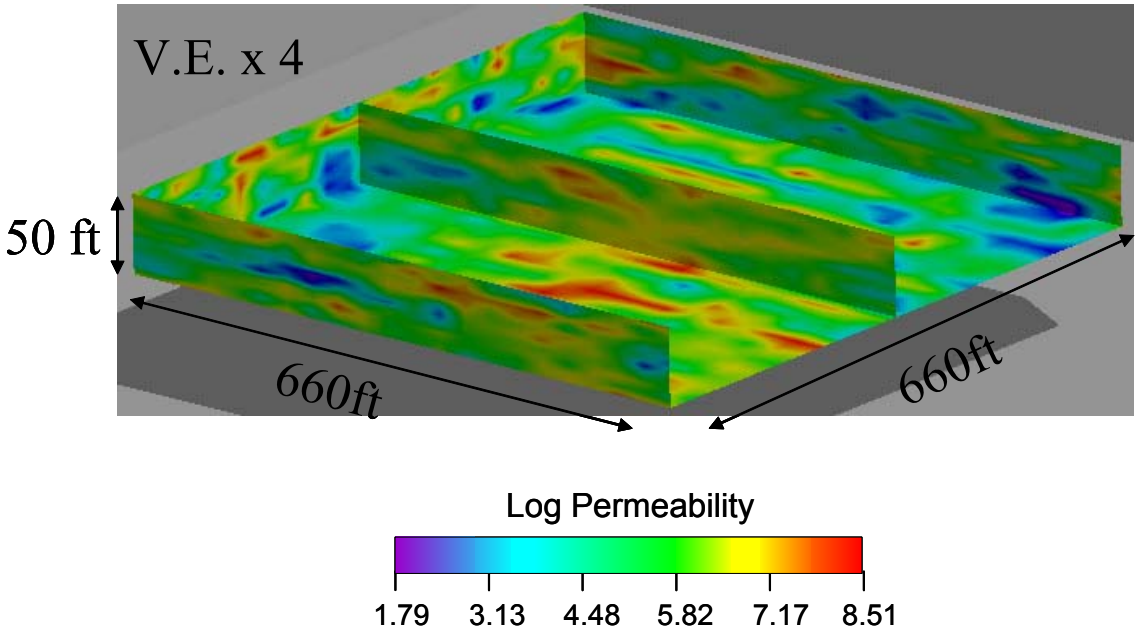

Figure 7: Permeability profile of the three-dimensional reservoir

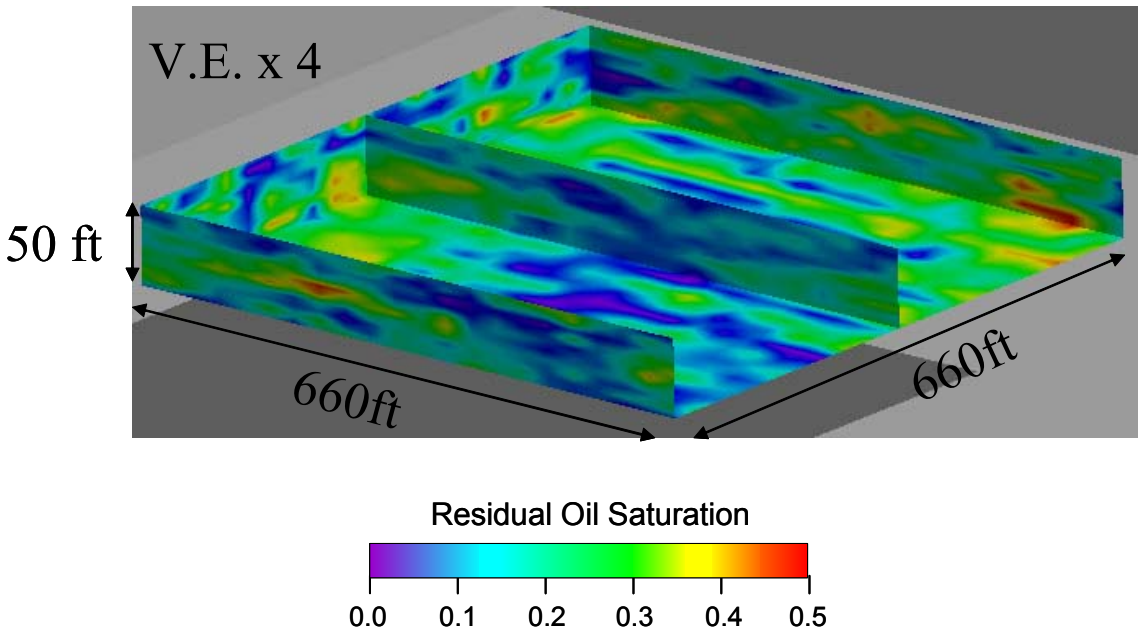

Figure 8: Residual oil saturation profile of the three-dimensional reservoir

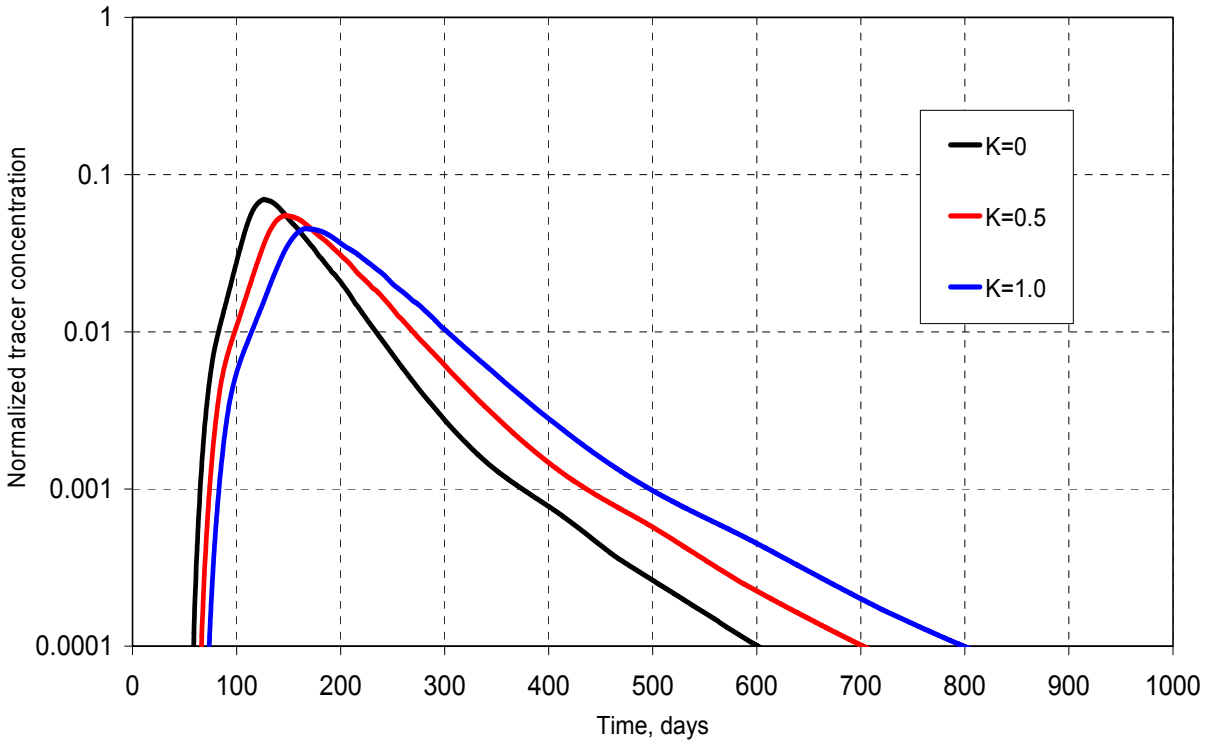

Figure 9: Normalized tracer concentrations at the producer for simulation layer 1 of the three-dimensional reservoir

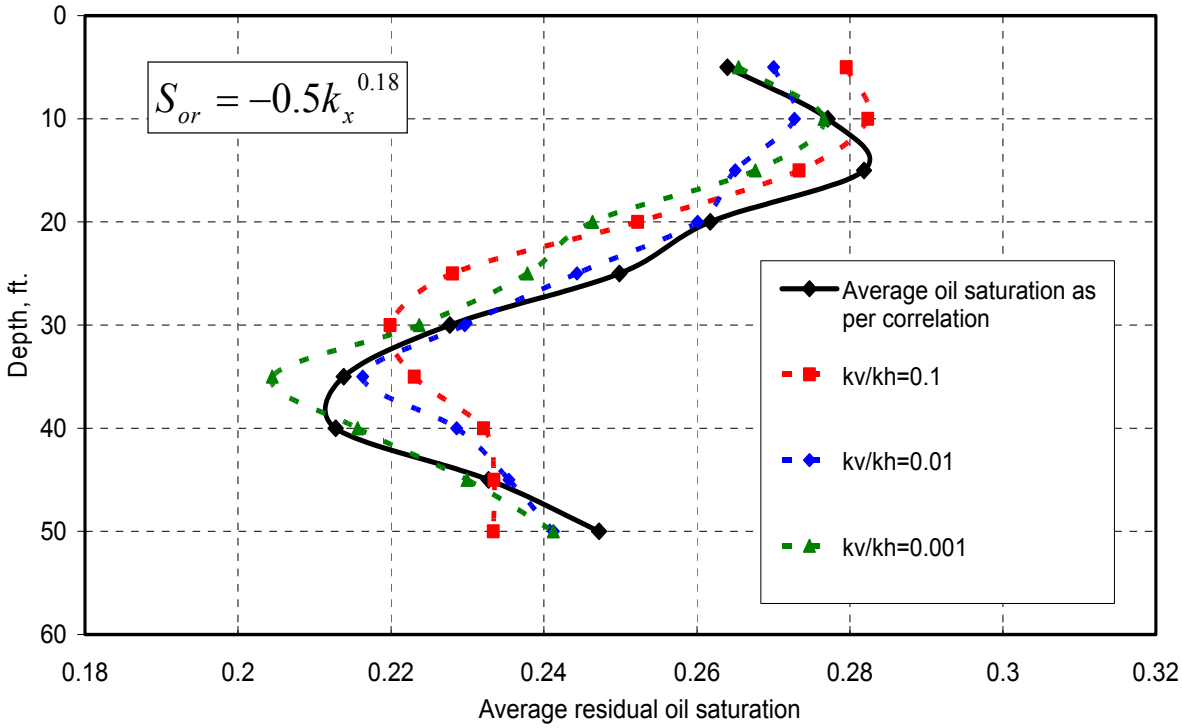

Figure 10: Estimated oil saturation for different vertical permeabilities for the 3 dimensional reservoir

RESULTS AND DISCUSSION: PART IIIB

Field-Scale Design Optimization via Numerical Simulation: Use of Natural Tracers for PITT Design

Introduction

Crude oil is a mixture of organic components of varying water solubility. A novel idea being investigated in this research is to use some of the more water-soluble components of crude oil as natural partitioning tracers to estimate oil saturations and swept pore volumes, and hence as a substitute for injected tracers. The rate at which these components will dissolve into water will depend upon their partition coefficients under reservoir conditions. In this study we have identified some of the common components of crude oils that might be used as natural partitioning tracers. Equations have been derived to estimate pore volumes and average oil saturations in a reservoir for both single-phase and multiphase flow and two simulations used to illustrate their validity under the assumed conditions.

Preliminary Results

Water-soluble components of crude oil have been studied for various geochemical applications (Bennet et al., 1997; Larter et al., 1995; Taylor et al., 1997; Kharaka et al., 2000). Some of the most soluble components are phenols, benzoic acids, quinolines and aliphatic acids. Table 1 lists some representative partition coefficients (Bennet et al., 1997, Reinsel et al., 1994 and Taylor et al., 1997) with a wide range of values from 0.009 to 31.

The mass conservation equations can be integrated under remarkably general reservoir conditions to estimate oil saturations and pore volumes. The major assumptions are that the partition coefficients are constant and the volume of each component dissolved into the water is small compared to total oil volume, so that its dissolution has negligible effect on the saturations. In general, the equations can be applied to heterogeneous reservoirs with multiphase flow.

The first case illustrated is based upon a carbonate outcrop called Lawyer Canyon, reference of which has been made in the first part of the report. The field was simulated with single phase flow and a uniform residual oil saturation of 0.30. The residual oil was modeled as a mixture of four partitioning components. Table 2 outlines the components and their initial concentrations. A waterflood was simulated and component concentrations were measured at the producer. Figure 1 shows the concentration of the crude oil components at the producer. The concentration of these compounds decrease with time as they are stripped out of the oil phase in the reservoir. Concentration of any two compounds can be used for the estimation of pore volumes and average oil saturations. In the cases illustrated, butyric acid and phenol concentrations have been used for the estimation. Figures 2 and 3 show the comparison between the estimated and reservoir oil saturations and pore volumes.

The second illustration is a waterflood of a quarter of a 40 acre five spot well pattern. The standard deviation in the natural logarithm of permeability was 1.61, the geometrically averaged permeability was 277 md, the correlation length in the vertical direction was 10 ft, and the correlation lengths in the horizontal directions were 100 ft. An exponential variogram was used to generate the permeability data. Figure 4 shows the permeability profile for the simulation field. The field was simulated with a uniform initial oil saturation of 0.7. The oil was modeled as four partitioning components as in the previous illustration. Figure 5 shows the fluid production rates of the simulated water flood. Figure 6 shows the concentrations of the crude oil compounds

at the producer in the water phase. Figures 7 and 8 show the close match between the estimated and actual oil saturations and pore volumes.

Compound	**Partition Coefficient**
Acetic Acid	0.009
Butyric Acid	0.084
Phenol	1.3
p-Cresol	3.6
o-Cresol	5.2
2,4 Dimethyl Phenol	15
3 Isopropyl Phenol	31

Table 1: Partition Coefficients of crude oil compounds

Compound	**Partition Coefficient**	**Initial concentration in the oil phase, mg/l**
o-Cresol	5.2	7.5
Phenol	1.3	1.5
Butyric Acid	0.084	1
Acetic Acid	0.009	1

Table 2: Oil compounds modeled in the illustrated simulations

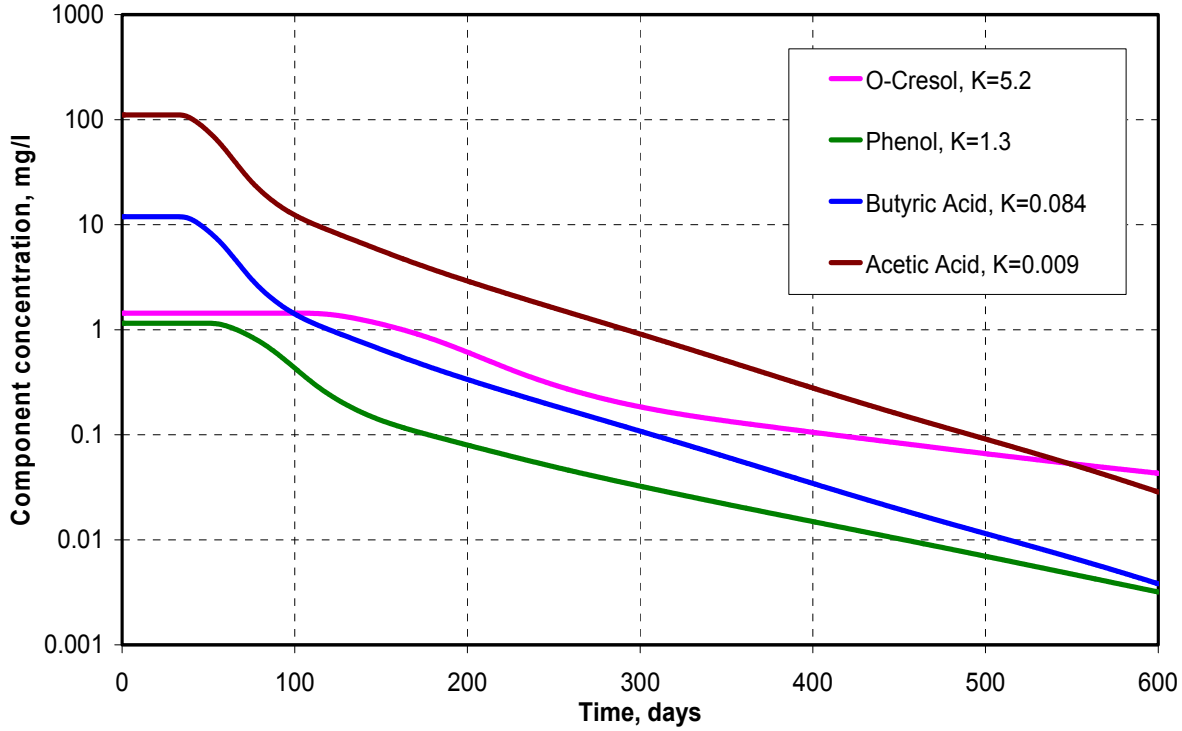

Figure 1: Total component concentrations at the producer for Lawyer Canyon

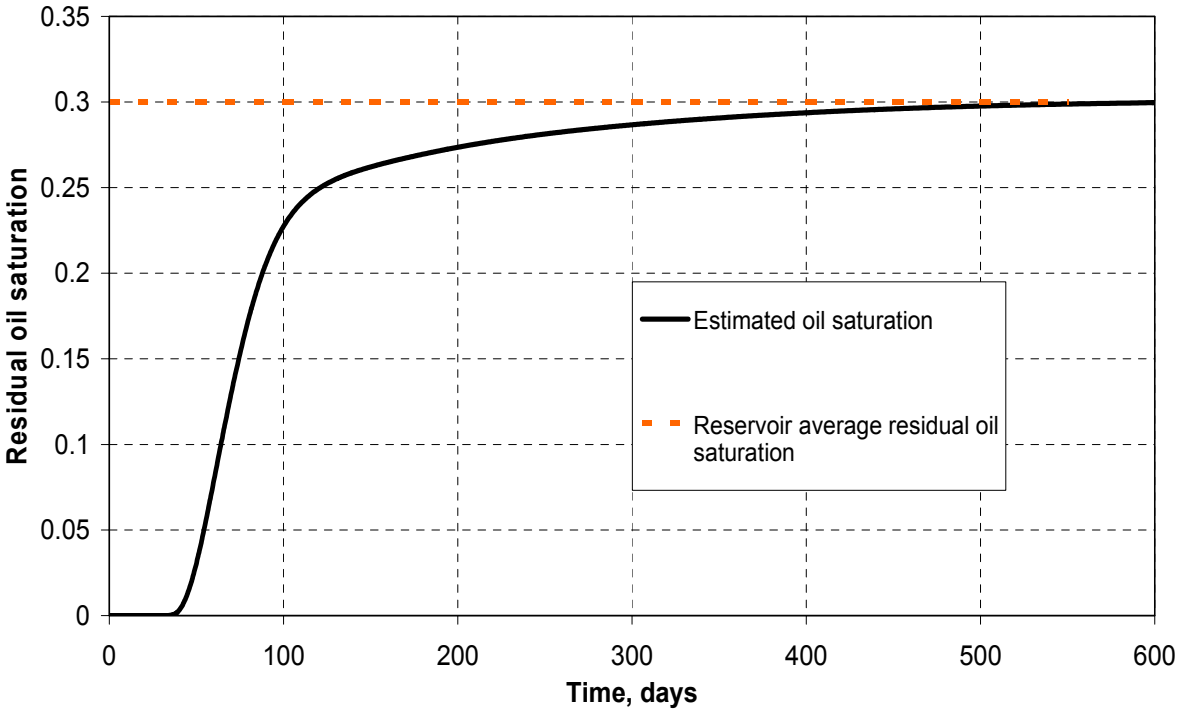

Figure 2: Estimated residual oil saturation for Lawyer Canyon using concentrations of Phenol and Butyric Acid

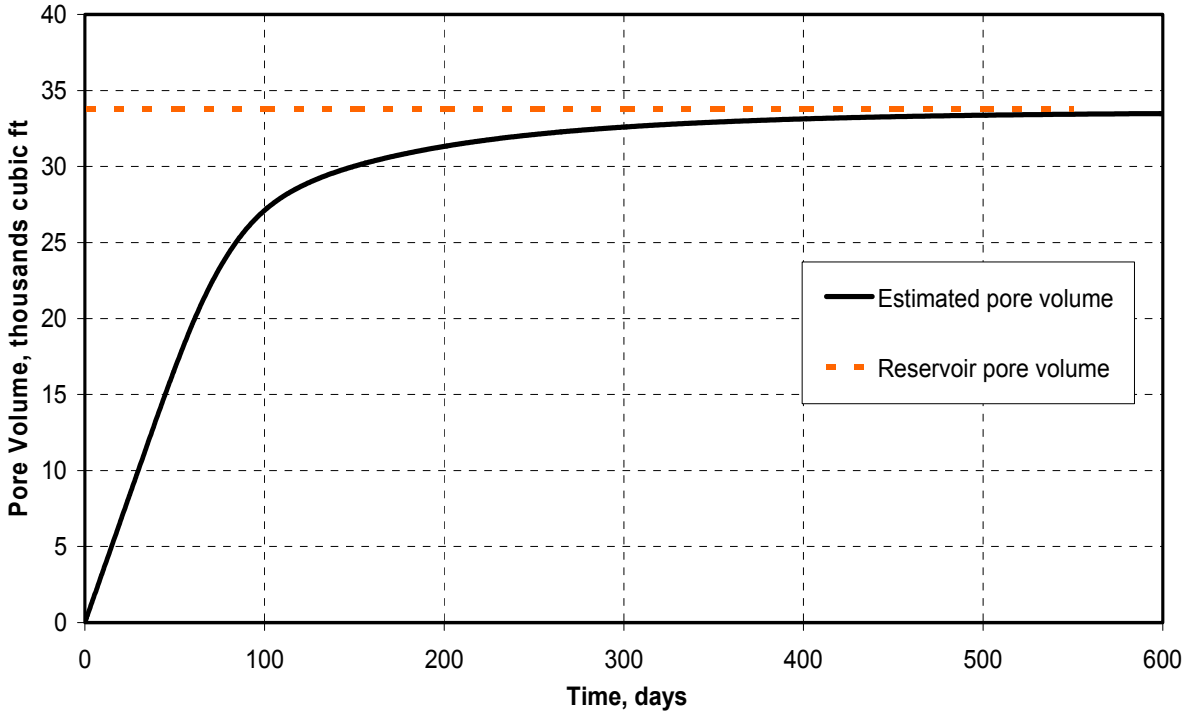

Figure 3: Estimated pore volume for Lawyer Canyon using concentrations of Phenol and Butyric Acid

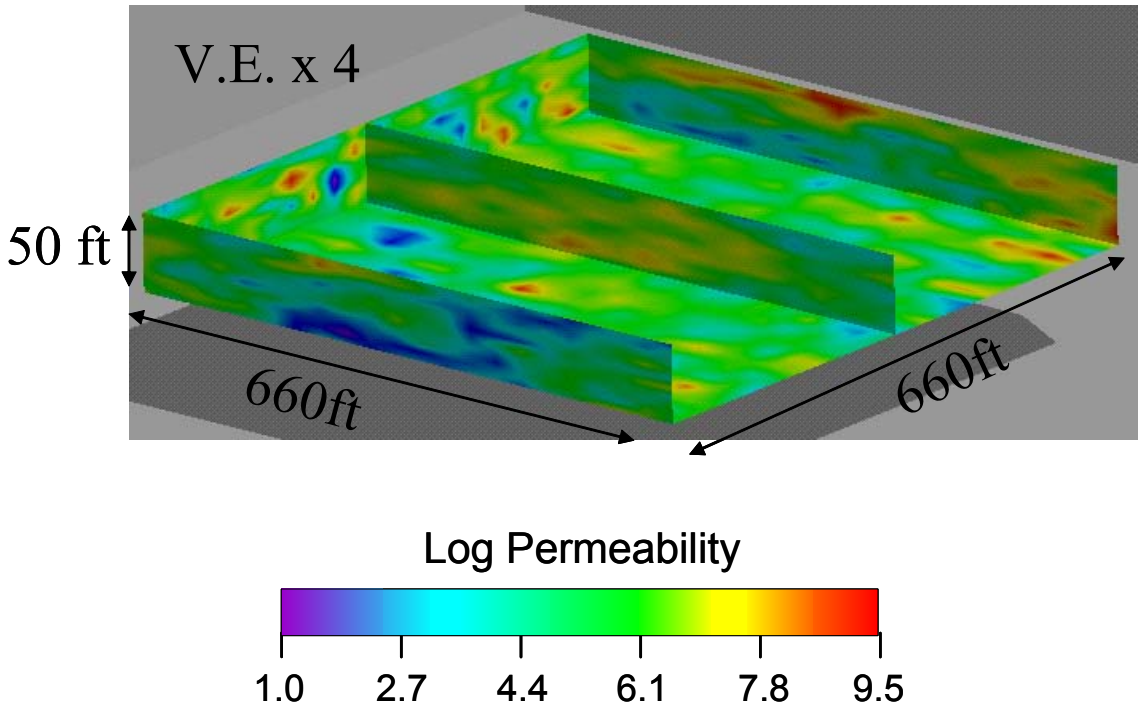

Figure 4: Permeability Profile for the 3 dimensional simulation

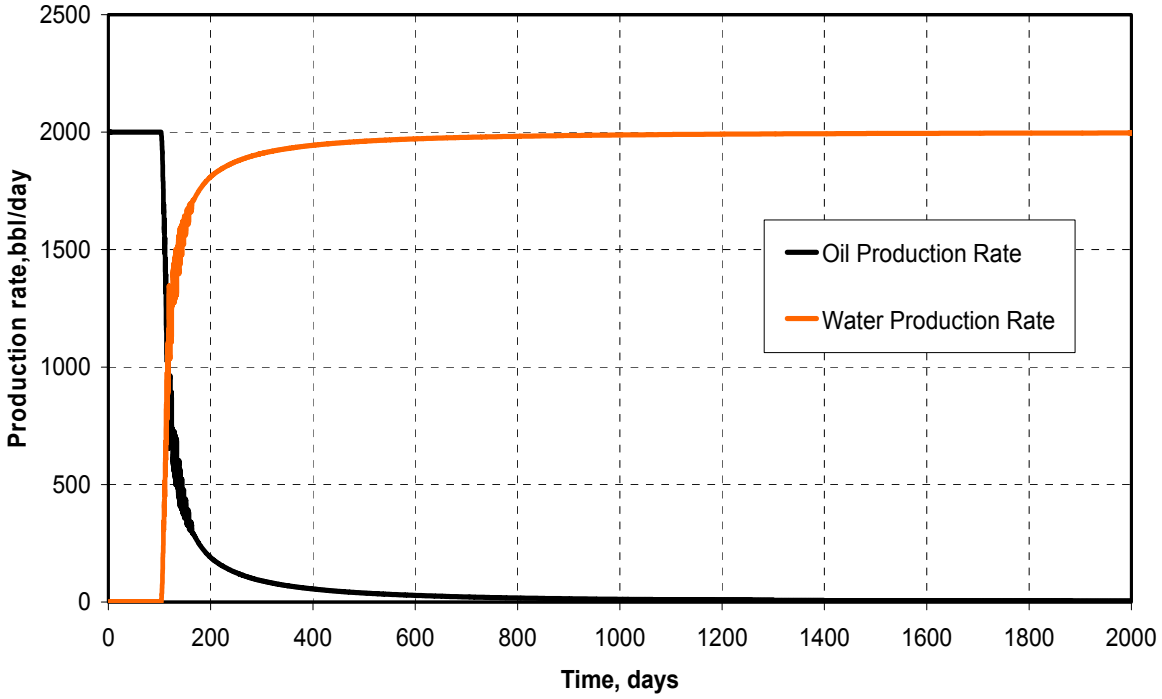

Figure 5: Fluid production rates for the 3 dimensional simulation

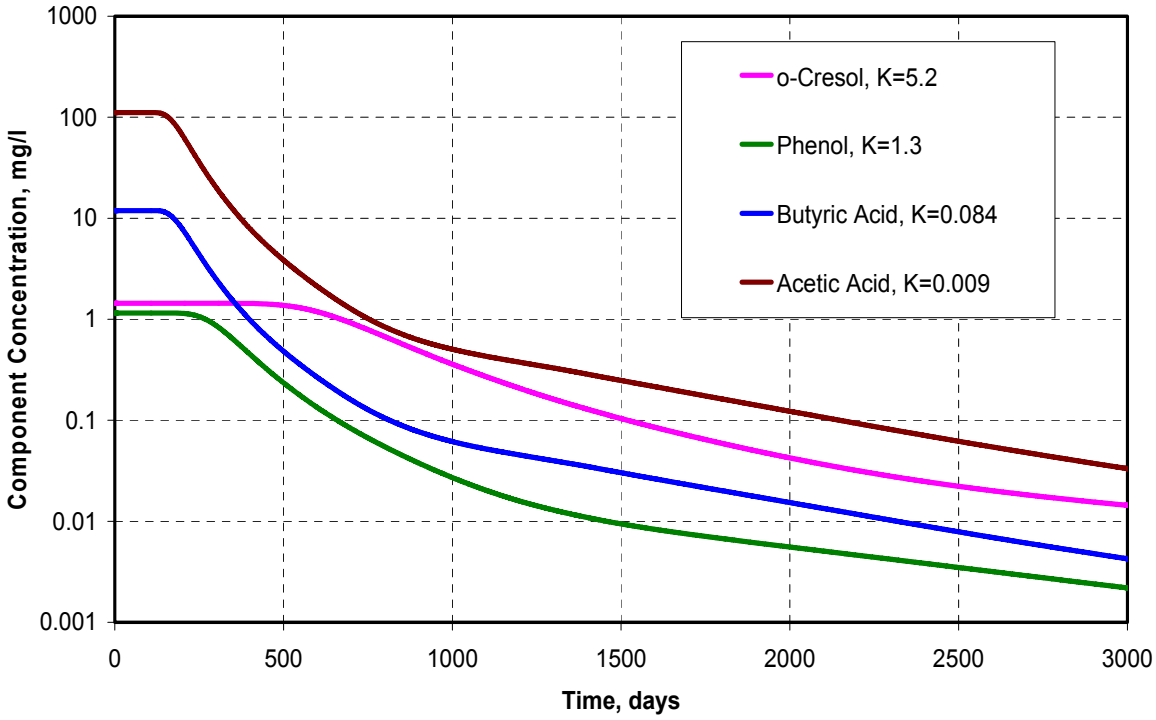

Figure 6: Component concentrations in the water phase at the producer for the 3 dimensional simulation

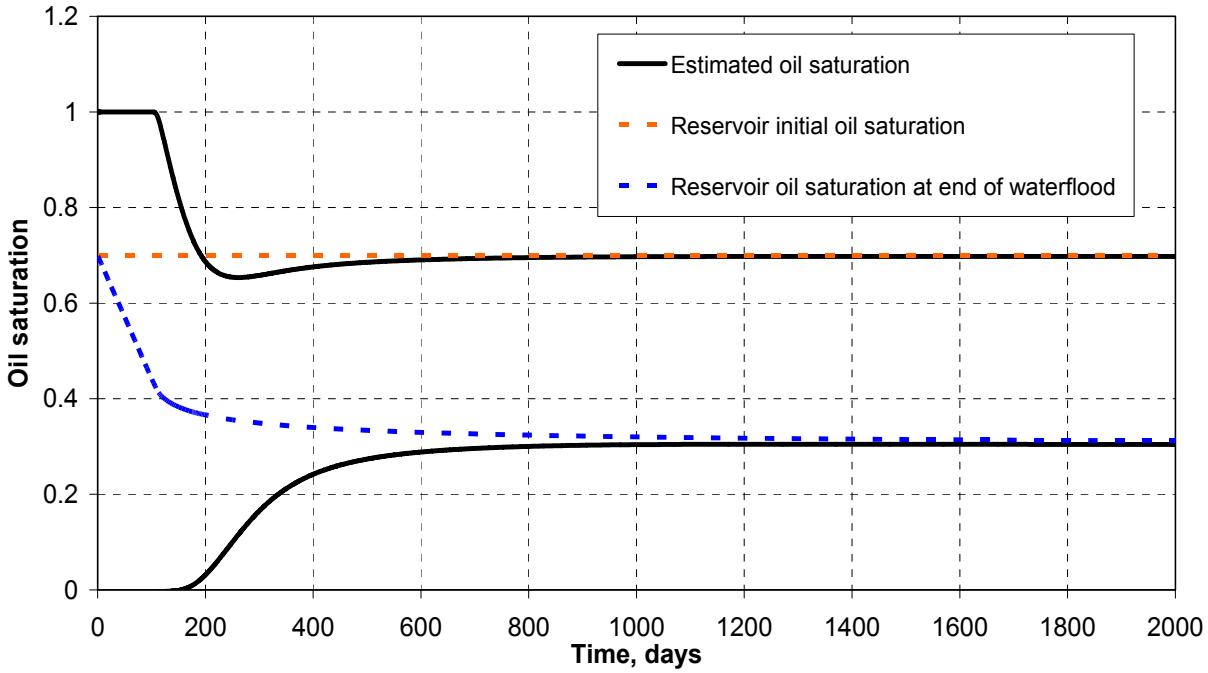

Figure 7: Estimated oil saturations using concentrations of Phenol and Butyric Acid for the 3 dimensional simulation

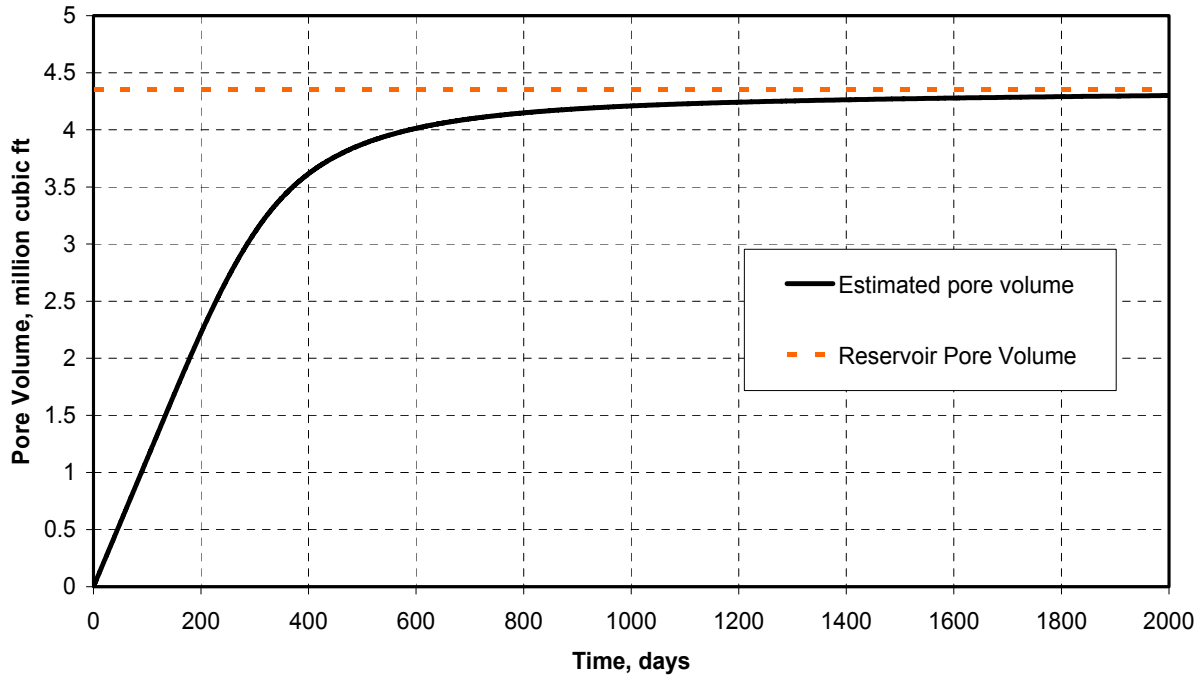

Figure 8: Estimated pore volume using concentration of Phenol and Butyric Acid for the 3 dimensional simulation.

RESULTS AND DISCUSSION: PART IIIC

Numerical Modeling of Partitioning Tracer Tests in Fractured Reservoirs

Introduction

Naturally fractured reservoirs can be modeled as two interconnected media: the matrix which contains the bulk of the fluid, but has very less conductive capacity, and the fracture which generally has high permeability but very little storage capacity. The dual porosity model is one of the oldest and most common approaches for modeling naturally fractured oil reservoirs and is available in most reservoir simulators including UTCHEM and ECLIPSE. The simulation domain is divided into two superimposed porous media: one for the fracture system and another for the porous rock matrix. A mass balance for each of the media results in two continuity equations coupled by a transfer function. This study compares the ECLIPSE and UTCHEM results for a series of partitioning tracer simulations as a first step in our research on how to optimize the use of tracers in naturally fractured oil reservoirs.

Simulation Results

In UTCHEM, each simulation gridblock can be divided into smaller matrix blocks depending upon the fracture spacing. In Eclipse, the fracture spacing is the same as the grid spacing, so simulating a small fracture spacing will increase the number of gridblocks and hence will increase the computational time. Figure 1 compares the oil production rates of a quarter of a five-spot water flood simulation with a slug tracer injection in a homogeneous fractured reservoir. The field simulated was 1000 ft long by 1000 ft wide by 25 ft thick. The porous matrix had an initial uniform oil saturation of 0.75 and a porosity of 0.3. The fractures had an initial oil saturation of 0.99 and a porosity of 0.01. The permeability of the matrix and the fracture were 100md and 1 md respectively. The tracer slug consisted of two partitioning tracers of partition coefficients 1 and 5, and was injected for 0.018 PV.

Table 1 shows the CPU times for a series of simulations with different fracture spacings and no subgridding of matrix blocks. UTCHEM has the advantage for small fracture spacing because of its feature allowing the user to specify more than one matrix block for each gridblock.

Figure 2 shows the comparison between the produced tracer concentrations for both ECLIPSE and UTCHEM. One of the significant processes in oil production in a fractured reservoir is capillary imbibition of water into the matrix with the simultaneous expulsion of oil to the fracture. Tracers having a higher partition coefficient will have a higher concentration in the oil phase, hence produced mass of these tracers will be greater. This phenomenon is evident from Figure 2. 82 % of the tracer mass with a high partition coefficient is recovered while only 50% of the other tracer is recovered.

Each matrix block can be subgridded to simulate flow inside a matrix block. In UTCHEM, the matrix blocks are subgridded as nested blocks in the horizontal direction and as stacked grids in the vertical direction and the size of each subgrid can be specified by the user. In ECLIPSE, the matrix blocks can be subgridded as nested blocks in two dimensions or as concentric blocks in three dimensions with the thicknesses of the subgrid varying logarithmically away from the fracture wall. Figures 3 and 4 show the simulation grids in a dual porosity model for UTCHEM and ECLIPSE. Figure 5 compares the oil production rates between ECLIPSE and UTCHEM for a homogeneous fractured reservoir with subgridding. The matrix blocks have two subgrids in the

horizontal direction. Comparisons with 3 dimensional subgridding are not presented as ECLIPSE failed to finish the simulation displaying a lot of convergence errors.

ECLIPSE uses a first order finite-difference method to approximate the spatial derivatives in the partial differential equations whereas UTCHEM has a third-order TVD finite-difference method, which is a more accurate approximation with less numerical dispersion. Figure 6 compares UTCHEM and ECLIPSE tracer production concentrations. The field simulated was a single phase, single porosity reservoir with a slug tracer injection. The slug volume injected was 0.02 PV. The field was a quarter of a five spot flood, 165 ft long by 165 ft wide by 5 ft thick.

Fracture Spacing, ft	CPU Time, seconds	
	ECLIPSE	UTCHEM
100	3	233
50	18	233
25	341	233
10	23369	233

Table 1: Run time comparisons for dual porosity runs with different fracture spacing for UTCHEM and ECLIPSE

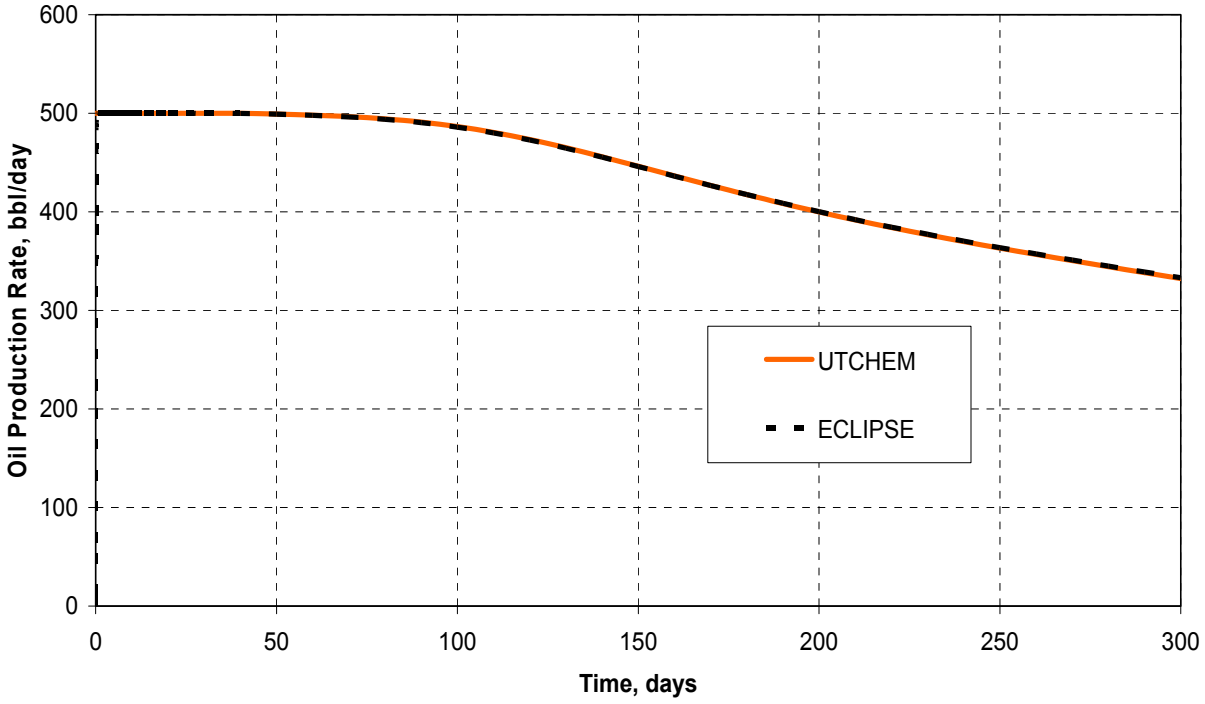

Figure 1: Comparison of oil production rate between UTCHEM and ECLIPSE for a fractured reservoir

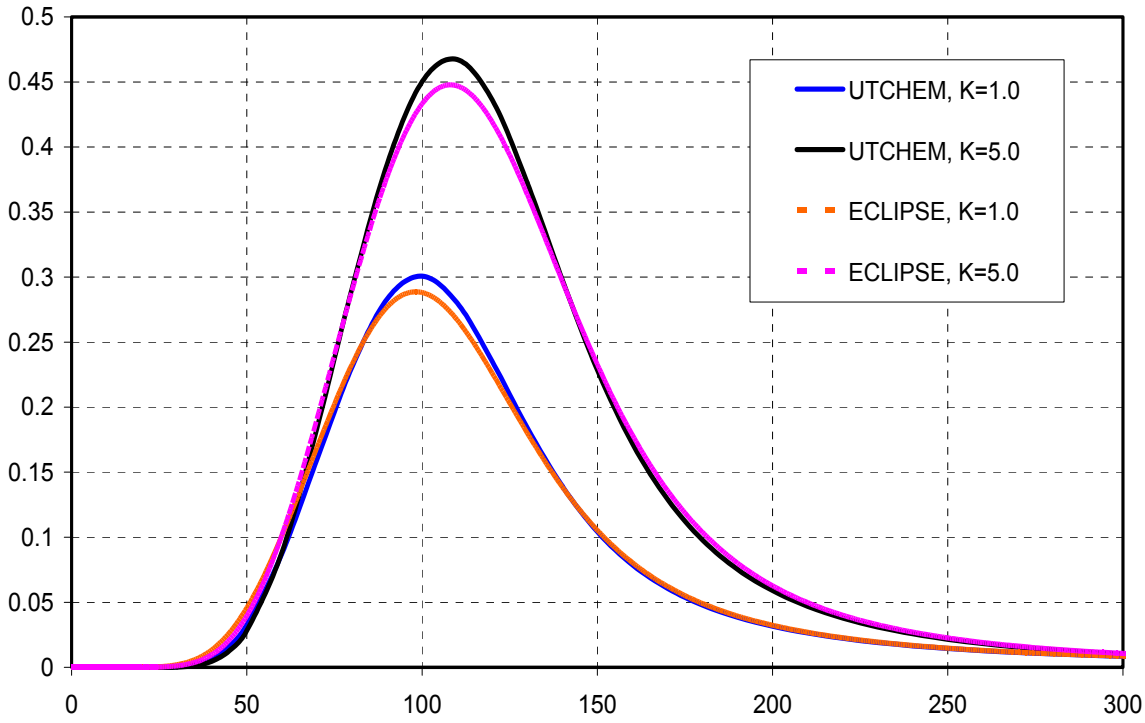

Figure 2: Comparison of total tracer concentrations between ECLIPSE and UTCHEM for a fractured reservoir

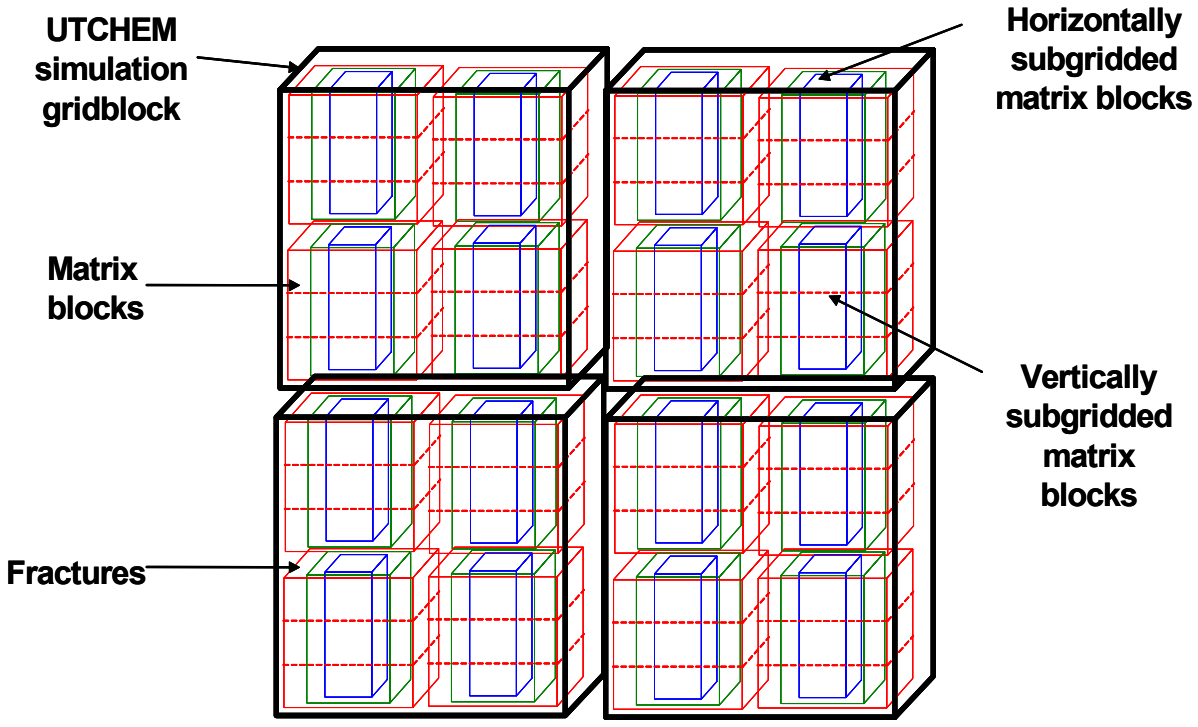

Figure 3: UTCHEM dual porosity simulation grid

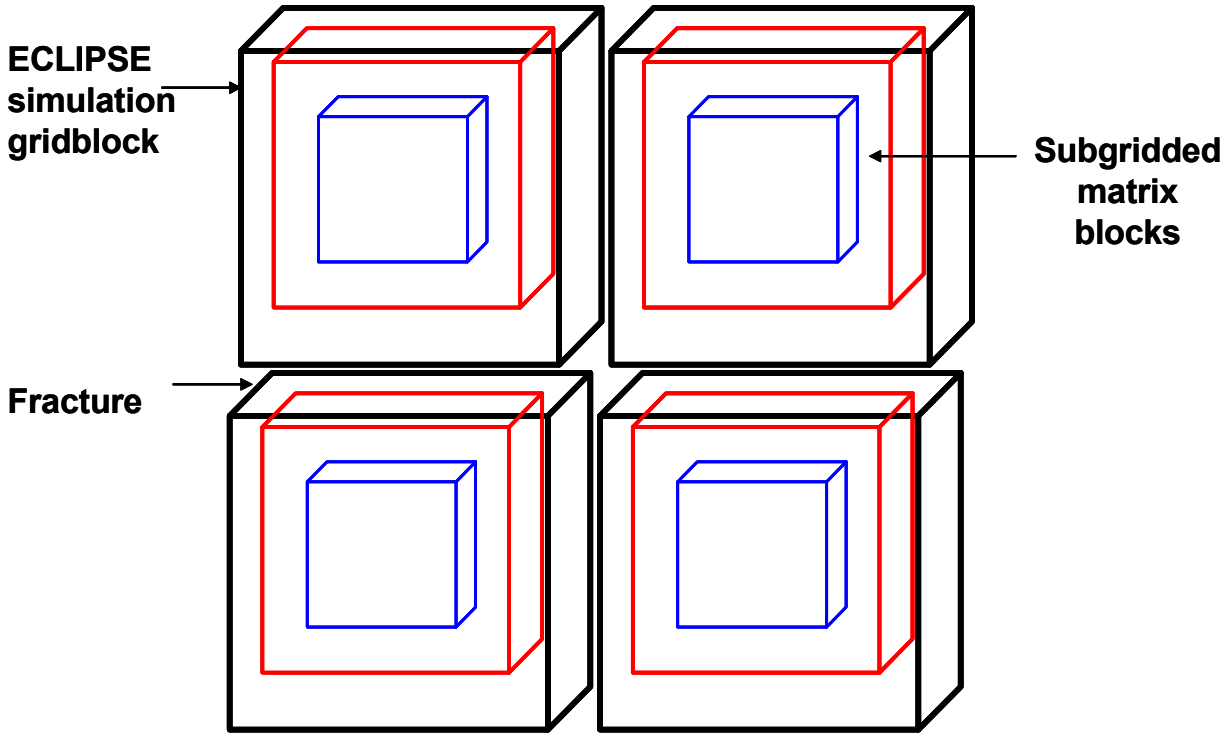

Figure 4: ECLIPSE dual porosity simulation grid

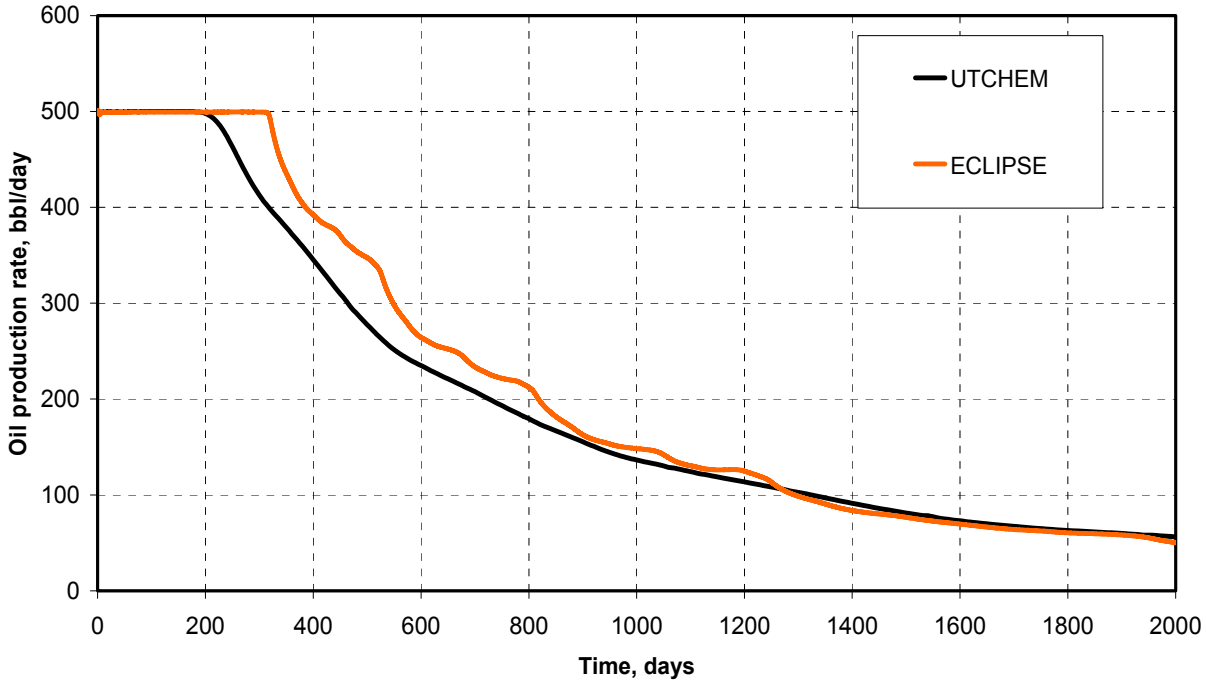

Figure 5: Comparison of oil production rates between ECLIPSE and UTCHEM for a dual porosity simulation with two subgrids in the horizontal direction

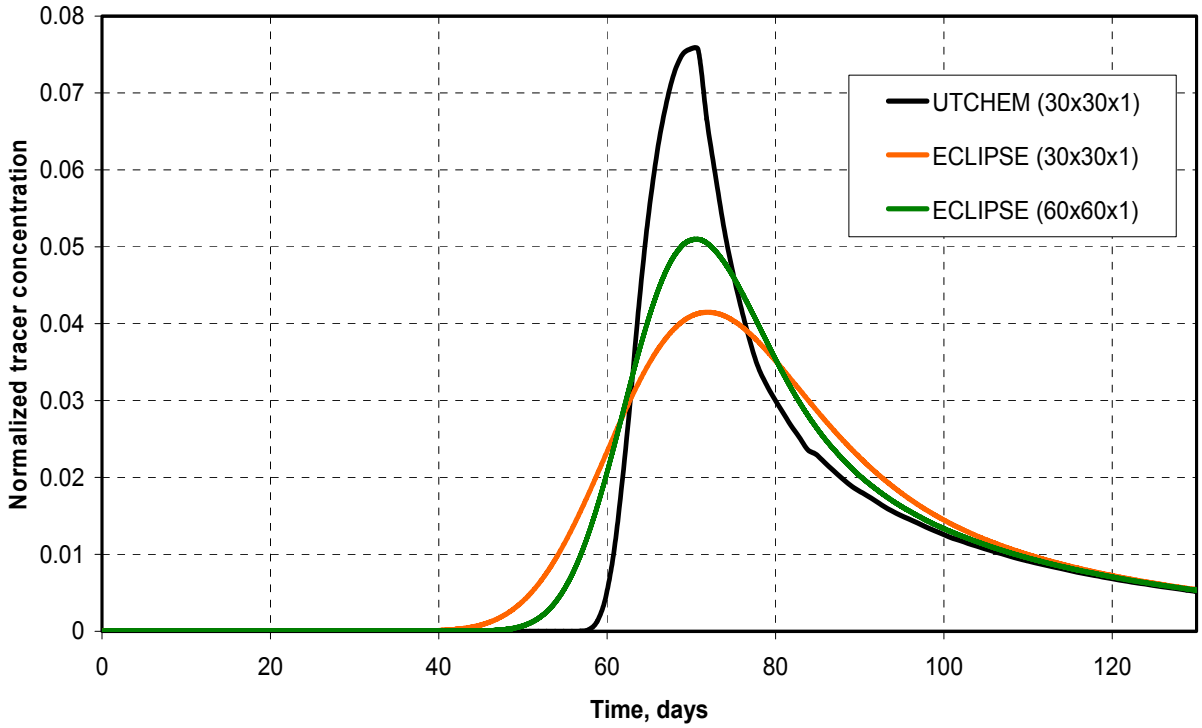

Figure 6: Comparison of tracer production concentrations between UTCHEM and ECLIPSE

CONCLUSIONS

Part-I

We have presented three approaches to production data integration and examined their relative merits using quantitative measures of non-linearity. These are travel time, generalized travel time and the commonly used amplitude inversion. The travel-time inversion of production data is robust and computationally efficient. Unlike conventional amplitude matching that can be highly nonlinear, the travel-time inversion has quasilinear properties. This makes the method particularly attractive for field-scale applications where the prior geologic model might be far from the solution. The generalized travel-time inversion appears to retain most of the desirable features of the travel-time inversion and also accomplishes the amplitude match. Some specific findings from this study can be summarized as follows:

1. We have quantitatively investigated the non-linearities associated with travel time and amplitude inversion for production data integration. The non-linearity is expressed in terms of a simple and intuitive geometric measure of curvature as proposed by Bates and Watts[16] and later used by Grimstad and Mannseth.[17]
2. The non-linearity in travel time inversion is found to be orders of magnitude smaller than the conventional amplitude inversion. As a result, the travel time inversion has better convergence properties and is less likely to be trapped in local minimum.
3. Travel time sensitivity is more uniform between the wells. In contrast, the amplitude sensitivity can be localized near the wells. The higher magnitude of the travel time sensitivity also contributes to its quasilinearity and improved convergence properties.
4. The generalized travel time inversion effectively combines travel time and amplitude inversion while retaining most of the desirable properties of the travel time inversion. For the field example studied here, the generalized travel time inversion outperformed both travel time and amplitude inversion.

Part-II

1. We have shown using a field application that Markov Random Fields provide an efficient and powerful framework for data integration accounting for the scale and precision of different data types. They are computationally tractable and are ideally suited to simulation-based computation such as MCMC (Markov Chain Monte Carlo) methods.
2. In the case study from Middle East presented here, we constructed fine scale porosity distribution from well and seismic data explicitly accounting for the varying scale and precision of the data types. This demonstrated the practical applicability of MRF for data integration.
3. The most sensitive parameter during spatial modeling using MRF was σ_2. This parameter quantifies the precision of the seismic data and controls the relationship between porosity and seismic data.

Part-III

1. An initial effort has been made in simulating the use of downhole sensors in tracer tests. Fields quite similar in characteristics to common oil fields were considered for the study. The initial results are very positive and show that partitioning tracers measured as a

function of depth with downhole sensors can in principle be used for estimating the vertical distribution of oil saturation during or after a waterflood. With permanent downhole sensors, the potential exists to make these measurements numerous times during a waterflood to update the sweep efficiency and consider targeting poorly swept oil using profile control, targeted infill drilling and other technologies and/or improved oil recovery methods.

2. The concept of natural tracers in oil fields has been introduced as a potentially cost-effective substitute for injected tracers. Phenols and aliphatic acids have been identified as some of the components of crude oil that might be used as natural partitioning tracers. Equations to calculate average oil saturations and pore volumes have been derived for single as well as multiphase flow and their accuracy has been illustrated with simulations.

3. Comparisons between UTCHEM and ECLIPSE for simulations without subgridding show good agreement. ECLIPSE failed to finish most of the simulations with subgridding. In addition ECLIPSE's first-order numerical method makes it quite difficult to simulate tracer problems accurately.

REFERENCES

Part-I

1. Bissel, R.C.: "Calculating Optimal Parameter for History Matching," *Proc*. 4th European Conference on the Mathematics of Oil Recovery, Topic E: History Match and Recovery Optimization, 1994.
2. Vasco, D.W., Yoon, S., and Datta-Gupta, A.: "Integrating Dynamic Data Into High-Resolution Reservoir Models Using Streamline-Based Analytic Sensitivity Coefficients," *SPE Journal* (December 1999) 389.
3. Oliver, D. S.: "Incorporation of Transient Pressure Data into Reservoir Characterization," *In Situ* 18 (3), 243-275 1994.
4. Datta-Gupta, A. *et al.*: "Streamlines, Ray Tracing and Production Tomography: Generalization to Compressible Flow," *Petroleum Geoscience* (May 2001), 75.
5. Yoon, S., Malallah, A.H., Datta-Gupta, A. and Vasco, D.W..: "A Multiscale Approach to Production Data Integration Using Streamline Models," *SPE Journal*, 6(2), 182-192, June (2001).
6. Landa, J.L., Kamal, M.M., Jenkins, C.D., and Horne, R.N.: Reservoir Characterization Constrained to Well Test Data: A Field Example," paper SPE 36511, Presented the 1996 SPE Annual Technical Conference and Exhibition, Denver 6-9 October.
7. Milliken, W.J. *et al.*: "Application of 3-D Streamline Simulation to Assist History Matching," paper SPE 63155 presented at the 2000 SPE Annual Technical Conference and Exhibition, Dallas, 1-4 October.
8. Wang, Y. and Kovscek, A.R.: "A Streamline Approach to History Matching Production Data," paper SPE 59370 presented at the 2000 SPE/DOE Symposium on Improved Oil Recovery, Tulsa, 3-5 April.
9. Wu, Z. and Datta-Gupta, A.: "Rapid History Matching Using a Generalized Travel Time Inversion Method," *SPE Journal*, 7(2), 113-122, June (2002)..
10. Reynolds, A. C., He, N., and Oliver, D.S.: "Reducing Uncertainty in Geostatistical Description with Well Testing Pressure Data," in *Proc*., 1997 International Reservoir Characterization Conference, Houston, 2-4 March.
11. Landa, J.L. and Horne, R.N.: "A Procedure to Integrate Well Test Data, Reservoir Performance History and 4-D Seismic Information into a Reservoir Description," paper SPE 38653 presented at the 1997 SPE Annual Technical Conference and Exhibition, San Antonio, TX, Oct. 5-8.
12. He, Z., Datta-Gupta, A., and Yoon, S.: "Streamline-Based Production Data Integration with Gravity and Changing Field Conditions*," SPE Journal*, 7(4), 423-436, December (2002).
13. King, M.J. and Datta-Gupta, A.: "Streamline Simulation: A Current Perspective," *In Situ* (1998) **22**, No. 1, 91.
14. Wen, X. *et al.*: "High Resolution Reservoir Models Integrating Multiple-Well Production Data," paper SPE 38728 presented at the 1997 SPE Annual Technical Conference and Exhibition, San Antonio, Texas, 5-8 October.
15. Luo, Y. and Schuster, G.T.: "Wave-Equation Traveltime Inversion," *Geophysics* (1991) **56,** No. 5, 645.
16. Bates, D.M. and Watts, D.G.: "Relative Curvature Measures of Nonlinearity," *J. R. Statist. Soc. B* (1980) **42**, No. 1, 1.

17. Grimstad, A.-A. and Mannseth, T.: "Nonlinearity, Scale, and Sensitivity for Parameter Estimation Problems," *SIAM J. Sci. Comput.* (2000) **21**, No. 6, 2096.
18. Mannseth, T. *et al.*: "Functional Representation and Model Nonlinearity in Estimation of Porous Media Properties From Laboratory Experiments," presented at the Fourth SIAM Conference on Mathematical and Computational Issues in the Geosciences, Albuquerque, NM, 16-19 June, 1997.
19. Yeh, W. W-G: "Review of Parameter Identification Procedures in Groundwater Hydrology: The Inverse Problem," *Water Resources Research* (1986) **22**, No. 2, 95.
20. Bissel, R.C. *et al.*: "Reservoir History Matching Using the Method of Gradients," paper SPE 24265 presented at the 1992 SPE European Petroleum Computer Conference, Stavanger, 25-27 May.
21. Sun, N-Z and Yeh, W. W.-G.: "Coupled Inverse Problems in Groundwater Modeling, I, Sensitivity Analysis and Parameter Identification," *Water Resources Research* (1990) **26**, 2507.
22. Datta-Gupta, A. and King, M.J.: "A Semianalytic Approach to Tracer Flow Modeling in Heterogeneous Permeable Media," *Advances in Water Resources* (1995) **18**, No. 1, 9.
23. Parker, R.L.: *Geophysical Inverse Theor*y, Princeton University Press, 1994.
24. Paige, C.C. and Saunders, M. A.: "LSQR: An Algorithm for Sparse Linear Equations and Sparse Least Squares," *ACM Trans. Math. Software* (1982) **8**, No. 1, 43.
25. Nolet, G.: "Seismic Wave Propagation and Seismic Tomography," in *Seismic Tomograph*y, G. Nolet (Ed.), D. Reidel, Dordrecht, (1987) 1-23.
26. Lichtenberger, J.: "Field Application of Interwell Tracers for Reservoir Characterization of Enhanced Oil Recovery Pilot Areas," paper SPE 21652 presented at the 1991 SPE Production Operations Symposium, Oklahoma City, 7-9 April.
27. Allison, S.B., Pope, G.A., and Sepehrnoori, K., "Analysis of Field Tracers for Reservoir Description," *J. Pet. Sci. Eng.* (1991), **5,** 173-186.
28. Iliassov, P.A. *et al.*: "Field-Scale Characterization of Permeability and Saturation Distribution Using Partitioning Tracer Tests: The Ranger Field, Texas," *SPE Journal*, 7(4), 409-423, December (2002).
29. Deutsch, C.V. and Journel, A.G.: *GSLIB: Geostatistical Software Library and User's Guide*, Oxford University, 1998.

Part-II

1. Haldorsen, H. H.: "Simulator Parameter Assignment And the Problem of Scale in reservoir engineering," Reservoir Characterization, Lake, L.W. and Carroll, H.B. Jr. (eds.), Academic Press, Inc. Orlando, FL, 1986.
2. Doyen, P.M., Psaila, D.E., den Boer, L.D. and Jans, D.: "Reconciling Data at Seismic and Well Log Scales in 3-D Earth Modeling," SPE 38698 paper presented at the 1997 SPE Annual Technical Conference and Exhibition, San Antonio, TX, October 5-8.
3. Beherns, R.A., Macleod, M.K., Tran, T.T., and Alimi, A.O.: "Incorporating Seismic Attribute Maps in 3D Reservoir Models," *SPE Reservoir Evaluation & Engineering* (1998), **1**(2), 122-126.
4. Doyen, P. M.: "Porosity from Seismic Data: A Geostatistical Approach," *Reservoir Characterization 2*, SPE reprint series No. 27, Society of Petroleum Engineers, Richardson, TX, 1989.

5. Almeida, A.: “Joint Simulation of Multiple Variable with a Markov-type Coregionalization Model,” Ph.D Dissertation, Stanford University, Stanford, CA (1993).
6. Xu, W., Tran, T.T., Srivastava, R.M., Journel, A.G.: “Integrating Seismic Data in Reservoir Modeling: The Collocated Cokriging Alternative,” SPE 24742 paper presented at the 1992 SPE Annual Technical Conference and Exhibition, Washington, DC, October 4-7.
7. Deutsch, C.V., Srinivasan, S. and Mo, Y.: “Geostatistical Reservoir Modeling Accounting for Precision and Scale of Seismic Data,” SPE 36497 paper presented at the 1996 SPE Annual Technical Conference and Exhibition, Denver, Colorado, October 6-9.
8. Xue, G. and Datta-Gupta, A.: “A New Approach to Seismic Data Integration During Reservoir Characterization Using Optimal Nonparametric Transformations,” SPE 36500 paper presented at the 1996 SPE Annual Technical Conference and Exhibition, Denver, Colorado, October 6-9.
9. Frykman, P. and Deutsch, C.V.: “Geostatistical Scaling Laws Applied to Core and Log Data,” SPE 56822 paper presented at the 1999 SPE Annual Technical Conference and Exhibition, Houston, TX, October 3-6.
10. Behrens, R.A. and Tran, T.T.: “Incorporating Seismic Data of Intermediate Vertical Resolution into 3D Reservoir Models,” SPE 49143 paper presented at the 1998 SPE Annual Technical Conference and Exhibition, New Orleans, LS, September 27-30.
11. Doyen, P.M., Psaila, D.E., den Boer, L.D., and Jans, D.: " Reconciling Data at Seismic and Well Log Scales in 3-D Earth Modeling," paper SPE 38498, presented at the 1996 SPE Annual Technical Conference and Exhibition, Denver, CO, October 6-9.
12. Dubrule, O.: “Estimating or Choosing a Geostatistical Model,” Geostatistics For the Next Century, Roussos Dimitrakopoulos (eds.), Kluwer Academic Publishers, Dordrecht, The Netherlands, 1994.
13. Graffigne, C. et al.: “Hierarchical Markov Random Field Models Applied to Image Analysis: A Review,” Neural, Morphological, and Stochastic Methods in Image and Signal Processing, Dougherty E.R, Francoise, P. and Shen, S.S. (eds.), San Diego, California, SPIE 2568, 1995.
14. Perez, P. and Heitz, F.: “Restriction of a Markov Random Field on a Graph and Multiresolution Image Analysis,” Technical Report 2170, INRIA, IRISA, Mar.1994.
15. Tjelmeland, H., Besag, J.: “Markov Random Fields with Higher-order Interactions,” Scandinavian Journal of Statistics (1998), 25(3), 415-433.
16. Hoiberg, J., Omre, H., and Tjelmeland, H.: “Large-Scale Barriers in Extensive Drilled Reservoirs,” in Proc. 2nd European Conference on the Mathematics of Oil Recovery, D. Guerillot and O. Guillon (eds.), Editions Technip, Paris (1990).
17. Tjelmeland, H. and Holden, L.: “Semi-Markov Random Fields,” Geostatistics Troia ’92, Soares, A. (ed.), Kluwer Academic Publishers, Dordrecht, The Netherlands, 1993.
18. Lee, S.H., Malallah, A., and Datta-Gupta, A.: “Multiscale Data Integration Using Markov Random Fields,” SPE 63066 paper presented at the 2000 SPE Annual Technical Conference and Exhibition, Dallas, Texas, October 1-4.
19. Lakshmanan, S. and Derin, H.: “Gaussian Markov Random Fields at Multiple Resolutions,” Markov Random Fields: Theory and Application, Chellappa, R. and Jain, A. (eds.), Academic Press Inc., London, 1993.
20. Kato, Z., Berthod, M., and Zerubia, J.: “Multiscale Markov Random Field Models for Parallel Image Classification,” Proc. Int. Conf. Computer Vision, Berlin, Germany, 1993.

21. Ripley, B. D.: "Stochastic Models for The Distribution of Rock Types in Petroleum Reservoirs," Statistics in the Environmental and Earth Sciences: New Developments in Theory & Practice, Walden, A.T. and Guttorp, P. (eds.), Edward Arnold, London, 1992.
22. Tjelmeland, H.: "Modeling of The Spatial Facies Distribution by Markov Random Fields," Geostatistics Wollongong '96, Proceedings of the Fifth International Geostatistical Congress, Baafi, E.Y. and Schofield, N.A. (eds.), Kluwer Academic Publishers, Dordrecht, The Netherlands, 1997.
23. Besag, J.: "Spatial Interaction and The Statistical Analysis of Lattice Systems," Journal of the Royal Statistical Society B (1974), 36, 192-236.
24. Higdon, D.: Spatial Applications of Markov Chain Monte Carlo for Bayesian Inference, Ph. D. dissertation, University of Washington, Seattle, WA., 1994
25. Besag, J., Green, P. J., Hidgon, D. and Mengersen, K.: "Bayesian computation and stochastic systems (with Discussion)," Statistical Science(1995), 10, 3-66.
26. Gilks, W.R., Richardson, S. and Spegelhalter, D.J.: Markov Chain Monte Carlo in Practice, Chapman and Hall/CRC, London, 1996.
27. Li, S.Z.: Markov Random Field Modeling in Computer Vision, Springer-Verlag, New York, 1995.
28. Devine, O.J., and Louis, T.A., and Halloran, M.E.: "Empirical Bayes Estimators for Spatially Correlated Incidence Rates," Environmetrics (1994), 5, 381-398.
29. Rue, H. and Tjelmeland, H.: Fitting Gaussian Markov Random Fields to Gaussian Fields," Statistics No.16, Department of Mathematical Sciences, Norwegian University of Science and Technology, Trondheim, Norway, 1999.
30. Caers, J.: "Automatic Histogram and Variogram Reproduction in Simulated Annealing Simulation," Mathematical Geology (2001), 33, 2, 167-190.
31. Journel, A.G.: "Conditional Geostatistical Operations to Nonlinear Volume Averages," Mathematical Geology (1999), 31(8), 931-953.
32. Geyer, C.J: Markov Chain Mote Carlo Lecture Notes, 1998 (S.H. Lee, Private collection).
33. Brémand, P.: Markov Chains: Gibbs Fields, Monte Carlo Simulation, And Queues, Springer-Verlag, New York, 1991.
34. Journel, A. and Alabert, F. G., "A New Method for Reservoir Mapping," Journal of Petroleum technology, February, 1990.
35. Polkowski, G. R., 1997, Degradation of Reservoir Quality by Clay Content, Unayzah Formation, Central Saudi Arabia, GeoArabia, v. 2, no.1, p 49-61.
36. Senalp, M., and Al-Duaiji, A., 1995, Stratigraphy and Sedimentation of Unayzah Reservoir, Central Saudi Arabia, Middle East Petroleum Geosciences, Geo 94, v.2, p. 837-847.
37. Ferdinand, K.: "The Integration of Seismic Attributes and Rock Properties for Mapping Porosity Thickness in the Heterogeneous Grayburg Carbonate Reservoir, Corrigan Cowden Unit West Texas," BP, Houston, TX.

Part-IIIA

1. Jennings, J. W. Jr., S.C. Ruppel, W. B. Ward: "Geostatistical Analysis of Permeability Data and Modeling of Fluid-Flow Effects in Carbonate Outcrops", SPE Reservoir Evaluation and Engineering Vol. 3, No. 4, August 2000
2. Kragas, Tor K., Brock A. Williams, Gregory A. Myers: "The Optic Oil Field: Deployment and Application of Permanent In- well Fiber Optic Sensing Systems for

Production and Reservoir Monitoring", paper SPE 71529 presented at the 2001 SPE Annual Technical Conference and Exhibition, New Orleans, Louisiana, 30 September-3 October
3. Wu, Zhan, Akhil Datta Gupta: "Rapid History Matching Using a Generalized Travel-Time Inversion Method", SPE Journal, Vol. 7, No. 2, June 2002
4. Yoon, S., I. Barman, A. Datta-Gupta, and G.A. Pope: "In-Situ Characterization of Residual NAPL Distribution Using Streamline-Based Inversion of Partitioning Tracer Tests," SPE 52729 Proceedings of the 1999 SPE/EPA Exploration & Production Environmental Conference, Austin, TX, 28 February - 3 March.
5. Zemel, B.: " Tracers in the Oil Field", Developments in Petroleum Science, Vol. 43, Elsevier Science, 1995

Part-IIIB

1. Benett, B. and S. R. Larter: "Partition behavior of alkyl phenols in crude oil/brine systems under subsurface conditions", Geochimica et Cosmochimica Acta, Vol. 61, No. 20, 1997
2. Kharaka, Yousif K., Paul D. Lundegard and Thomas H. Giordano: " Distribution and origin of organic ligands in subsurface waters from sedimentary basins", Ore Genesis and Exploration: The Roles of Organic Matter, Reviews in Economic Geology, Vol. 9, 2000
3. Larter, S.R., and A. C. Aplin: "Reservoir geochemistry: Methods, applications and opportunities", The geochemistry of reservoirs, Geological Society Special Publication, No. 86, 1995
4. Reinsel, Mark A., John J. Borkowski and John T. Sears: " Partition coefficients for Acetic, Propionic and Butyric Acids in a crude oil/water system", Journal of Chemical Engineering Data, 39, 1994
5. Taylor, P., Steve Larter, Martin Jones, Jason Dale and Idar Horstad: " The effect of oil-water-rock partitioning on the occurrence of alkyl phenols in petroleum systems", Geochimica et Cosmochimica Acta, Vol. 61, No. 9, 1997

LIST OF ACRONYMS AND ABBREVIATIONS

$\boldsymbol{d}$ = data vector
C_c = calculated tracer concentration
C_o = observed tracer concentration
D = dispersion coefficient
$\boldsymbol{F}_k$ = tangent vector
$\boldsymbol{F}_{kk}$ = acceleration vector
I = identity matrix
k = permeability
L = spatial difference operator
n_b = number of grid blocks
n_o = number of dynamic data observations
s = slowness
S = sensitivity matrix
t = time
u = Darcy velocity
v = Interstitial velocity
β = weighting factor
κ_{am} = measure of nonlinearity for amplitude inversion
κ_{gt} = measure of nonlinearity for generalized travel-time inversion
κ_{tt} = measure of nonlinearity for travel-time inversion
τ = time of flight
$\Delta\tau$ = generalized travel-time or travel-time shift